ORBITAL RENDEZVOUS AND SPACECRAFT LOITERING

IN THE EARTH-MOON SYSTEM

A Thesis

Submitted to the Faculty

of

Purdue University

by

Fouad Khoury

In Partial Fulfillment of the

Requirements for the Degree

of

Master of Science in Aeronautics and Astronautics

December 2020

Purdue University

West Lafayette, Indiana

THE PURDUE UNIVERSITY GRADUATE SCHOOL
STATEMENT OF THESIS APPROVAL

Dr. Kathleen Howell, Chair

    School of Aeronautics and Astronautics

Dr. Carolin Frueh

    School of Aeronautics and Astronautics

Dr. David Spencer

    School of Aeronautics and Astronautics

Approved by:

    Dr. Gregory Blaisdell

        Associate Head of the Graduate School of Aeronautics & Astronautics

To my parents, Saeb & Lama, and my siblings, Omar & Karmah

أحط نفسك بالأشخاص الذين يرون مواضع العظمة فيك .

ACKNOWLEDGMENTS

"The known is finite, the unknown infinite; intellectually we stand on an islet in the midst of an illimitable ocean of inexplicability. Our business in every generation is to reclaim a little more land." - T. H. Huxley

This work would not be possible without the support of many of my colleagues and mentors. I am grateful for the experiences and interactions I have had (and hopefully continue to have) with each of them. First, I would like to express my gratitude to my adviser Professor Kathleen Howell for her guidance, patience, and encouragement. It has been my honor to serve as her student, teaching assistant, and researcher. I furthermore express my gratitude to my fellow researchers in the Multibody Dynamics Research Group, both past and present. Thank you to Andrew C, Robert, Collin, Brian, Emily, RJ, David, Beom, Ricardo, Rohith, Vivek, Juan, Maaninee, Andrew M, Stephen, Kenza, Bonnie, Nick, Paige, Yuki, and Kenji for your technical advice and feedback. Your friendships have enabled me to not just finish my journey in graduate school but to enjoy and learn from it as well. Moreover, I would like to thank the professors in my committee, Professors Carolin Frueh and David Spencer, for reviewing my work and providing valuable insights.

I would also like to thank my mentors Dr. Alan Lovell, from the Air Force Research Lab (AFRL), Dr. Diane Davis, from a.i. solutions, and the many engineers at the NASA Johnson Space Center. Their collaboration and feedback have been instrumental in establishing the foundations for this work. Moreover, I would like to express my appreciation to the engineers at John Hopkins University Applied Physics Laboratory for their discussions and insight. I look forward to joining their ranks and contributing to the advancement of space technologies and missions.

Finally, I thank my family both in the United States and abroad. Your sacrifices

and support have enabled me to pursue my passions and develop a love for learning. To my father, I thank you for instilling in me perseverance and a strong work ethic. To my mother, thank you for teaching me the value of sacrifice and patience. To my brother, thank you for teaching me to recognize beauty in the natural world and humankind's placement in it. Finally, to my sister, thank you for teaching me the importance of displaying kindness and respect to everyone.

TABLE OF CONTENTS

LIST OF TABLES

LIST OF FIGURES

Figure   Page

Figure   Page

ABSTRACT

Khoury, Fouad M.S., Purdue University, December 2020. Orbital Rendezvous and Spacecraft Loitering in the Earth-Moon System. Major Professor: Kathleen C. Howell.

To meet the challenges posed by future space exploration activities, relative satellite motion techniques and capabilities require development to incorporate dynamically complex regimes. Specific relative motion applications including orbital rendezvous and spacecraft loitering will play a significant role in NASA's Gateway and Artemis missions which aim to land the first woman and next man on the Moon by 2024. In this investigation, relative motion in the restricted 3-body problem is formulated, validated, and tested in a rotating local-vertical-local-horizontal (LVLH) frame situated at a target spacecraft and followed by a chaser. Two formulations of the restricted 3-body problem are considered, namely the Circular Restricted 3-Body Problem (CR3BP) and the Elliptical Restricted 3-Body Problem (ER3BP). Comparisons between the relative dynamical models in the CR3BP and ER3BP, respectively, and other standard relative motion sets of equations such as the Euler-Hill (HCW) model and the Linear Equations of Relative Motion (LERM) are accomplished to identify limitations and inaccuracies pertaining to the in orbits that exist in the CR3BP and ER3BP, respectively. Additionally, the relative motion equations are linearized to develop computational tools for solutions to the rendezvous and space loitering problems in the Earth-Moon system.

1. INTRODUCTION

Relative satellite motion between manned orbiting spacecraft was initially implemented for use in the Gemini and Apollo missions. In 1965, the first successful crewed rendezvous between two spacecraft was performed with Gemini-6A (crewed by Walter Schirra & Thomas Stafford) and Gemini 7 (crewed by Frank Borman & James Lovell) in Earth orbit. Since then, relative satellite motion has played an essential part in space missions with applications ranging from rendezvous & docking, formation flying, and proximity operations. Moreover, proposed future applications include satellite servicing, on-orbit assembly, and space debris removal. One of the most successful applications of relative motion includes the cargo and crew resupply missions with the International Space Station (ISS) in low Earth orbit. For almost two decades, the ISS has served as an multinational platform for micro-gravity and space environment research for established and emerging civilian space agencies.

The fundamental step in any relative motion analysis includes the formulation and validation of the system's equations of motion. Traditionally, a Keplerian model frequently serves as the basis to characterize the dynamics of two spacecraft in orbit around a main primary. From this initial assumption, a number of relative motion models have been formulated, validated, and successfully implemented for real-world missions. Historically, relative motion models have been formulated in a rotating local-vertical-local-horizontal (LVLH) frame attached to a spacecraft along its orbit. As a result, these models characterize the motion of another spacecraft termed as the chaser or deputy with respect to the origin of the LVLH frame located at the target or chief. Employing this local frame is particularly important for rendezvous, docking, and formation flying missions since orbital motion is expressed from the perspective of the target or chief. Moreover, the LVLH frame is used to assess trajectories and ensure collision avoidance as well as facilitate proximity operations. Among the dy-

namical models that are the most widely applied are the Euler Hill [2] equations (also denoted as the Hill-Clohessy-Wiltshire (HCW) equations) introduced in 1960 for the design of a terminal rendezvous guidance strategy for circular orbits. These equations assume a target orbit to be circular and a chaser spacecraft in close proximity along a slightly elliptic and possibly, slightly inclined orbit. If the nonlinear equations of relative motion in the Keplerian model are formulated and subsequently linearized by means of a Taylor expansion about the target position, the model is denoted the Linear Equations of Relative Motion (LERM). These equations provide a good characterization of the relative motion between the target and chaser vehicles assuming the initial distance between the spacecraft is sufficiently small with respect to the target orbit radius. According to Alfriend et al. [11], previous analysis suggests that the LERM are best employed when the relative distance is smaller than 50 km. More recently developed models include the Yamanaka-Ankersen STM [3] approximations for arbitrary elliptical orbits. Although these models demonstrate continued success in space missions appropriate to their respective regimes, they generate unacceptable errors in their descriptions of relative orbits that exist with the incorporation of both Earth and Moon gravity fields as point masses. Incorporation of both the Earth and Moon gravity is necessary in formulations for relative motion analysis for orbits in models with increased dynamical complexity and applications in cislunar space.

1.1 Problem Definition

NASA's proposed Gateway and Artemis missions, as envisioned by the 2017 Space Policy Directive [28], aim to land the first woman and next man on the Moon by 2024. As part of the 2017 directive on space exploration, the agency seeks to establish a long term presence in lunar orbit and on the Moon's surface to develop new capabilities for future missions to Mars and beyond. Although the Apollo program (1969 - 1972) was largely successful in accomplishing its technical objectives, the missions were characterized by short duration trips to the Moon (about 3 days) and remained in

lunar orbit. In constrast, proposed mission architectures require longer durations in the lunar vicinity and employ non-Keplerian orbits with favorable stability and eclipse avoidance properties. Two proposed orbits for the Gateway and Artemis programs include the 9:2 L_2 lunar synodic resonant Near Rectilinear Halo Orbit (NRHO) and a Distant Retrograde Orbit (DRO) with an altitude of approximately 70,400 km from the lunar surface. These orbits only exist in the CR3BP which incorporate both the Earth and Moon gravity as point masses, in contrast to the Keplerian 2-body model. Consequently, dynamical models that develop based on the CR3BP assumptions must be derived and formulated to accurately represent the physics of relative motion between a target and chaser spacecraft along these specified trajectories. To reciprocate techniques employed for rendezvous operations in 2-body regimes, equations of relative motion are formulated and derived in an LVLH frame attached to a target spacecraft; however, definitions for the LVLH coordinates are modified. Once established, these equations are validated against traditional relative motion models to identify the limitations of the 2-body assumptions along the 9:2 L_2 NRHO and DRO. Furthermore, these models are linearized about the target's position and employed to construct a maneuver scheme to address rendezvous and space loitering problems in the Earth-Moon system. Finally, single and multiple shooting approaches formulated specifically to the LVLH frame are introduced to compute maneuvers and achieve terminal rendezvous or produce bounded motion in the relative space.

1.2 Previous Contributions

Although relative motion problem in the 2-body problem has been studied extensively, investigations of 3-body relative motion dynamics are more limitd. Nevertheless, there is some effort to develop strategies for rendezvous operations within the context of the CR3BP. Colagrossi et al. [10] examine rendezvous and docking operations for a very large space structure in a halo orbit about L_2. The model employed

incorporates coupled orbit and attitude motion in the CR3BP and uses a lumped parameter approach to accommodate the flexible dynamics. Murakami et al. [6] propose a practical rendezvous scenario for logistics missions to a cislunar space station in the vicinity of the Earth-Moon L_2 point. Both analyses formulate the dynamics in a synodic frame based at the system barycenter. Franzini et al. [1] first formulated and derived the nonlinear equations of motion in a LVLH frame based on assumptions in the restricted 3-body problem. The equations and their linear counterparts are validated against the HCW and LERM models along a NRHO. The analysis suggests that the linearized equations are accurate near apolune but perform poorly in the vicinity of perilune where rapid separation between the target and chaser exceeds the range of validity for the linearization assumption. A maneuver scheme incorporating single and multiple thruster firings is proposed and a number of rendezvous scenarios are examined along an NRHO. Both impulsive and continuous thrust profiles are considered for initial relative separations of up to a few kilometers between the target and chaser vehicles. This investigation aims to reproduce the formulation and validation of the nonlinear equations of relative motion proposed by Franzini et al. and extend the analyses to incorporate other target orbits of interest in the cislunar vicinity.

1.3 Document Outline

The basis for this work is the formulation of the set of equations of relative motion in the restricted 3-body problem. Specifically, two formulations of the restricted 3-body problem are investigated namely, the CR3BP and ER3BP. A derivation and analysis of both models produces the desired reference orbit geometry for the target spacecraft. Given these differential equations, the nonlinear relative equations of motion are formulated and validated using the approach consistent with Franzini et al [1]. The equations and their linear counterparts are also examined against the HCW and LERM in a 9:2 L_2 NRHO, large radius DRO, and small radius DRO. Initial relative states between the target and chaser spacecraft are selected along

the corresponding orbits for the validation procedure. Finally, single and multiple shootings scheme are proposed to facilitate the computation in rendezvous and space loitering problems for all three target orbits.

- Chapter 2: A brief overview of Keplerian motion is provided for reference. The equations of motion for the restricted 3-body problem are derived along with the appropiate assumptions to the model to include the ER3BP and CR3BP. The equations are developed in two synodic reference frames: S , based at the system barycenter; and M, originating at the center of the second primary. In the ER3BP, a pseudo-potential function and equilibrium points are identified to offer insight into the problem. Likewise, the CR3BP investigation includes an overview of the pseudo-potential function, a single integral of the motion, and the equilibrium points. Zero velocity surfaces and symmetry properties supply intuition governing the dynamical flow. Variational equations for both the ER3BP and CR3BP are summarized to highlight computation tools for relative solutions in both regimes. Finally, dynamical systems theory is employed to introduce differential corrections techniques and a number of periodic orbit families are computed. A multiple patch point framework is proposed to transition solutions from the CR3BP to the ER3BP and higher-fidelity ephemeris models.

- Chapter 3: First, let L denote the LVLH frame L; an overview and appropriate definition are introduced. Two relative motion models in 2-body problem, expressed in frame L, are derived for reference. The nonlinear equations of relative motion in the ER3BP and CR3BP are then formulated and derived using the process proposed by Franzini et al. Next, these relative motion models are verified and validated along three target orbits: a 9:2 L_2 NRHO, a high radius DRO (about 70,400 km altitude), and a small radius DRO (about 9000 km altitude). Finally, single and multiple shooting schemes are proposed to target relative states and geometry in the LVLH frame.

- Chapter 4: Two types of relative motion applications are examined, namely orbital rendezvous and spacecraft loitering. A number of rendezvous scenarios are investigated along all three target orbits with varying relative states. An approach to address the spacecraft loitering problem for each of these orbits is proposed along with examples that demonstrate bounded behavior in the LVLH frame.

- Chapter 5: A summary of results is provided and recommendations for future analysis and work are suggested.

2. BACKGROUND

The motion of a body under the influence of a single primary has been studied extensively for centuries. Although an analytical closed-form solution exists for this dynamical model, these two-body approximations can exhibit inaccuracies when another primary is incorporated. However, multi-body systems ($n \geq 3$) do not possess analytical solutions for the motion and instead require numerical integration of the governing equations of motion. First, to explore this problem, the restricted 3-body problem is formulated for arbitrary masses in a synodic frame S centered at the system barycenter. Simplifying assumptions are then employed to produce the ER3BP and CR3BP equations of motion.

2.1 Keplerian Dynamics

The two-body problem has served as the basis for trajectory design in support of many early spacecraft missions in the twentieth century. A number of simplifying assumptions employed in the model include the representation of both bodies as centrobaric point-masses and the inverse square law as the description of the gravitational force between them. The general problem of two bodies is depicted in Figure 2.1.
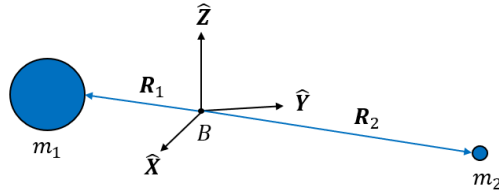
Fig. 2.1. Diagram of the two-body model.

An inertially fixed coordinate system is centered at the system barycenter B. An inertial coordinate system I is defined as a dextral orthogonal triad represented by directions $\hat{\mathbf{X}}, \hat{\mathbf{Y}}$, and $\hat{\mathbf{Z}}$. The quantities $\mathbf{R}_1$ and $\mathbf{R}_2$ denote the position vectors of the first and second primary bodies as measured from B, respectively, and are assummed to be point masses. If the inverse square law is employed to model the mutual gravitational force between the two bodies, the motions of m_1 and m_2 are governed by the following second-order vector differential equations

$$\ddot{\mathbf{R}}_1 = \frac{Gm_2}{r_{12}^3}\mathbf{r}_{12} \tag{2.1}$$

$$\ddot{\mathbf{R}}_2 = -\frac{Gm_1}{r_{12}^3}\mathbf{r}_{12} \tag{2.2}$$

$$\ddot{\mathbf{r}}_{12} = \ddot{\mathbf{R}}_2 - \ddot{\mathbf{R}}_1 = -\frac{G(m_1 + m_2)}{r_{12}^3}\mathbf{r}_{12} = -\frac{\mu}{r^3}\mathbf{r} \tag{2.3}$$

where μ is the gravitational constant, $\mathbf{r}_{12}$ is the relative position vector from m_1 to m_2, and r_{12} is the norm of $\mathbf{r}_{12}$. For notation purposes, the subscript is dropped from $\mathbf{r}_{12}$ and for other expressions involving the two-body model. There are several methods to produce the closed-form solution to Equations (2.1) - (2.3), but for simplicity this investigation employs the process in Alfriend et al. [11]. To obtain the analytical solution to Equation (2.3), it is useful to transform the inertially-based equations into a rotating synodic frame S with axes $\hat{\mathbf{x}}_s, \hat{\mathbf{y}}_s$ and $\hat{\mathbf{z}}_s$ analogous to polar coordinates. In this frame, $\hat{\mathbf{x}}_s = \mathbf{r}_{12}/\|\mathbf{r}_{12}\|$, $\hat{\mathbf{z}}_s$ coincides with the direction of the system angular momentum vector (normal to the orbital plane), and $\hat{\mathbf{y}}_s$ completes the right-handed set. Figure 2.2 depicts the two-body model in frame S. To that end, the following kinematical expressions are first introduced

$$\mathbf{r} = r\hat{\mathbf{x}}_{\mathbf{s}} \tag{2.4}$$

$$\dot{\mathbf{r}} = \dot{r}\hat{\mathbf{x}}_s + r\dot{\theta}\hat{\mathbf{y}}_s \tag{2.5}$$

$$\ddot{\mathbf{r}} = (\ddot{r} - r\dot{\theta}^2)\hat{\mathbf{x}}_s + (2\dot{r}\dot{\theta} + r\ddot{\theta})\hat{\mathbf{y}}_s \tag{2.6}$$
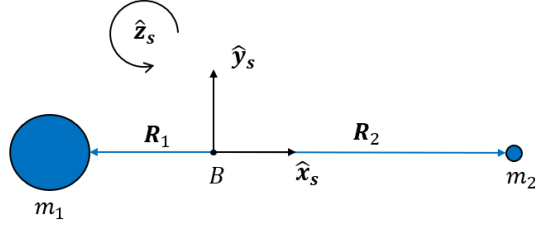
Fig. 2.2. Diagram of the two-body model in synodic frame S.

where θ is the argument of latitude and $\dot{\theta} = \omega_{S/I}$ is the angular velocity of frame S with respect to the inertial frame I. The dot above the quantity $\dot{\theta}$ is taken as the derivative with respect to time as observed from the inertial frame. Substituting Equation (2.6) into Equation (2.3) yields the following scalar expressions represented in frame S:

$$\ddot{r} = r\dot{\theta}^2 - \frac{\mu}{r^2} \tag{2.7}$$

$$\ddot{\theta} = -\frac{2\dot{r}\dot{\theta}}{r} \tag{2.8}$$

The orbit angular momentum vector per unit mass, $\mathbf{h}$, is defined as:

$$\mathbf{h} = \mathbf{r} \times \dot{\mathbf{r}} = \mathbf{r} \times \mathbf{v} = \begin{bmatrix} r \\ 0 \\ 0 \end{bmatrix} \times \begin{bmatrix} \dot{r} \\ r\dot{\theta} \\ 0 \end{bmatrix} = r^2\dot{\theta}\hat{\mathbf{z}}_\mathbf{s} = h\hat{\mathbf{z}}_\mathbf{s} \tag{2.9}$$

where $\hat{\mathbf{z}}_\mathbf{s}$ is a unit vector normal to the orbital plane of the two bodies. It is observed from Equation (2.8) that the scalar derivative

$$\frac{d}{dt}(r^2\dot{\theta}) = r(r\ddot{\theta} + 2\dot{r}\dot{\theta}) = 0 \tag{2.10}$$

Therefore, it is concluded that the angular vector $\mathbf{h}$ is time invariant and implies conservation of angular momentum. Since $\mathbf{h}$ is a vector quantity, the derivative with respect to time is

$$\dot{\mathbf{h}} = \dot{\mathbf{r}} \times \dot{\mathbf{r}} + \mathbf{r} \times \ddot{\mathbf{r}} = -\frac{\mu}{r^3} \mathbf{r} \times \mathbf{r} = \mathbf{0} \tag{2.11}$$

Clearly, the magnitude h is constant as are each of its inertial components. Next, the chain rule is applied to Equation (2.7) to obtain

$$\ddot{r} = \frac{d}{dt}\left(\frac{dr}{dt}\right) = \frac{dr}{dt}\frac{d}{dr}\left(\frac{dr}{dt}\right) = \dot{r}\frac{d}{dr}(\dot{r}) = d\left(\frac{\dot{r}^2}{2}\right) \tag{2.12}$$

To prove Equation (2.12), a u substitution is employed to express

$$\dot{r}\frac{d}{dr}(\dot{r}) = udu = d\left(\frac{u^2}{2}\right) = d\left(\frac{\dot{r}^2}{2}\right) \qquad \text{Q.E.D} \tag{2.13}$$

If the expression for the scalar value $\ddot{r}$ from Equation (2.7) is substituted into Equation (2.13), then

$$d\left(\frac{\dot{r}^2}{2}\right) = \left(\frac{h^2}{r^3} - \frac{\mu}{r^2}\right) \tag{2.14}$$

Equation (2.14) is integrated to arrive at

$$\mathcal{E} = \frac{\dot{r}^2}{2} + \frac{h^2}{2r^2} - \frac{\mu}{r} = \left(\frac{\dot{r}^2 + r\dot{\theta}^2}{2}\right) - \frac{\mu}{r} = \frac{v^2}{2} - \frac{\mu}{r} \tag{2.15}$$

where the scalar $\mathcal{E}$ is a constant of integration, denoted as the specific energy, as it is the sum of the kinetic and potential energies. Equation (2.15) demonstrates conservation of energy for the two-body system. Finally, both constants of integration yield the following expressions:

$$\dot{r} = \sqrt{2\left(\mathcal{E} + \frac{\mu}{r}\right) - \frac{h^2}{r^2}} \tag{2.16}$$

$$\dot{\theta} = \frac{h}{r^2} \tag{2.17}$$

All of the above expressions include derivatives with respect to time, yet it is convenient to introduce the independent variable as a function of θ. Dividing Equation (2.16) by Equation (2.17), the equation yields

$$\frac{dr}{d\theta} = \frac{r^2\sqrt{2(\mathcal{E} + \mu/r) - h^2/r^2}}{h} \tag{2.18}$$

It is observed that Equation (2.18) is a seperable differential expression, solved through direct integration with initial condition θ_0 by

$$\theta = \int \frac{hdr}{r^2\sqrt{2(\mathcal{E} + \mu/r) - h^2/r^2}} + \theta_0 = \cos^{-1}\frac{1/r - \mu/h^2}{\sqrt{2\mathcal{E}/h + \mu^2/h^4}} + \theta_0 \tag{2.19}$$

and then r is solved in Equation (2.19) to obtain

$$r = \frac{h^2/\mu}{1 + \sqrt{1 + 2\mathcal{E}h^2/\mu^2}\cos(\theta - \omega)} = \frac{p}{1 + e\cos\theta^*} \tag{2.20}$$

where

$$\omega = \theta_0 \tag{2.21}$$

$$p = h^2/\mu \tag{2.22}$$

$$e = \sqrt{1 + 2\mathcal{E}h^2/\mu^2} \tag{2.23}$$

$$\theta^* = \theta - \omega \tag{2.24}$$

are the argument of periapsis, semilatus rectum, eccentricity, and true anomaly, respectively. Equation (2.19) admits solutions in the form of conic sections which include a circle, ellipse, parabola, and hyperbola. Using the following expressions,

$$a = \frac{p}{1 - e^2} \tag{2.25}$$

$$\mathcal{E} = -\frac{\mu}{2a} \tag{2.26}$$

classifications of each conic is parameterized based on eccentricity e, semimajor axis a, and specific energy $\mathcal{E}$ as presented in Table 2.1.

Table 2.1.
Conic classification in the two-body problem

Conic	a value	e value	$\mathcal{E}$ value
Circle	$a > 0$	$e = 0$	$\mathcal{E} < 0$
Ellipse	$a > 0$	$0 < e < 1$	$\mathcal{E} < 0$
Parabola	$a = \infty$	$e = 1$	$\mathcal{E} = 0$
Hyperbola	$a < 0$	$e > 1$	$\mathcal{E} > 0$

The sign of $\mathcal{E}$ classifies the conic as either a closed ($\mathcal{E} < 0$) or an open ($\mathcal{E} > 0$) orbit. The expressions are subsequently referenced in the investigation of ER3BP since the motion of the second primary with respect to the first must be tracked to obtain the correct relative distance and velocities between the two bodies.

2.2   Elliptical Restricted 3-Body Problem

The addition of another particle of interest is foundation of the formulation of the general 3-body problem. The model is comprised of two primaries, m_1 and m_2, and a body of interest m. Each body imparts its gravitational influence on the other masses in the system. Figure 2.3 depicts the general three-body problem with inertial frame I and synodic frame S.
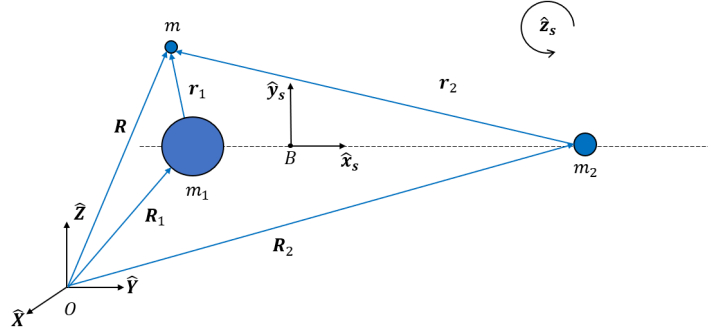
Fig. 2.3. Diagram of the three-body model in synodic frame S.

The general three-body problem operates on the assumption that all bodies can be modeled as point masses. This assumption infers that all masses are centrobaric, a reasonable approximation for planetary mass distributions. Consequently, the equations of motion are formulated as

$$\left[\ddot{\mathbf{R}}\right]_I = -\frac{Gm_1}{r_1^3}\mathbf{r}_1 - \frac{Gm_2}{r_2^3}\mathbf{r}_2 \tag{2.27}$$

$$\left[\ddot{\mathbf{R}}_1\right]_I = \frac{Gm_2}{r_{12}^3}\mathbf{r}_{12} + \frac{Gm}{r_1^3}\mathbf{r}_1 \tag{2.28}$$

$$\left[\ddot{\mathbf{R}}_2\right]_I = -\frac{Gm_1}{r_{12}^3}\mathbf{r}_{12} + \frac{Gm}{r_2^3}\mathbf{r}_2 \tag{2.29}$$

where

$$\mathbf{r}_1 = \mathbf{R} - \mathbf{R}_1 : \quad \text{relative position vector from } m_1 \text{ to } m \tag{2.30}$$

$$\mathbf{r}_2 = \mathbf{R} - \mathbf{R}_2 : \quad \text{relative position vector from } m_2 \text{ to } m \tag{2.31}$$

$$\mathbf{r}_{12} = \mathbf{R}_2 - \mathbf{R}_1 : \quad \text{relative position vector from } m_1 \text{ to } m_2 \tag{2.32}$$

and $\left[\ddot{\mathbf{R}}\right]_I$ specifies the acceleration of body m as observed from an inertial frame of reference I. Since accelerations are inertially based, they are subtracted to obtain the acceleration of the relative vectors as follows

$$\left[\ddot{\mathbf{r}}_1\right]_I = \left[\ddot{\mathbf{R}}\right]_I - \left[\ddot{\mathbf{R}}_1\right]_I = -\frac{G(m+m_1)}{r_1^3} - Gm_2\left(\frac{\mathbf{r}_2}{r_2^3} + \frac{\mathbf{r}_{12}}{r_{12}^3}\right) \tag{2.33}$$

$$\left[\ddot{\mathbf{r}}_2\right]_I = \left[\ddot{\mathbf{R}}\right]_I - \left[\ddot{\mathbf{R}}_2\right]_I = -\frac{G(m+m_2)}{r_2^3} - Gm_1\left(\frac{\mathbf{r}_1}{r_1^3} - \frac{\mathbf{r}_{12}}{r_{12}^3}\right) \tag{2.34}$$

As formulated above in Equations (2.33) and (2.34), no analytical solution exists to describe the motion of m subject to gravitational forces from m_1 and m_2. Nonetheless, Joseph Louis Lagrange (1736-1813) proposed a special circumstance where the mass of the third body is assumed negligible. The assumption that mass m is assumed to be much less than the other two primaries ($m << m_1, m_2$) is employed such the

original formulation of three bodies is coined the restricted 3-body problem. The mass of interest m then represents a spacecraft subject to the gravitational influence of two primaries m_1 and m_2. As a result, Equations (2.33) and (2.34) become

$$\left[\ddot{\mathbf{r}}_1\right]_I = -\mu_1 \frac{\mathbf{r}_1}{r_1^3} - \mu_2 \left(\frac{\mathbf{r}_2}{r_2^3} + \frac{\mathbf{r}_{12}}{r_{12}^3} \right) \tag{2.35}$$

$$\left[\ddot{\mathbf{r}}_2\right]_I = -\mu_2 \frac{\mathbf{r}_2}{r_2^3} - \mu_1 \left(\frac{\mathbf{r}_1}{r_1^3} - \frac{\mathbf{r}_{12}}{r_{12}^3} \right) \tag{2.36}$$

where $\mu_1 = Gm_1$ and $\mu_2 = Gm_2$ are the gravitational parameters of m_1 and m_2, respectively. Since the mass m is negligible, the two primaries move on conics about their common barycenter. In both the ER3BP and CR3BP, this motion is then the solution of the two-body problem. Since the motion of the primaries is Keplerian, their paths remain in a plane. Figure 2.4 depicts the geometry in the ER3BP as the orbits of the primaries m_1 and m_2 are elliptical about their common barycenter.
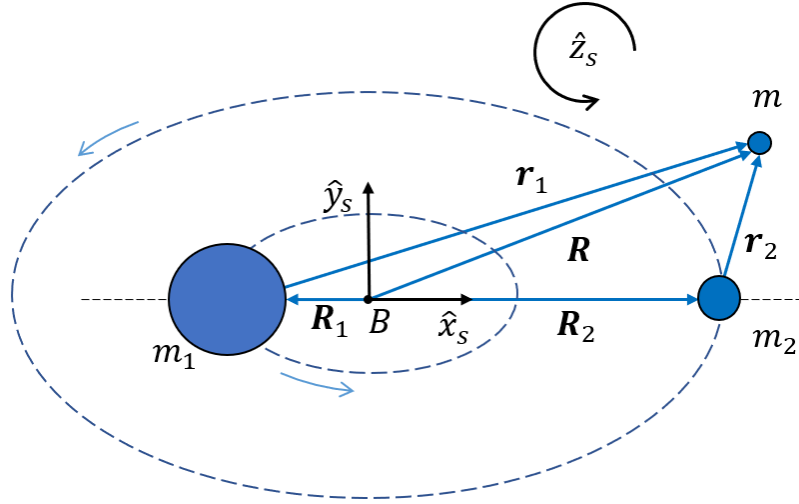
Fig. 2.4. Diagram of the three-body model in synodic frame S.

The synodic frame S is assumed to rotate with respect to the inertial frame I with angular velocity $\boldsymbol{\omega}_{S/I} = \omega_{S/I}\hat{\mathbf{z}}_s$. As a result, the basic kinematical equation is em-

ployed to compute the velocity and accelerations of vector $\mathbf{R}$ from an inertial observer as follows

$$\mathbf{R} = x\hat{\mathbf{x}}_s + y\hat{\mathbf{y}}_s + z\hat{\mathbf{z}}_s \tag{2.37}$$

$$\left[\dot{\mathbf{R}}\right]_I = \left[\dot{\mathbf{R}}\right]_S + \boldsymbol{\omega}_{S/I} \times \mathbf{R} \tag{2.38}$$

$$\left[\ddot{\mathbf{R}}\right]_I = \left[\ddot{\mathbf{R}}\right]_S + 2\boldsymbol{\omega}_{S/I} \times \left[\dot{\mathbf{R}}\right]_S + \left[\dot{\boldsymbol{\omega}}_{S/I}\right]_S \times \mathbf{R} + \boldsymbol{\omega}_{S/I} \times (\boldsymbol{\omega}_{S/I} \times \mathbf{R}) \tag{2.39}$$

Note that the position vector is expressed in terms of the synodic frame S. Without loss of generality, frames S and I coincide at B so that Equation (2.27) is substituted into Equation (2.39) to obtain

$$\left[\ddot{\mathbf{R}}\right]_S + 2\boldsymbol{\omega}_{S/I} \times \left[\dot{\mathbf{R}}\right]_S + \left[\dot{\boldsymbol{\omega}}_{S/I}\right]_S \times \mathbf{R} + \boldsymbol{\omega}_{S/I} \times (\boldsymbol{\omega}_{S/I} \times \mathbf{R}) = -\mu_1 \frac{\mathbf{r}_1}{r_1^3} - \mu_2 \frac{\mathbf{r}_2}{r_2^3} \tag{2.40}$$

where position vectors $\mathbf{r}_1$ and $\mathbf{r}_2$, measured from the barycenter B, denote the spacecraft position vectors with respect to m_1 and m_2, respectively, as

$$\mathbf{r}_1 = (x + R_1)\hat{\mathbf{x}}_s + y\hat{\mathbf{y}}_s + z\hat{\mathbf{z}}_s \tag{2.41}$$

$$\mathbf{r}_2 = (x - R_2)\hat{\mathbf{x}}_s + y\hat{\mathbf{y}}_s + z\hat{\mathbf{z}}_s \tag{2.42}$$

In component-wise form along each of the axis directions in frame S, the equations are expressed

$$\ddot{x} - 2\omega_{S/I}\dot{y} - \dot{\omega}_{S/I}y - \omega_{S/I}^2 x = -\mu_1 \frac{x + R_1}{r_1^3} - \mu_2 \frac{x - R_2}{r_2^3} \tag{2.43}$$

$$\ddot{y} + 2\omega_{S/I}\dot{x} + \dot{\omega}_{S/I}x - \omega_{S/I}^2 y = -\mu_1 \frac{y}{r_1^3} - \mu_2 \frac{y}{r_2^3} \tag{2.44}$$

$$\ddot{z} = -\mu_1 \frac{z}{r_1^3} - \mu_2 \frac{z}{r_2^3} \tag{2.45}$$

where the norm of the spacecraft distance from each of the primaries are expressed

$$r_1 = \sqrt{(x + R_1)^2 + y^2 + z^2} \qquad r_2 = \sqrt{(x - R_2)^2 + y^2 + z^2} \tag{2.46}$$

To compute the distances of the scalar quantities R_1 and R_2, the center of mass equation is employed at barycenter B. Using frame S, two equations are formulated to produce the following relationship,

$$-\mu_1 R_1 + \mu_2 R_2 = 0 \tag{2.47}$$

$$R_1 + R_2 = r_{12} \tag{2.48}$$

where r_{12} is the relative distance between m_1 and m_2. By solving for R_1 or R_2 in Equation (2.47) and substituting in Equation (2.48), the expressions yield

$$R_1 = \mu_s r_{12} \tag{2.49}$$

$$R_2 = (1 - \mu_s)r_{12} \tag{2.50}$$

where μ_s is classified as the *system* mass parameter given by

$$\mu_s = \frac{\mu_2}{\mu_1 + \mu_2} \tag{2.51}$$

It is apparent from the formulation of Equations (2.43)-(2.45) that the positions of the primaries R_1 and R_2 oscillate as the primaries m_1 and m_2 move along their respective

orbits around barycenter B. It is sometimes useful to change the origin of the synodic frame so that the spacecraft position is measured with respect to one of the primaries. Thus, a rotating synodic frame M with axes $\hat{\mathbf{x}}_m, \hat{\mathbf{y}}_m$ and $\hat{\mathbf{z}}_m$ is introduced so that the spacecraft position vector is referenced from the second primary, m_2. Frame M rotates with the same angular velocity as S, yet the axes are defined with different directions such that

$$\hat{\mathbf{x}}_m = -\frac{\mathbf{r}_{12}}{r_{12}} = -\hat{\mathbf{x}}_s \tag{2.52}$$

$$\hat{\mathbf{z}}_m = \frac{\mathbf{h}_{12}}{h_{12}} = \hat{\mathbf{z}}_s \tag{2.53}$$

$$\hat{\mathbf{y}}_m = \hat{\mathbf{z}}_m \times \hat{\mathbf{x}}_m = -\hat{\mathbf{y}}_s \tag{2.54}$$

$$\tag{2.55}$$

The formulation of synodic frame M is consistent with the definitions in Franzini et al [1]. The positive $\hat{\mathbf{x}}$ direction is directed towards the larger primary m_1 and $\hat{\mathbf{z}}$ is parallel to the normal of the orbital plane of the two primaries. Figure 2.5 depicts the differences of synodic frames S and M in the ER3BP. Both frames rotate with the same angular velocity with respect to the inertial frame I, however, they originate at different positions.
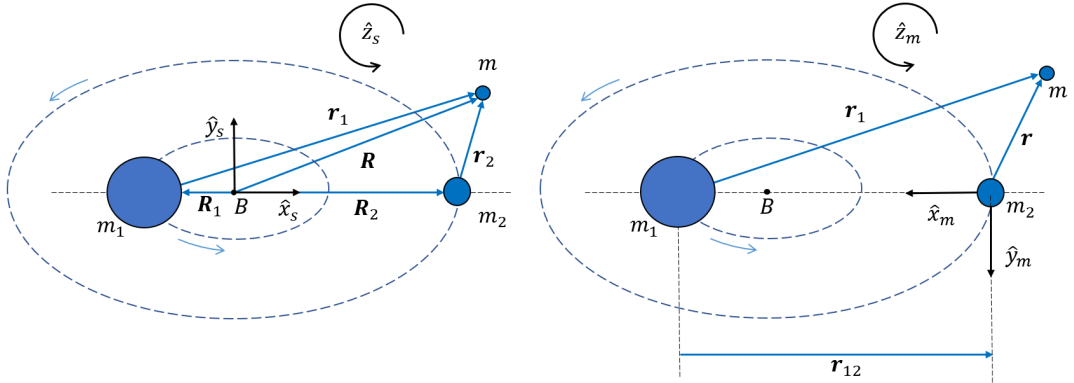
Fig. 2.5. Diagram of the ER3BP in synodic frames S (left) and M (right).

The employment of frame M provides a description of the motion of m with respect to the second primary m_2. For applications in spacecraft missions, it is more useful to reference a spacecraft's motion with respect to a primary instead of the system barycenter. Therefore, without loss of generality, if inertial frame I and synodic frame M coincide at m_2, the position, velocity, and acceleration of spacecraft m as expressed in frame M coordinates are

$$\mathbf{r} = x\hat{\mathbf{x}}_m + y\hat{\mathbf{y}}_m + z\hat{\mathbf{z}}_m \tag{2.56}$$

$$\left[\dot{\mathbf{r}}\right]_I = \left[\dot{\mathbf{r}}\right]_M + \boldsymbol{\omega}_{M/I} \times \mathbf{r} \tag{2.57}$$

$$\left[\ddot{\mathbf{r}}\right]_I = \left[\ddot{\mathbf{r}}\right]_M + 2\boldsymbol{\omega}_{M/I} \times \left[\dot{\mathbf{r}}\right]_M + \left[\dot{\boldsymbol{\omega}}_{M/I}\right]_M \times \mathbf{r} + \boldsymbol{\omega}_{M/I} \times (\boldsymbol{\omega}_{M/I} \times \mathbf{r}) \tag{2.58}$$

where $\mathbf{r}_{12} = -r_{12}\hat{\mathbf{x}}_m$, and the spacecraft position vectors from first and second primaries are defined as:

$$\mathbf{r}_1 = (x - r_{12})\hat{\mathbf{x}}_m + y\hat{\mathbf{y}}_m + z\hat{\mathbf{z}}_m \qquad \mathbf{r} = x\hat{\mathbf{x}}_m + y\hat{\mathbf{y}}_m + z\hat{\mathbf{z}}_m \tag{2.59}$$

In component-wise form, Equation (2.58) is written as

$$\ddot{x} - 2\omega_{M/I}\dot{y} - \dot{\omega}_{M/I}y - \omega_{M/I}^2 x = -\mu_1\left(\frac{x - r_{12}}{r_1^3} + \frac{1}{r_{12}^3}\right) - \mu_2\frac{x}{r^3} \tag{2.60}$$

$$\ddot{y} + 2\omega_{M/I}\dot{x} + \dot{\omega}_{M/I}x - \omega_{M/I}^2 y = -\mu_1\frac{y}{r_1^3} - \mu_2\frac{y}{r^3} \tag{2.61}$$

$$\ddot{z} = -\mu_1\frac{z}{r_1^3} - \mu_2\frac{z}{r^3} \tag{2.62}$$

where the norm of the distances between the spacecraft and primary m_1 and m_2 are evaluated as

$$r_1 = \sqrt{(x - r_{12})^2 + y^2 + z^2} \qquad r = \sqrt{x^2 + y^2 + z^2} \tag{2.63}$$

In the study of dynamical systems, it is often convenient to nondimensionalize quantities so that the equations of motion become functions of one parameter. Nondimensionalization for the ER3BP equations is accomplished by normalizing the following:

- dimensional distances l by the primary m_2 orbit semimajor axis a

- time t by the system mean motion n, i.e.,

$$n = \sqrt{\frac{G(m_1 + m_2)}{a^3}} \tag{2.64}$$

  and the introduction of a nondimensional time quantity τ such that $\tau = n(t - t_0)$

- mass quantities such that $\mu_1 + \mu_2 = 1$

As a consequence, any generic distance and its corresponding time derivatives are nondimensionalized as follows

$$l = a\tilde{l} \tag{2.65}$$

$$\dot{l} = a\frac{d\tilde{l}}{d\tau}\frac{d\tau}{dt} = an\tilde{l}' \tag{2.66}$$

$$\ddot{l} = an\frac{d\tilde{l}'}{d\tau}\frac{d\tau}{dt} = an^2\tilde{l}'' \tag{2.67}$$

where the quantities under the tilde symbol, i.e. $\tilde{l}$, denote nondimensionalized quantities and the superscript prime symbol, i.e. $\tilde{l}'$, represents derivatives with respect to τ. Angular quantities ω are nondimensionalized using a similar procedure, so it follows that

$$\omega = n\tilde{\omega} \tag{2.68}$$

$$\dot{\omega} = \frac{d\omega}{d\tau}\frac{d\tau}{dt} = n^2\tilde{\omega}' \tag{2.69}$$

The system mass parameter is defined in Equation (2.51) and then the mass parameters for the primaries m_1 and m_2 are obtained as

$$\mu_2 = \mu \qquad\qquad \mu_1 = 1 - \mu \qquad\qquad (2.70)$$

where $\mu_s = \mu$. Thus, it is assumed that $0 < \mu < 0.5$ if $m_1 > m_2$. The scalar nondimensional equations of motion in the ER3BP then follow, expressed in terms of components in Frame S as,

$$\tilde{x}'' - 2\tilde{\omega}_{S/I}\tilde{y}' - \tilde{\omega}'_{S/I}\tilde{y} - \tilde{\omega}^2_{S/I}\tilde{x} = -(1-\mu)\frac{\tilde{x} + \tilde{R}_1}{\tilde{r}^3_1} - \mu\frac{\tilde{x} - \tilde{R}_2}{\tilde{r}^3_2} \qquad (2.71)$$

$$\tilde{y}'' + 2\tilde{\omega}_{S/I}\tilde{x}' + \tilde{\omega}'_{S/I}\tilde{x} - \tilde{\omega}^2_{S/I}\tilde{y} = -(1-\mu)\frac{\tilde{y}}{\tilde{r}^3_1} - \mu\frac{\tilde{y}}{\tilde{r}^3_2} \qquad (2.72)$$

$$\tilde{z}'' = -(1-\mu)\frac{\tilde{z}}{\tilde{r}^3_1} - \mu\frac{\tilde{z}}{\tilde{r}^3_2} \qquad (2.73)$$

Likewise, the ER3BP equations in terms of Frame M in nondimensional form are defined as

$$\tilde{x}'' - 2\tilde{\omega}_{M/I}\tilde{y}' - \tilde{\omega}'_{M/I}\tilde{y} - \tilde{\omega}^2_{M/I}\tilde{x} = -(1-\mu)\left(\frac{\tilde{x} - \tilde{r}_{12}}{\tilde{r}^3_1} + \frac{1}{\tilde{r}^2_{12}}\right) - \mu\frac{\tilde{x}}{\tilde{r}^3} \qquad (2.74)$$

$$\tilde{y}'' + 2\tilde{\omega}_{M/I}\tilde{x}' + \tilde{\omega}'_{M/I}\tilde{x} - \tilde{\omega}^2_{M/I}\tilde{y} = -(1-\mu)\frac{\tilde{y}}{\tilde{r}^3_1} - \mu\frac{\tilde{y}}{\tilde{r}^3} \qquad (2.75)$$

$$\tilde{z}'' = -(1-\mu)\frac{\tilde{z}}{\tilde{r}^3_1} - \mu\frac{\tilde{z}}{\tilde{r}^3} \qquad (2.76)$$

There are advantages to analysis based in the ER3BP in either frame S and frame M, largely dependent on the type of application. Selected orbits in close proximity to the second primary can employ the M frame since it is expected that the spacecraft position is measured from the m_2 and not the barycenter B. Moreover, nondimensional quantities are useful since they alleviate computational expense by parameterizing equations with respect to one value, namely μ. For simplicity, the tilde sign ($\tilde{x}$) is dropped from equations with the understanding that all quantities are nondimensional. For reference, characteristic quantities for the Earth-Moon and Sun-Earth system are listed in Table 2.2.

Table 2.2.
Characteristic Quantities for Nondimensionalization

System	distance a	total mass $m_1 + m_2$	mean motion n	sys. parameter μ
Earth-Moon	384400 km	6.0468e24 kg	2.6814e-6 rad/sec	0.01215
Sun-Earth	1.4965e8 km	1.9888e30 kg	1.98995e-7 rad/sec	3.00349e-6

2.2.1   Pseudo-potential Functions

The ER3BP equations of motion are further simplified by the introduction of a pseudo-potential functions. Recall the inertial potential function is defined as

$$U = \frac{1 - \mu}{r_1} + \frac{\mu}{r_2} \tag{2.77}$$

Equation (2.77) is modified such that

$$U_S^* = \frac{\omega_{S/I}^2}{2}(x^2 + y^2) + \frac{1 - \mu}{r_1} + \frac{\mu}{r_2} = \frac{\omega_{S/I}^2}{2}(x^2 + y^2) + U \tag{2.78}$$

$$U_M^* = \frac{\omega_{M/I}^2}{2}(x^2 + y^2) + (1 - \mu)\left(\frac{1}{r_1} - \frac{x}{r_{12}}\right) + \frac{\mu}{r}$$

$$= \frac{\omega_{M/I}^2}{2}(x^2 + y^2) - (1 - \mu)\frac{x}{r_{12}} + U \tag{2.79}$$

where U_S^* and U_M^* are the pseudo-potential functions for frames S and M, respectively. Therefore, Equations (2.71) - (2.73) in frame S is expressed as

$$x'' - 2\omega_{S/I}y' - \omega'_{S/I}y = \frac{\partial U_S^*}{\partial x} \tag{2.80}$$

$$y'' + 2\omega_{S/I}x' + \omega'_{S/I}x = \frac{\partial U_S^*}{\partial y} \tag{2.81}$$

$$z'' = \frac{\partial U_S^*}{\partial z} \tag{2.82}$$

Likewise, Equations (2.74) - (2.76) in frame M are rewritten as

$$x'' - 2\omega_{M/I}y' - \omega'_{M/I}y = \frac{\partial U^*_M}{\partial x} \tag{2.83}$$

$$y'' + 2\omega_{M/I}x' + \omega'_{M/I}x = \frac{\partial U^*_M}{\partial y} \tag{2.84}$$

$$z'' = \frac{\partial U^*_M}{\partial z} \tag{2.85}$$

The pseudo-potential functions are used to develop system matrices to formulate the equations of motion is state space form. As a result, first order variational equations are obtained to construct differential corrections schemes to target states in frames S and M.

2.3 Circular Restricted 3-Body Problem

A further assumption in addition to those governing the ER3BP delivers an additional formulation of the restricted three-body problem, the CR3BP. The primaries m_1 and m_2 are already assumed to move on a Keplerian orbit. Now, the conic motion is further assumed to be circular orbits about their common barycenter. Under this assumption, there are two main simplications:

- The nondimensional angular velocity for both synodic frames S and M are $\omega_{S/I} = \omega_{M/I} = 1$

- The distance between the two primaries is constant, thus

$$\mathbf{R}_1 = -\mu\hat{\mathbf{x}}_s \qquad \mathbf{R}_2 = (1-\mu)\hat{\mathbf{x}}_s \qquad \mathbf{r}_{12} = \hat{\mathbf{x}}_s = -\hat{\mathbf{x}}_m \tag{2.86}$$

A depiction of the CR3BP appears in Figure 2.6, where the orbits of the primaries are now circular about barycenter B. Equations (2.71) - (2.73) in the S frame are reduced to

$$x'' - 2y' - x = -(1 - \mu)\frac{x + \mu}{r_1^3} - \mu\frac{x - 1 + \mu}{r_2^3} \tag{2.87}$$

$$y'' + 2x' - y = -(1 - \mu)\frac{y}{r_1^3} - \mu\frac{y}{r_2^3} \tag{2.88}$$

$$z'' = -(1 - \mu)\frac{z}{r_1^3} - \mu\frac{z}{r_2^3} \tag{2.89}$$

where,

$$r_1 = \sqrt{(x + \mu)^2 + y^2 + z^2} \qquad r_2 = \sqrt{(x - 1 + \mu)^2 + y^2 + z^2} \tag{2.90}$$

Likewise, Equations (2.74) - (2.76) in the M frame then become

$$x'' - 2y' - x = -(1 - \mu)\left(\frac{x - 1}{r_1^3} + 1\right) - \mu\frac{x}{r^3} \tag{2.91}$$

$$y'' + 2x' - y = -(1 - \mu)\frac{y}{r_1^3} - \mu\frac{y}{r^3} \tag{2.92}$$

$$z'' = -(1 - \mu)\frac{z}{r_1^3} - \mu\frac{z}{r^3} \tag{2.93}$$

where,

$$r_1 = \sqrt{(x - 1)^2 + y^2 + z^2} \qquad r = \sqrt{x^2 + y^2 + z^2} \tag{2.94}$$

The CR3BP assumes that both the distances between the primaries and the nondimensional angular velocity of frames S and M remain constant, greatly simplifying the equations of motion. Moreover, Equations (2.91) - (2.93) are time-invariant which classifies the CR3BP as an autonomous system. As a result, any solution obtained in the CR3BP is valid for any point in time, both past and future.
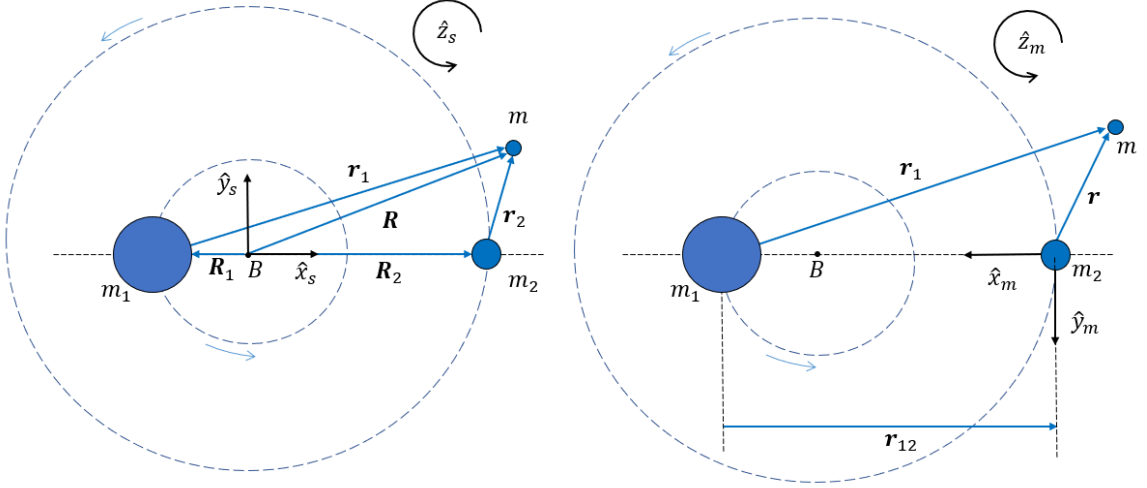
Fig. 2.6. Diagram of the CR3BP in synodic frames S (left) and M (right).

2.3.1 Pseudo-potential Functions

Given the circular assumption for the orbits of the two primaries, pseudo-potential functions in Equations (2.78) and (2.79) are also simplified to obtain

$$\Omega_S^* = \frac{1}{2}(x^2 + y^2) + \frac{1-\mu}{r_1} + \frac{\mu}{r_2} = \frac{1}{2}(x^2 + y^2) + U \tag{2.95}$$

$$\Omega_M^* = \frac{1}{2}(x^2 + y^2) + (1-\mu)\left(\frac{1}{r_1} - x\right) + \frac{\mu}{r}$$

$$= \frac{1}{2}(x^2 + y^2) - (1-\mu)x + U \tag{2.96}$$

where Ω_S^* and Ω_M^* denote the CR3BP pseudo-potential function in frames S and M, respectively. Equations (2.80) - (2.82) in frame S are then expressed as

$$x'' - 2y' = \frac{\partial \Omega_S^*}{\partial x} \tag{2.97}$$

$$y'' + 2x' = \frac{\partial \Omega_S^*}{\partial y} \tag{2.98}$$

$$z'' = \frac{\partial \Omega_S^*}{\partial z} \tag{2.99}$$

Likewise, Equations 2.83 - 2.85 in frame M are given as

$$x'' - 2y' = \frac{\partial \Omega_M^*}{\partial x} \tag{2.100}$$

$$y'' + 2x' = \frac{\partial \Omega_M^*}{\partial y} \tag{2.101}$$

$$z'' = \frac{\partial \Omega_M^*}{\partial z} \tag{2.102}$$

The formulation of pseudo-potential functions in the CR3BP facilitate the derivation of the model's only integral of the motion. To admit an analytical solution, six integrals of the motion must exist for the equations of motion in the rotating frame. In fact, there is only one integral of the motion for the CR3BP so numerical integration is required to obtain a time history of spacecraft m.

2.3.2   Jacobi Constant

The CR3BP, as formulated in the rotating synodic frame, admits an integral of motion since it is regarded as a conservative system. Given that the pseudo-potential Ω^* is an time-invariant potential function, operating on the equations of motion yields an energy-like constant. An approach to produce this constant is similar to the derivation of the specific energy constant $\mathcal{E}$ in the two-body problem. First, a dot product between the spacecraft velocity and acceleration vectors in the S frame yields

$$\mathbf{r}' \cdot \mathbf{r}'' = x'x'' + y'y'' + z'z'' = \frac{\partial \Omega_S^*}{\partial x}x' + \frac{\partial \Omega_S^*}{\partial y}y' + \frac{\partial \Omega_S^*}{\partial z}z' + \frac{\partial \Omega_S^*}{\partial \tau} \tag{2.103}$$

where the value $\frac{\partial \Omega_S^*}{\partial \tau}$ simplifies to zero, since the pseudo-potential function is derived in an autonomous system. Scalar integration of Equation (2.103), yields

$$\int \mathbf{r}' \cdot \mathbf{r}'' d\tau = \frac{1}{2}(x'^2 + y'^2 + z'^2) = \Omega_S^* - J \tag{2.104}$$

$$J = 2\Omega_S^* - v^2 \tag{2.105}$$

where v is the magnitude of spacecraft velocity, i.e. speed, as observed in the rotating frame S and J is denoted the Jacobi constant. The Jacobi constant represents an energy-like quantity such that a decrease in J infers an increase in the spacecraft energy as observed in S. The Jacobi constant is used to determine the range of natural speeds available to a spacecraft given its unique position with respect to the primaries.

2.3.3 Equilibrium Solutions

Five equilibria determined from the CR3BP equations of motion are available as observed in the rotating frame. These solutions are usually denoted as the Lagrangian or libration points, with the first three identified in 1763 by Leonhard Euler (1707-1783) denoted as L_1, L_2 and L_3. These three collinear points lie along the $\hat{\mathbf{x}}_s$ on the line between the two primaries. In 1772, Lagrange produced the last two equilibrium solutions L_4 and L_5, denoted as the equilateral points. To locate these points, the vector gradient of the pseudo-potential function is set to zero, $\nabla \Omega_S^* = 0$, such that three scalar equations are obtained as

$$-(1 - \mu)\frac{(x_{eq} + \mu)}{r_1^3} - \mu\frac{(x_{eq} - 1 + \mu)}{r_2^3} + x_{eq} = 0 \tag{2.106}$$

$$-(1 - \mu)\frac{y_{eq}}{r_1^3} - \mu\frac{y_{eq}}{r_2^3} + y_{eq} = 0 \tag{2.107}$$

$$-(1 - \mu)\frac{z_{eq}}{r_1^3} - \mu\frac{z_{eq}}{r_2^3} = 0 \tag{2.108}$$

where x_{eq}, y_{eq}, and z_{eq} represent the positions of the equilibrium points as measured from the barycenter B in frame S. The equilibrium solutions must simultaneously satisfy Equations (2.106) - (2.108). From first glance, it is apparent that $z_{eq} = 0$ satisfies all the equations placing the equilibrium points in the $\hat{\mathbf{x}}_s - \hat{\mathbf{y}}_s$ plane. The collinear points are computed by setting $y_{eq} = z_{eq} = 0$ and, then, solving for the roots of the Equation (2.106). Since there are no analytical solutions for this equation, these points must be computed numerically. Szebehely [18] offers a series expansion to approximate the L_1 and L_2 locations by defining

$$\gamma_1 = r_h \left(1 - \frac{1}{3} r_h - \frac{1}{9} r_h^2 + ... \right) \tag{2.109}$$

$$\gamma_2 = r_h \left(1 + \frac{1}{3} r_h + \frac{1}{9} r_h^2 + ... \right) \tag{2.110}$$

where $r_h = \sqrt[3]{\mu/3}$ is Hill's radius which approximates the smaller primary's gravitational sphere of influence subject to perturbations from the larger primary. Consequently, γ_1 and γ_2 are the distances from L_1 and L_2 to primary m_2, respectively. The two remaining equilateral points are evaluated by setting $r_1 = r_2 = 1$, which form an equilateral triangle with primaries m_1 and m_2 as two of the vertices. Figure 2.7 depicts the locations of all five equilibria for CR3BP. Although all the libration points satisfy Equations (2.106) - (2.108), they do not all emerge simultaneously. In fact, they are numbered such that they are consistent with the order at which they become accessible with decreasing values of Jacobi constant or

$$J_{L_1} > J_{L_2} > J_{L_3} > J_{L_4} = J_{L_5} \tag{2.111}$$

In other words, more libration points emerge as the orbital energy of the spacecraft increases. It is worth noting that L_4 and L_5 emerge at the same Jacobi constant value as a consequence of the mirror theorem. Nevertheless, L_4 by convention denotes the libration point ahead of the line between the primaries in their rotation whereas L_5

trails behind. Table 2.3 summarizes the locations of all the libration points for the Earth-Moon and Sun-Earth systems.
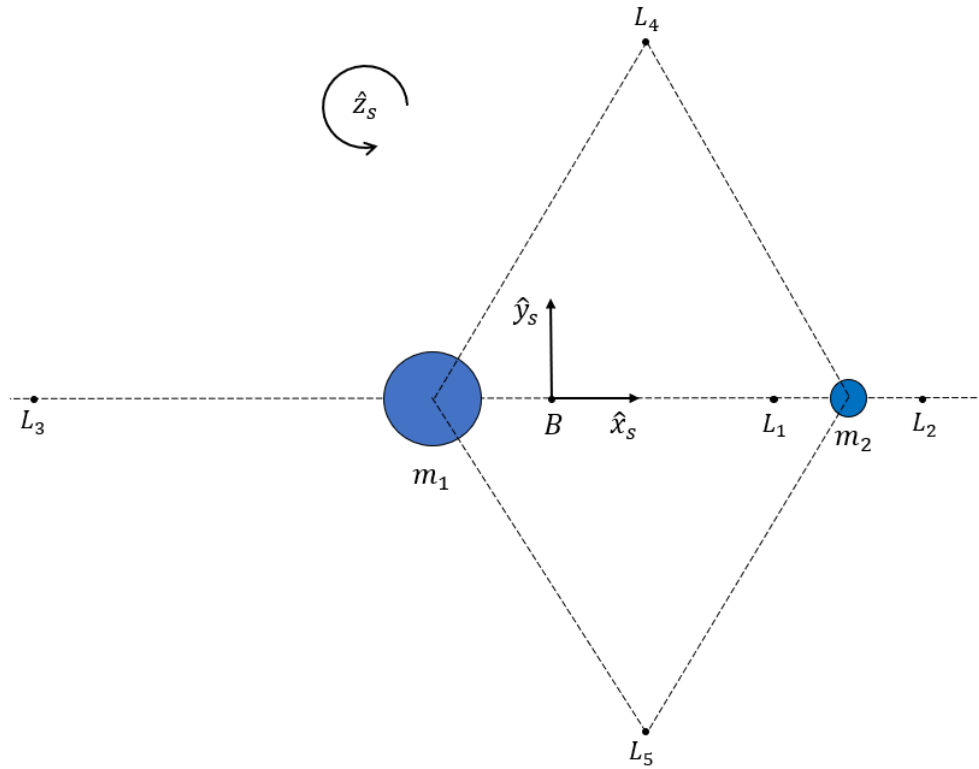
Fig. 2.7. Positions of the Libration Points in Frame S.

Table 2.3.
Libration Point Positions for Different Systems

System	$L_1[x,y]$ (nd)	$L_2[x,y]$ (nd)	$L_3[x,y]$ (nd)	$L_4[x,y]$ (nd)	$L_5[x,y]$ (nd)
Earth-Moon	$[0.8369\ 0]$	$[1.1557\ 0]$	$[-1.0051\ 0]$	$[0.4878\ 0.866]$	$[0.4878\ -0.866]$
Sun-Earth	$[0.99\ 0]$	$[1.01\ 0]$	$[-1.0\ 0]$	$[0.5\ 0.866]$	$[0.5\ -0.866]$

2.3.4 Zero Velocity Surfaces

The Jacobi constant J is also employed to compute bounds on the spacecraft accessible regions given the position in the rotating frame. These bounds are visualized as surfaces in configuration space, originating from its relationship with the spacecraft speed as expressed in Equation (2.105). Since spacecraft speed is by definition non-imaginary, an inequality is formulated by setting $v = 0$ to obtain

$$2\Omega_S^* >= J \tag{2.112}$$

where the pseudo-potential Ω_S^* places bounds on the spacecraft position for a given value of the Jacobi constant. The locus of points where $v = 0$ admits a three-dimensional surface labelled a Zero-Velocity Surface (ZVS). Areas bounded by the surfaces introduce forbidden regions since $v < 0$ for a spacecraft to realistically access these areas of space. If a slice of the ZVS is taken at $z = 0$, the curve obtained is denoted the Zero-Velocity Curve (ZVC). As previously mentioned, the libration points emerge at different energy levels according to the pseudo-potential Ω_S^* and the spacecraft velocity. Table 2.4 lists approximate Jacobi constant values where each of the libration points L_i emerge for different systems.

Table 2.4.
Libration Point Jacobi Constants for Different Systems

System	L_1 (nd)	L_2 (nd)	L_3 (nd)	L_4 (nd)	L_5 (nd)
Earth-Moon	3.1883	3.1722	3.0122	2.9880	2.9880
Sun-Earth	3.0422	3.0403	3.0002	2.9998	2.9998

Figure 2.8 plots sample ZVS and ZVC for the Earth-Moon system at a Jacobi constant value such that

$$J_{L_2} > J > J_{L_3}$$

In this example, it is observed that the set Jacobi constant value for the spacecraft at $J = 3.05$ is sufficiently low enough such that L_1 and L_2 are accessible in cislunar space. The boundaries of the accessible regions available to the spacecraft appear in purple whereas the white spaces contain the forbidden regions. At this energy level, the spacecraft possibly escapes the Earth-Moon system although it is impossible to predict when or if this occurs. Nevertheless, at this Jacobi constant value, these surfaces provide some insight regarding the dynamical flow in the system by extracting the forbidden regions as the space bound by the ZVC in two-dimensional space and the ZVS in three-dimensional space.
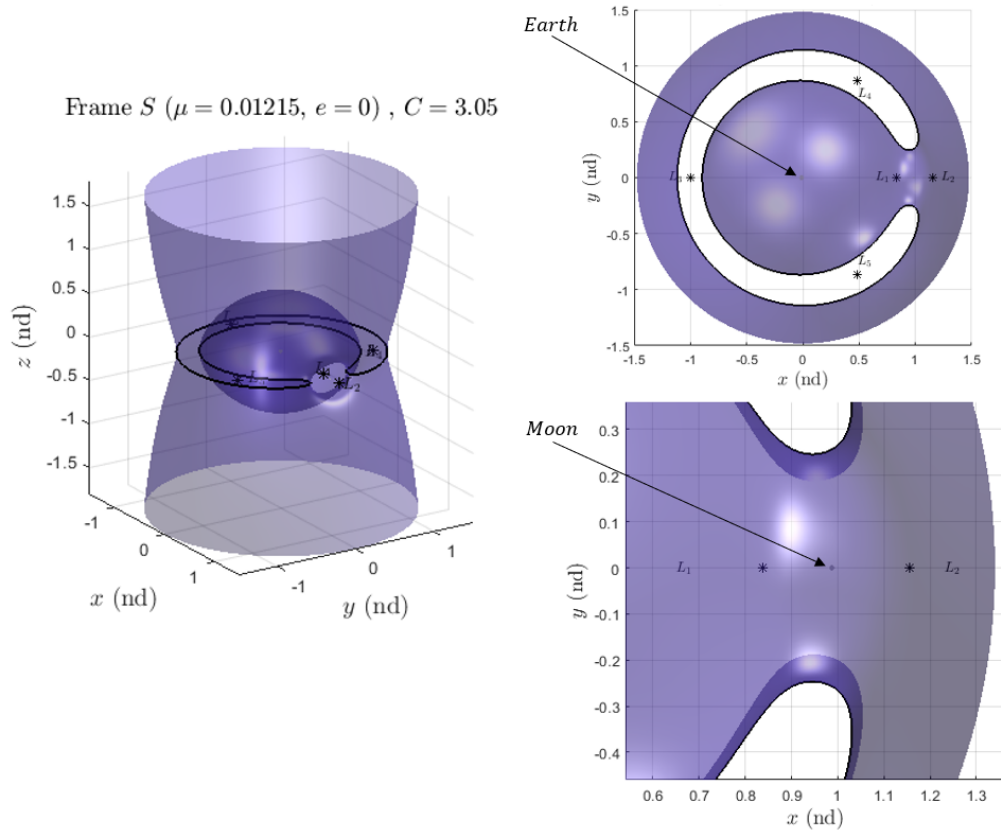
Fig. 2.8. ZVS boundaries (purple) and ZVC (black) case in the Earth-Moon system

Consequently, the ZVCs for six different Jacobi constants are plotted in Figure 2.9, where each case accesses more of the space until no forbidden region remain.
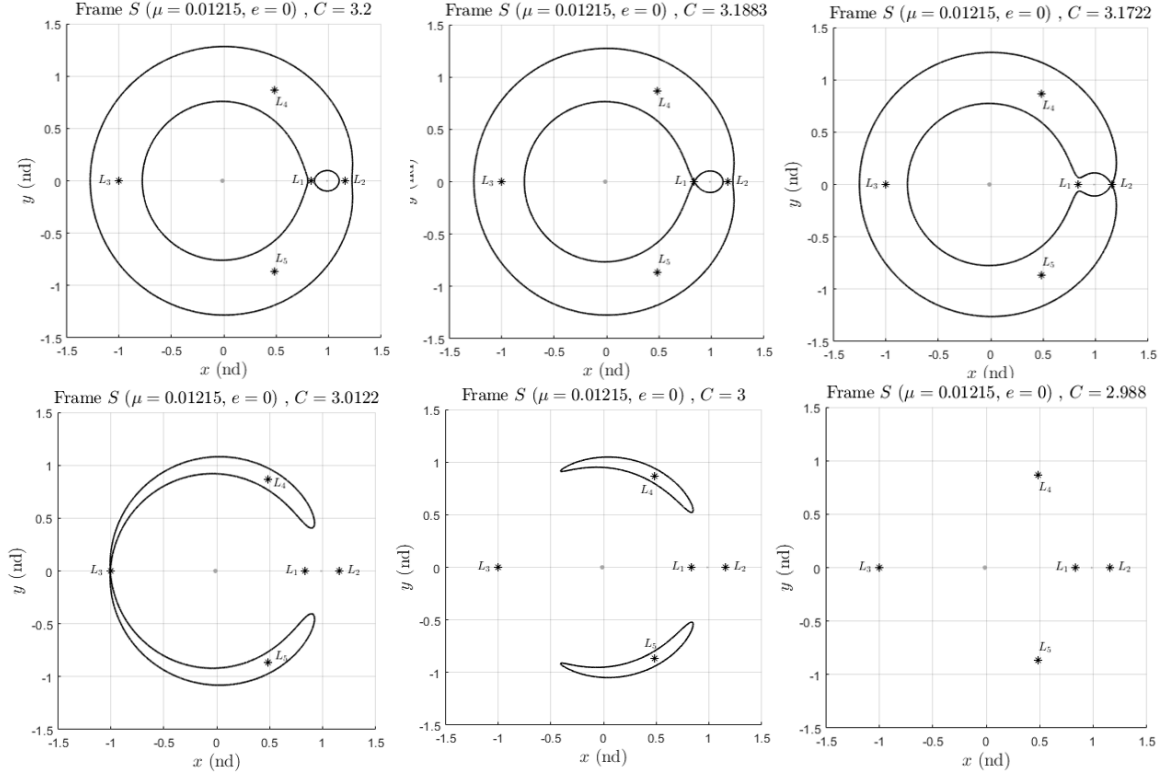
Fig. 2.9. Zero-Velocity Curves Progression for the Earth-Moon System

The ZVCs are obtained by taking a slice of the ZVS at $z = 0$ for different energy levels. At the highest level of the Jacobi constant value (top-left of Figure 2.9), two regions emerge around the primaries, an interior region around the Earth and an exterior region around the Moon, yet they do not connect. An increase in spacecraft energy, synonymous with a decrease in Jacobi constant value, opens a pathway at L_1 (top-middle of Figure 2.9) connecting the two regions around the primaries. As the Jacobi constant value decreases further such that $J < J_{L_2}$, a second pathway emerges at L_2 (top-right of Figure 2.9) offering a possible escape path from the system. For this reason, Szebehely [18] concludes that is easier to leave the Earth-Moon system through passage by the Moon or the Sun-Earth system by the Earth. Further decreases in

the Jacobi constant value allows passage to L_3 (bottom-left of Figure 2.9) and the L_4, L_5 points (bottom-middle of Figure 2.9) until the forbidden regions bounded by the ZVCs in the $\hat{\mathbf{x}}_s - \hat{\mathbf{y}}_s$ plane disappear rendering the entire space accessible (bottom-right of Figure 2.9). It is worth noting that although the ZVCs in the $\hat{\mathbf{x}}_s - \hat{\mathbf{y}}_s$ plane disappear, there still remain inaccessible regions in the three-dimensional space above and below the plan of the primaries.

2.3.5 Symmetry

Producing solutions of interest in the CR3BP, including periodic orbits, are enabled by exploiting a useful symmetry property admitted by the equations of motion. Suppose a set of coordinates $(x^\alpha, y^\alpha, z^\alpha)$ are defined such that $x^\alpha(\tau^\alpha) = x(\tau)$, $y^\alpha(\tau^\alpha) = -y(\tau)$, and $z^\alpha(\tau^\alpha) = z(\tau)$. The time variable τ^α is defined such that

$$\frac{d}{d\tau^\alpha} = -\frac{d}{d\tau}$$
$$\frac{d^2}{d\tau^{\alpha 2}} = -\frac{d^2}{d\tau^2}$$

Thus, it is apparent that the new set of coordinates *mirrors* the formulated set (x, y, z) across the $\hat{\mathbf{x}}_s - \hat{\mathbf{z}}_s$ plane in reverse time. Substituting the new coordinate set into Equation (2.97) - (2.99) yields

$$\frac{d^2 x^\alpha}{d\tau^{\alpha 2}} + 2\frac{dy^\alpha}{d\tau^\alpha} = \frac{\partial \Omega_S^*}{\partial x^\alpha} \tag{2.113}$$

$$\frac{d^2 y^\alpha}{d\tau^{\alpha 2}} - 2\frac{dx^\alpha}{d\tau^\alpha} = \frac{\partial \Omega_S^*}{\partial y^\alpha} \tag{2.114}$$

$$\frac{d^2 z^\alpha}{d\tau^{\alpha 2}} = \frac{\partial \Omega_S^*}{\partial z^\alpha} \tag{2.115}$$

Equations (2.113) - (2.115) admit a structure exact to Equations (2.97) - (2.99); therefore, any solution obtained in the CR3BP also admits a solution mirrored across the $\hat{\mathbf{x}}_s - \hat{\mathbf{z}}_s$ plane. Roy et al. [25] summarizes this result by postulating the mirror theorem.

Theorem 2.1.1 (Mirror Theorem): *If n point masses are acted upon by their mutual gravitational forces only, and at a certain epoch each radius vector from the center of mass of the system is perpendicular to every velocity vector, then the orbit of each mass after that epoch is a mirror image of its orbit prior to that epoch.*

The mirror theorem will be employed in section 2.4.1 to obtain periodic solutions in the CR3BP by targeting perpendicular crossings along the $\hat{\mathbf{x}}_s - \hat{\mathbf{z}}_s$ plane.

2.4 Differential Corrections

The CR3BP problem does not admit an analytical, closed-form solution. As a result, numerical techniques , e.g., differential corrections and shooting algorithms, are employed to facilitate the computation of solutions. As a dynamical system, the CR3BP is chaotic meaning that any slight variations in the initial state result in larger variations downstream. In this section, corrections strategies based on multi-variable Newton methods are addressed and applied to a boundary value problem subject to a given set of constraints.

2.4.1 State Transition Matrix

Any application of differential corrections requires an assessment of the sensitivities of the variables. A key element in such a process is to relate variations in the initial state $\mathbf{x}(\tau_0)$ to variations downstream at $\mathbf{x}(\tau, \mathbf{x}(\tau_0))$. The system equations of motion are of the form $\mathbf{x}'(\tau) = \mathbf{f}(\tau, \mathbf{x}(\tau), \boldsymbol{\beta})$ where the state vector is $\mathbf{x}(\tau) = [x(\tau)\ \ y(\tau)\ \ z(\tau)\ \ x'(\tau)\ \ y'(\tau)\ \ z'(\tau)]^T$ and $\boldsymbol{\beta}$ represents a vector of parameters and constants pertaining to the system of interest. Although not exclusive to any particular coordinate frame representation, the following analysis assumes that variables and derivatives are taken with respect to Frame S. Thus, the state vector contains position and velocity coordinates relative to the system barycenter B. If the equations in Frame M are employed for the analysis, the state vector includes position and velocity information

for position vectors originating relative to the second primary m_2. In either case, the vector variation relative to some reference trajectory is defined as

$$\delta\mathbf{x}(\tau) = \mathbf{x}(\tau) - \mathbf{x}^*(\tau) \tag{2.116}$$

where $\mathbf{x}^*(\tau)$ indicates the state pertaining to the reference trajectory at time τ and $\mathbf{x}(\tau)$ represents the state on a path in close proximity to the reference solution. Employing a first-order Taylor expansion relative to the reference trajectory, the linear variational equations of motion are written as

$$\delta\mathbf{x}'(\tau) = \frac{\partial\mathbf{f}(\tau, \mathbf{x}(\tau), \beta)}{\partial\mathbf{x}(\tau)}\delta\mathbf{x}(\tau) = \mathbf{A}(\tau)\delta\mathbf{x}(\tau) \tag{2.117}$$

where $\mathbf{A}(\tau)$ is termed the Jacobian matrix comprised of the associated partials pertaining to the equations of motion evaluated on the reference trajectory. Equation (2.117) admits a linear solution in the form of a matrix derivative relating variations between variables from the initial to final state. Mathematically, the linear solution is expressed as

$$\delta\mathbf{x}(\tau) = \left(\frac{\partial\mathbf{x}(\tau)}{\partial\mathbf{x}(\tau_0)}\right)\delta\mathbf{x}(\tau_0) \tag{2.118}$$

To determine the components of the matrix derivative, a first-order differential equation is formulated such that

$$\frac{d}{d\tau}\left(\frac{\partial\mathbf{x}(\tau)}{\partial\mathbf{x}(\tau_0)}\right) = \frac{d}{d\mathbf{x}(\tau_0)}\left(\frac{\partial\mathbf{x}(\tau)}{\partial\tau}\right) = \frac{d}{d\mathbf{x}(\tau_0)}\mathbf{x}'(\tau) \tag{2.119}$$

Since $\mathbf{x}(\tau_0)$ and τ are independent, they may be interchanged in Equation (2.119). Consequently, the chain rule is employed to produce

$$\frac{d}{d\tau}\left(\frac{\partial\mathbf{x}(\tau)}{\partial\mathbf{x}(\tau_0)}\right) = \frac{d}{d\mathbf{x}(\tau_0)}\mathbf{x}'(\tau) = \frac{\partial\mathbf{f}(\tau, \mathbf{x}(\tau), \beta)}{\partial\mathbf{x}(\tau)}\frac{\partial\mathbf{x}(\tau)}{\partial\mathbf{x}(\tau_0)} = \mathbf{A}(\tau)\frac{\partial\mathbf{x}(\tau)}{\partial\mathbf{x}(\tau_0)} \tag{2.120}$$

The state transition matrix (STM) $\boldsymbol{\Phi}$ is defined as the derivative matrix relating initial variations in the state to those downstream, that is

$$\boldsymbol{\Phi}(\tau,\tau_0) = \frac{\partial \mathbf{x}(\tau)}{\partial \mathbf{x}(\tau_0)} = \begin{bmatrix} \frac{\partial x}{\partial x_0} & \frac{\partial x}{\partial y_0} & \frac{\partial x}{\partial z_0} & \frac{\partial x}{\partial x_0'} & \frac{\partial x}{\partial y_0'} & \frac{\partial x}{\partial z_0'} \\ \frac{\partial y}{\partial x_0} & \frac{\partial y}{\partial y_0} & \frac{\partial y}{\partial z_0} & \frac{\partial y}{\partial x_0'} & \frac{\partial y}{\partial y_0'} & \frac{\partial y}{\partial z_0'} \\ \frac{\partial z}{\partial x_0} & \frac{\partial z}{\partial y_0} & \frac{\partial z}{\partial z_0} & \frac{\partial z}{\partial x_0'} & \frac{\partial z}{\partial y_0'} & \frac{\partial z}{\partial z_0'} \\ \frac{\partial x'}{\partial x_0} & \frac{\partial x'}{\partial y_0} & \frac{\partial x'}{\partial z_0} & \frac{\partial x'}{\partial x_0'} & \frac{\partial x'}{\partial y_0'} & \frac{\partial x'}{\partial z_0'} \\ \frac{\partial y'}{\partial x_0} & \frac{\partial y'}{\partial y_0} & \frac{\partial y'}{\partial z_0} & \frac{\partial y'}{\partial x_0'} & \frac{\partial y'}{\partial y_0'} & \frac{\partial y'}{\partial z_0'} \\ \frac{\partial z'}{\partial x_0} & \frac{\partial z'}{\partial y_0} & \frac{\partial z'}{\partial z_0} & \frac{\partial z'}{\partial x_0'} & \frac{\partial z'}{\partial y_0'} & \frac{\partial z'}{\partial z_0'} \end{bmatrix} = \begin{bmatrix} \phi_{11} & \phi_{12} & \phi_{13} & \phi_{14} & \phi_{15} & \phi_{16} \\ \phi_{21} & \phi_{22} & \phi_{23} & \phi_{24} & \phi_{25} & \phi_{26} \\ \phi_{31} & \phi_{32} & \phi_{33} & \phi_{34} & \phi_{35} & \phi_{36} \\ \phi_{41} & \phi_{42} & \phi_{43} & \phi_{44} & \phi_{45} & \phi_{46} \\ \phi_{51} & \phi_{52} & \phi_{53} & \phi_{54} & \phi_{55} & \phi_{56} \\ \phi_{61} & \phi_{62} & \phi_{63} & \phi_{64} & \phi_{65} & \phi_{66} \end{bmatrix}$$

$$(2.121)$$

Moreover, the first-order matrix differential equation governing the STM over time is written as

$$\boldsymbol{\Phi}'(\tau,\tau_0) = \mathbf{A}(\tau)\boldsymbol{\Phi}(\tau,\tau_0) \tag{2.122}$$

It is apparent from Equation (2.122) that the initial value of $\boldsymbol{\Phi}$ at τ_0 is the identity matrix $\mathbf{I}_{6\times6}$. The individual elements of the STM are derived from the linear variational equations of motion with respect to a baseline or reference solution. The differential equations governing the behavior of these variations follow as

$$\delta x'' - 2\delta y' = \Omega_{S,xx}^*\delta x + \Omega_{S,xy}^*\delta y + \Omega_{S,xz}^*\delta z \tag{2.123}$$

$$\delta y'' + 2\delta x' = \Omega_{S,yx}^*\delta x + \Omega_{S,yy}^*\delta y + \Omega_{S,yz}^*\delta z \tag{2.124}$$

$$\delta z'' = \Omega_{S,zx}^*\delta x + \Omega_{S,zy}^*\delta y + \Omega_{S,zz}^*\delta z \tag{2.125}$$

The above equations then form the system matrix $\mathbf{A}(\tau)$ as

$$\mathbf{A}(\tau) = \begin{bmatrix} 0 & 0 & 0 & 1 & 0 & 0 \\ 0 & 0 & 0 & 0 & 1 & 0 \\ 0 & 0 & 0 & 0 & 0 & 1 \\ \Omega_{S,xx}^* & \Omega_{S,xy}^* & \Omega_{S,xz}^* & 0 & 2 & 0 \\ \Omega_{S,yx}^* & \Omega_{S,yy}^* & \Omega_{S,yz}^* & -2 & 0 & 0 \\ \Omega_{S,zx}^* & \Omega_{S,zy}^* & \Omega_{S,zz}^* & 0 & 0 & 0 \end{bmatrix} \tag{2.126}$$

The scalar partial derivatives in $\mathbf{A}(\tau)$ are evaluated as

$$\Omega^*_{S,xx} = \frac{\partial \Omega^*_S}{\partial x \partial x} = 1 - \frac{1-\mu}{r_1^3} - \frac{\mu}{r_2^3} + \frac{3(1-\mu)(x+\mu)^2}{r_1^5} + \frac{3\mu(x-1+\mu)^2}{r_2^5} \qquad (2.127)$$

$$\Omega^*_{S,yy} = \frac{\partial \Omega^*_S}{\partial y \partial y} = 1 - \frac{1-\mu}{r_1^3} - \frac{\mu}{r_2^3} + \frac{3(1-\mu)y^2}{r_1^5} + \frac{3\mu y^2}{r_2^5} \qquad (2.128)$$

$$\Omega^*_{S,zz} = \frac{\partial \Omega^*_S}{\partial z \partial z} = 1 - \frac{1-\mu}{r_1^3} - \frac{\mu}{r_2^3} + \frac{3(1-\mu)z^2}{r_1^5} + \frac{3\mu z^2}{r_2^5} \qquad (2.129)$$

$$\Omega^*_{S,xy} = \Omega^*_{S,yx} = \frac{\partial \Omega^*_S}{\partial x \partial y} = \frac{3(1-\mu)(x+\mu)y}{r_1^5} + \frac{3\mu(x-1+\mu)y}{r_2^5} \qquad (2.130)$$

$$\Omega^*_{S,xz} = \Omega^*_{S,zx} = \frac{\partial \Omega^*_S}{\partial x \partial z} = \frac{3(1-\mu)(x+\mu)z}{r_1^5} + \frac{3\mu(x-1+\mu)z}{r_2^5} \qquad (2.131)$$

$$\Omega^*_{S,yz} = \Omega^*_{S,zy} = \frac{\partial \Omega^*_S}{\partial y \partial z} = \frac{3(1-\mu)yz}{r_1^5} + \frac{3\mu yz}{r_2^5} \qquad (2.132)$$

where r_1 and r_2 denote the magnitudes of the nondimensional position vectors as measured in frame S from primaries m_1 and m_2, respectively.

2.4.2 Monodromy Matrix

If the STM is evaluated over precisely one orbital period and is observed as a fixed point on a stroboscopic map, the STM is labelled the monodromy matrix denoted as $\mathbf{\Phi}(t_0 + P, t_0)$. The monodromy matrix $\mathscr{M}$ possesses the following properties:

1. It possesses eigenvalues that emerge in reciprocal pairs

2. The determinate of $\mathscr{M} \to \det \mathbf{\Phi}(t_0 + P, t_0)$ is equal to unity

3. $\mathscr{M}$ is symplectic

Many applications in the CR3BP involve the momodromy matrix $\mathscr{M}$, one of which includes the assessment of orbital stability in a linear sense. Since it contains discrete-time information, the $\mathscr{M}$ stability boundary is the unit circle and the eigenvalues λ_i, provide information regarding the stability of the reference solution. A summary of the eigenvalues and their classifications in a linear and a nonlinear context is summarized in Table 2.5.

Table 2.5.
Monodromy Matrix Eigenvalue Decomposition & Stability Characteristics

Eigenvalue Conditions	Linear Stability Assessment	Nonlinear Stability Result
All $\lambda_i < 0$	Asymptotically Stable	Asymptotically Stable
One $\lambda_i > 0$	Unstable	Unstable
All $\lambda_i = 1$	Marginally Stable	Unknown

Periodic orbits that exist in the CR3BP possess two eigenvalues equal to unity indicating (i) the orbit periodicity and (ii) the orbit membership as part of a collective family of solutions with similar characteristics. As periodic orbits are computed along a family, changes in stability occur as determined by eigenvalues that may indicate the presence of a bifurcation to a new family of solutions. A more detailed analysis regarding bifurcations in the CR3BP is given by Zimovan et al. [26] and Bosanac [27].

2.4.3   Shooting Algorithms

Differential corrections techniques are an invaluable tool for multi-body trajectory design. In particular, they are used to vary design variables to construct specified orbit geometries subject to a set of constraints. Consider the design variable vector $\mathbf{X}$ defined as

$$\mathbf{X} = \begin{bmatrix} X_1 \\ X_2 \\ \vdots \\ X_n \end{bmatrix} \tag{2.133}$$

In this formulation, there are n design variables in vector $\mathbf{X}$ that includes variables representing, e.g., state elements and times of flight. The design variables are iterated subject to a set of m constraints contained in the constraint vector $\mathbf{F}(\mathbf{X})$ or

$$\mathbf{F}(\mathbf{X}) = \begin{bmatrix} F_1(\mathbf{X}) \\ F_2(\mathbf{X}) \\ \vdots \\ F_m(\mathbf{X}) \end{bmatrix} = \mathbf{0} \tag{2.134}$$

Constraints are parameterized using e.g., position, velocity, and TOF elements and there exist numerous ways to formulate a wide variety of possible conditions depending on the application. The objective is to formulate an iteration process to a design state vector $\mathbf{X}^*$ such that $\mathbf{F}(\mathbf{X}^*) = \mathbf{0}$ or, more accurately, until all specified constraints meet a numerical tolerance. If the initial guess vector is denoted as $\mathbf{X}^0$, the constraint vector is expanded using a Taylor series about the initial guess such that

$$\mathbf{F}(\mathbf{X}) = \mathbf{F}(\mathbf{X}^0) + \frac{\partial \mathbf{F}(\mathbf{X}^0)}{\partial \mathbf{X}^0}(\mathbf{X} - \mathbf{X}^0) + \cdots \tag{2.135}$$

where $\frac{\partial \mathbf{F}(\mathbf{X}^0)}{\partial \mathbf{X}^0}$ or $D\mathbf{F}(\mathbf{X}^0)$ is defined as the Jacobian matrix with m rows and n columns. The elements of the Jacobian matrix comprise of the partial derivatives of the constraints with respect to the design variables. If Equation (2.135) is retained to only first order, then the equation simplifies to

$$\mathbf{0} = \mathbf{F}(\mathbf{X}) = \mathbf{F}(\mathbf{X}^0) + D\mathbf{F}(\mathbf{X}^0)(\mathbf{X} - \mathbf{X}^0) \tag{2.136}$$

Equation (2.136) is rewritten using the iterative update form such that

$$\mathbf{0} = \mathbf{F}(\mathbf{X}^j) + D\mathbf{F}(\mathbf{X}^j)(\mathbf{X}^{j+1} - \mathbf{X}^j) \tag{2.137}$$

where $\mathbf{X}^j$ indicates the current iteration of the design variable vector along with the corresponding value of $\mathbf{F}(\mathbf{X}^j)$. Likewise, $\mathbf{X}^{j+1}$ refers to the next iteration of the design variable vector. The iteration process continues until $\mathbf{X}^{j+1}$ produces $\mathbf{F}(\mathbf{X}^{j+1}) = \mathbf{F}(\mathbf{X}^*) = \mathbf{0}$ or within some specified numerical tolerance. In this investigation, the numerical tolerance for the condition on the constraint vector follows as $||\mathbf{F}(\mathbf{X}^{j+1})|| <$

10^{-12} where the norm employed is the L^2 norm or square root of the sum of the squares of the elements also known as the Euclidean norm. Note that the state variables in this formulation are nondimensional. Equation (2.137) is rearranged to solve for the design vector $\mathbf{X}^{j+1}$ to obtain

$$\mathbf{X}^{j+1} = \mathbf{X}^j - D\mathbf{F}(\mathbf{X}^j)^{-1}\mathbf{F}(\mathbf{X}^j) \tag{2.138}$$

Equation (2.138) operates under the assumption that $D\mathbf{F}(\mathbf{X}^j)$ is invertible, thus, providing an exact solution to the update design variable vector. Consequently, $D\mathbf{F}(\mathbf{X}^j)$ is invertible if and only if m constraints equal n free variables resulting in a square Jacobian matrix. If there are more design variables than constraints (that is $n > m$), the update equation admits an infinite number of solutions. Typically, the minimum norm solution is sometimes employed as it seeks the solution $\mathbf{X}^{j+1}$ that is closest to the initial guess $\mathbf{X}^j$. As a result, the final solution $\mathbf{X}^*$ is as close as possible to $\mathbf{X}^0$ and, thus, retains similar characteristics as the initial design variable vector. If $D\mathbf{F}(\mathbf{X}^j)$ is not square, Equation (2.138) is modified to solve for the minimum norm solution by

$$\mathbf{X}^{j+1} = \mathbf{X}^j - D\mathbf{F}(\mathbf{X}^j)^T (D\mathbf{F}(\mathbf{X}^j)D\mathbf{F}(\mathbf{X}^j)^T)^{-1}\mathbf{F}(\mathbf{X}^j) \tag{2.139}$$

Both forms of the update equation from Equations (2.138) and (2.139) depend on the formulation of the design and constraint vectors. The onus is on the designer to select the free variables and constraint conditions for the application considered.

Single Shooting Algorithms

The simplest targeting scheme using differential corrections employs the single shooter method to obtain a solution to the two-point boundary value problem. Let the initial state be represented as

$$\mathbf{x}(\tau_0) = [x(\tau_0) \ \ y(\tau_0) \ \ z(\tau_0) \ \ x'(\tau_0) \ \ y'(\tau_0) \ \ z'(\tau_0)] \tag{2.140}$$

where the coordinates comprising the vector are measured in Frame S. Using the initial state, the equations of motion $\mathbf{x}'(\tau) = f(\tau, \mathbf{x}(\tau), \beta)$ are propagated to some later time $\tau_0 + T$ where the final state of the spacecraft is defined as $\mathbf{x}(\tau_0 + T)$. To obtain an initial state such that the final state arrives at a desired position $\mathbf{x}_d$, the update equations in Equations (2.138) or (2.139) are applied and iterated until the condition on the constraint vector $\mathbf{F}(\mathbf{X}) = \mathbf{0}$ is met. As an example, let the design vector be expressed as

$$\mathbf{X} = \begin{bmatrix} x'(\tau_0) \\ y'(\tau_0) \\ z'(\tau_0) \\ T \end{bmatrix} \tag{2.141}$$

where $x'(\tau_0), y'(\tau_0), z'(\tau_0)$ are the initial velocities of the spacecraft and T refers to the integration time. Likewise, the constraint vector $\mathbf{F}(\mathbf{X})$ is formulated such that

$$\mathbf{F}(\mathbf{X}) = \begin{bmatrix} x(\tau_0 + T) - x_d \\ y(\tau_0 + T) - y_d \\ z(\tau_0 + T) - z_d \end{bmatrix} \tag{2.142}$$

indicating that the only constraints are subjected to the spacecraft's final position. Consequently, the Jacobian matrix is computed using the partials of the constraint variables with respect to the initial states as

$$D\mathbf{F}(\mathbf{X}) = \begin{bmatrix} \frac{\partial x(\tau_0+T)}{\partial x'(\tau_0)} & \frac{\partial x(\tau_0+T)}{\partial y'(\tau_0)} & \frac{\partial x(\tau_0+T)}{\partial z'(\tau_0)} & \frac{\partial x(\tau_0+T)}{\partial T} \\ \frac{\partial y(\tau_0+T)}{\partial x'(\tau_0)} & \frac{\partial y(\tau_0+T)}{\partial y'(\tau_0)} & \frac{\partial y(\tau_0+T)}{\partial z'(\tau_0)} & \frac{\partial y(\tau_0+T)}{\partial T} \\ \frac{\partial z(\tau_0+T)}{\partial x'(\tau_0)} & \frac{\partial z(\tau_0+T)}{\partial y'(\tau_0)} & \frac{\partial z(\tau_0+T)}{\partial z'(\tau_0)} & \frac{\partial z(\tau_0+T)}{\partial T} \end{bmatrix} = \begin{bmatrix} \phi_{14} & \phi_{15} & \phi_{16} & x'(\tau_0+T) \\ \phi_{24} & \phi_{25} & \phi_{26} & y'(\tau_0+T) \\ \phi_{34} & \phi_{35} & \phi_{36} & z'(\tau_0+T) \end{bmatrix} \tag{2.143}$$

where the elements ϕ_{mn} are defined from Equation (2.121). Figure 2.10 depicts a single shooting technique for a case that allows only the initial velocities to vary in order to reach the desired state in position. Since this example employs the integration time T as a design variable, the algorithm uses a single shooter variable-time targeter to arrive at an initial state to satisfy $\mathbf{F}(\mathbf{X}) = \mathbf{0}$. As a result, the minimum norm solution of the update equation is employed since the number of constraints is less than the number of design variables ($m < n$). If a fixed-time targeter is used instead, the number of elements in the design vector $\mathbf{X}$ is identical to the constraint vector $\mathbf{F}(\mathbf{X})$, thus, an exact solution to the update equation exists. In this investigation, variable-time targeters are employed to compute periodic orbits in the CR3BP; fixed-time targeters are applied to rendezvous scenarios that are subject to a TOF constraint.
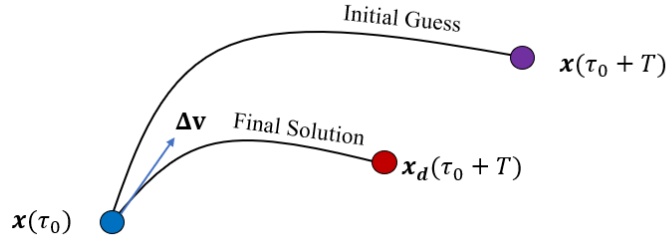

Fig. 2.10. Single Shooting Algorithm Diagram

Multiple Shooting Algorithms

When trajectory design problems incorporate nonlinear dynamics (i.e., paths passing near primaries) or lengthy integration times, a multiple-segment corrections scheme is better equipped to produce a solution. This multiple shooting technique is an extension to the single shooting method as it concurrently solves several two-point boundary value problems subject to sets of constraints. As an example, a trajectory is discretized into n patchpoints with $n - 1$ segments between them as depicted in

Figure 2.11. In this scenario, $\mathbf{x}_p^0$ for $p = 1, ..., n$ constitute each of the six-dimensional initial state vectors associated with the patchpoints as discretized from some trajectory. Likewise, in a general sense, $\mathbf{x}_p^f(T_p, E_p)$ for $p = 1, ..., n-1$ denote the final states at each of the patchpoints after some propagation time T_s and at the epoch time E_s. The epoch time is required for ephemeris models since they are time-dependent systems; however, the CR3BP does not require epochs since the equations of motion are autonomous.
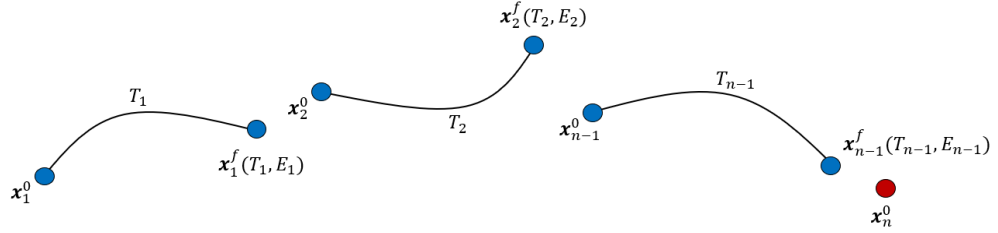

Fig. 2.11. Multiple Shooting Algorithm Diagram

In a multi-segment corrections scheme, the initial discretized segments along the trajectory are not continuous, thus, the constraint vector $\mathbf{F}(\mathbf{X})$ enforces state continuity conditions such that

$$\mathbf{x}_{p-1}^f(T_{p-1}, E_{p-1}) - \mathbf{x}_p^0 = \mathbf{0} \tag{2.144}$$

Equation (2.144) mandates that positions, velocities, and epoch times between patchpoints are continuous as depicted in Figure 2.12.
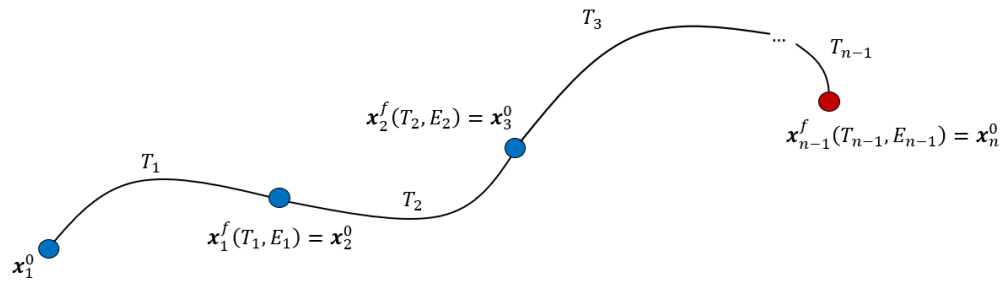
Fig. 2.12. Corrected Multiple Shooting Algorithm Diagram

Several different variations of the continuity constraints are implemented depending on the application. For example, for multiple impulsive thrust firings at patchpoints, velocities may vary as long as position continuiuty is met as illustrated in Figure 2.13. Ultimately, this information is reflected in the constraint vector $\mathbf{F}(\mathbf{X})$. Consider the design vector $\mathbf{X}$ for a multiple-shooting algorithm scheme to be defined

$$\mathbf{X} = \begin{bmatrix} \mathbf{x}_1^0 \\ \vdots \\ \mathbf{x}_n^0 \\ T_1 \\ \vdots \\ T_{n-1} \\ E_1 \\ \vdots \\ E_n \end{bmatrix} \tag{2.145}$$

where the elements in $\mathbf{X}$ denote the position and velocities for each patch point $\mathbf{x}_1^0, ..., \mathbf{x}_n^0$, the length of integration along each segment between patchpoints $T_1, ..., T_{n-1}$, and the epoch times at each patchpoint $E_1, ..., E_n$. To enforce position and velocity continuity between patchpoints, the constraint vector $\mathbf{F}(\mathbf{X})$ is formulated as

$$\mathbf{F}(\mathbf{X}) = \begin{bmatrix} \mathbf{x}_1^f(T_1, E_1) - \mathbf{x}_2^0 \\ \vdots \\ \mathbf{x}_{n-1}^f(T_{n-1}, E_{n-1}) - \mathbf{x}_n^0 \\ E_1 + T_1 - E_2 \\ \vdots \\ E_{n-1} + T_{n-1} - E_n \end{bmatrix} \tag{2.146}$$

Consequently, the Jacobian matrix $D\mathbf{F}(\mathbf{X})$ is evaluated as

$$DF(\mathbf{X}) = \begin{bmatrix} \frac{\partial \mathbf{x}_1^f}{\partial \mathbf{x}_1^0} & -\frac{\partial \mathbf{x}_2^0}{\partial \mathbf{x}_2^0} & & & \frac{\partial \mathbf{x}_1^f}{\partial T_1} & & & \frac{\partial \mathbf{x}_1^f}{\partial E_1} \\ & \ddots & \ddots & & & \ddots & & & \ddots \\ & & \frac{\partial \mathbf{x}_{n-1}^f}{\partial \mathbf{x}_{n-1}^0} & -\frac{\partial \mathbf{x}_n^0}{\partial \mathbf{x}_n^0} & & \frac{\partial \mathbf{x}_{n-1}^f}{\partial T_{n-1}} & & & \frac{\partial \mathbf{x}_{n-1}^f}{\partial E_{n-1}} \\ & & & & \frac{\partial T_1}{\partial T_1} & & & \frac{\partial E_1}{\partial E_1} & -\frac{\partial E_2}{\partial E_2} \\ & & & & & \ddots & & & \ddots & \ddots \\ & & & & & & \frac{\partial T_{n-1}}{\partial T_{n-1}} & & & \frac{\partial E_{n-1}}{\partial E_{n-1}} & -\frac{\partial E_n}{\partial E_n} \end{bmatrix}$$

(2.147)

Abbreviated notation and the computation of partials simplify the elements of the Jacobian matrix by arranging the matrix elements as

$$DF(\mathbf{X}) = \begin{bmatrix} \mathbf{\Phi}_1 & -\mathbf{I}_{6\times6} & & & \mathbf{x}_1'^f & & & \frac{\partial \mathbf{x}_1^f}{\partial E_1} \\ & \ddots & \ddots & & & \ddots & & & \ddots \\ & & \mathbf{\Phi}_{n-1} & -\mathbf{I}_{6\times6} & & \mathbf{x}_{n-1}'^f & & & \frac{\partial \mathbf{x}_{n-1}^f}{\partial E_{n-1}} \\ & & & & 1 & & & 1 & -1 \\ & & & & & \ddots & & & \ddots & \ddots \\ & & & & & & 1 & & & 1 & -1 \end{bmatrix}$$

(2.148)

where $\mathbf{\Phi}_s$ for $s = 1, ..., n-1$ denotes the state transition for each segment, $\mathbf{x}_s'^f$ for $s = 1, ..., n-1$ are the derivatives of the design variables with respect to T_s, and $\frac{\partial \mathbf{x}_s^f}{\partial E_s}$ for $s = 1, .., n-1$ pertain to the partial derivatives of the design variables with respect to epoch time E_s. In the CR3BP, epoch variables are not applicable and, thus, are omitted from the formulation of the design and constraint vectors. Moreover, the sample case incoprates variation in T_s during the iteration process, yet a fixed-time targeter eliminates the inclusion of time variables T_s in the formulation of the design variable vector.
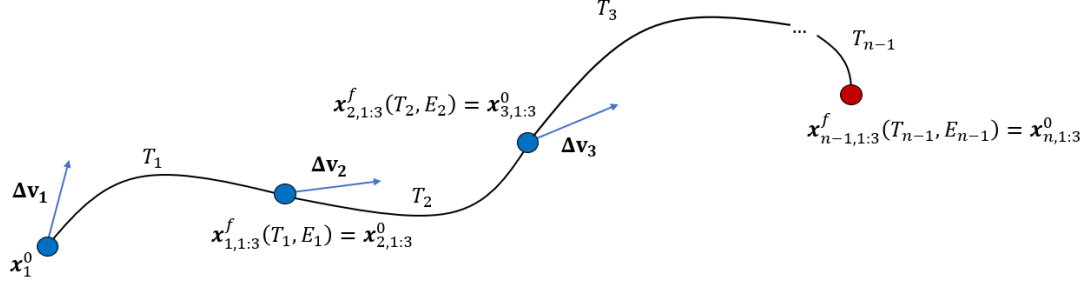
Fig. 2.13. Multiple Thrust Firing Schematic

Periodic Orbit Computation Strategies

In space missions, periodic orbits are particular useful for designers since they provide predictable and bounded behavior. In the CR3BP, periodic motion exists around the two primaries and close to the libration points. As it turns out, similar repeating behavior is also computed in a high-fidelity ephemeris model that is not exactly periodic but adequate enough for certain applications. In these cases, periodic orbits computed in the CR3BP are quasiperiodic in the higher fidelity ephemeris model since the dynamics are time-variant.

There are many types of periodic orbits that exist in the CR3BP. The most straightforward orbits to compute include those that are symmetric across the $\mathbf{x}_s - \mathbf{z}_s$ plane, which employ the mirror condition to target perpendicular crossings. Numerical corrections schemes are employed to obtain periodic solutions using an initial guess which can be drawn from a variety of different sources. For example, the linear variational equations of motion for the CR3BP is applied to approximate periodic motion in the vicinity of libration points. Moreover, two-body Keplerian motion provides reasonable approximations for periodic orbits close to each of the primaries. Additionally, previously converged periodic solutions provide initial guesses for orbits nearby and are used to construct continuation schemes to obtain similar orbits in a family. Consider an example to find symmetric orbits across the $\mathbf{x}_s - \mathbf{z}_s$ plane. An

initial state is selected such that $y_0 = 0$ and $x_0' = z_0' = 0$ to initialize a perpendicular crossing. Consequently, the initial state vector is defined as

$$\mathbf{x}_0 = [x_0 \ \ 0 \ \ z_0 \ \ 0 \ \ \dot{y}_0 \ \ 0]^T \tag{2.149}$$

The design vector $\mathbf{X}$ includes the free variables from the initial state which ultimately vary with iterations of the update equations. Thus,

$$\mathbf{X} = \begin{bmatrix} x_0 \\ z_0 \\ y_0' \\ T \end{bmatrix} \tag{2.150}$$

where the integration time T is included to implement a variable-time single shooter. Any omission of the initial state vector variables in the design variable vector forces those missing quantities to stay constant throughout the iteration process. The constraint vector $\mathbf{F}(\mathbf{X})$ contains those variables which are targeted to produce a perpendicular crossing on the $\mathbf{x}_s - \mathbf{z}_s$ plane. Thus, the variables selected to be zero in the initial state vector must also equate to zero at the crossing. The constraint vector is thus formulated as

$$\mathbf{F}(\mathbf{X}) = \begin{bmatrix} y(T) \\ x'(T) \\ z'(T) \end{bmatrix} = \mathbf{0} \tag{2.151}$$

It follows then that the Jacobian matrix $D\mathbf{F}(\mathbf{X})$ is defined as

$$D\mathbf{F}(\mathbf{X}) = \begin{bmatrix} \phi_{21} & \phi_{23} & \phi_{25} & y'(T) \\ \phi_{41} & \phi_{43} & \phi_{45} & x''(T) \\ \phi_{61} & \phi_{63} & \phi_{65} & z''(T) \end{bmatrix} \tag{2.152}$$

where ϕ_{ij} are the elements of the STM and the last column are the variable rates evaluated at final time T. Since the number of constraints is less than the number of

design variables, a minimum norm solution is employed to iterate on the initial guess until constraints are met within a numerical tolerance ($10e - 12$). The resulting solution will be a half revolution along a periodic orbit both originating and terminating along the $\mathbf{x}_s - \mathbf{z}_s$ plane. Once the half periodic solution is computed, the resulting state $\mathbf{X}^*$ can be integrated for $2T$ to yield the full periodic orbit. This same process can be modified to obtain planar periodic orbits by setting $z_0 = 0$ in the design variable vector and constraint vector. Thus,

$$
\mathbf{X} = \begin{bmatrix} x_0 \\ y_0' \\ T \end{bmatrix}
\tag{2.153}
$$

and the constraint vector follows as

$$
\mathbf{F}(\mathbf{X}) = \begin{bmatrix} y(T) \\ x'(T) \end{bmatrix} = \mathbf{0}
\tag{2.154}
$$

As a result, the Jacobian matrix is then expressed as

$$
D\mathbf{F}(\mathbf{X}) = \begin{bmatrix} \phi_{21} & \phi_{25} & y'(T) \\ \phi_{41} & \phi_{45} & x''(T) \end{bmatrix}
\tag{2.155}
$$

With an accurate initial guess, the correcter converges at a solution satisfing the perpendicular crossing constraint along the $\hat{\mathbf{x}}_s - \hat{\mathbf{z}}_s$ plane. Figure 2.14 demonstrates the progression from an initial state to a final half-periodic orbit employing the perpendicular crossing constraint.
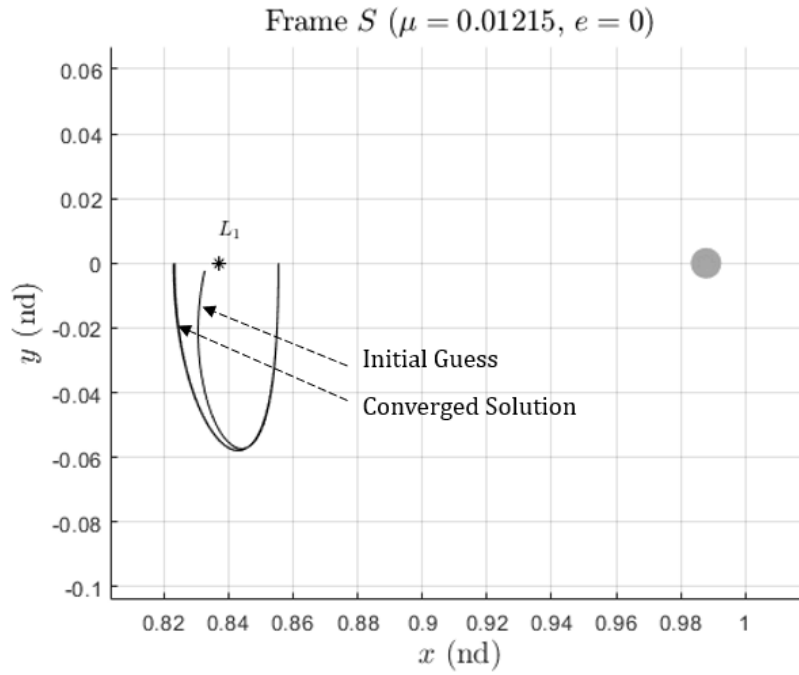
Fig. 2.14. Planar Periodic Orbit Computation

2.4.4 Periodic Family Continuation Techniques

Once a periodic orbit is computed, a continuation scheme is devised to obtain other periodic orbits in close proximity to the previously converged solution. A group of related periodic solutions is called a family and they deliver insight into the dynamical characteristics pertaining to a particular space. Families are also used in trajectory design since each family contains periodic orbits with similar characteristics. Assuming a converged solution exists, there are a number of ways to continue solutions to obtain other periodic orbits in the family.

Natural Parameter Continuation

The first method to continue a converged solution is natural parameter continuation (NPC). Once a solution satisfying a set of constraints is produced, one or more parameters of the final state is varied by a small amount and reconverged using the same numerical corrections process. The parameter with which the solution is perturbed can pertain to one of the state variables or other values like propagation time T or Jacobi constant J. In any case, the new perturbed state does not automatically meet the specified constraints and, thus, requires a corrections process to satisfy them within a set numerical tolerance. As an example, a methodology to implement NPC to continue a planar family of periodic orbits is outlined below.

1. First, assuming a solution exists, a converged state satisfying all constraints is obtained with the conditions

$$\mathbf{x}_{0,j}^* = \begin{bmatrix} x_{0,j} & 0 & 0 & 0 & y'_{0,j} & 0 \end{bmatrix}^T$$

where the quantity above refers to the corrected initial state which produces the periodic orbit with period P_j.

2. Next, the previously converged state is incremented by a small quantity ε so that the new state vector is expressed as

$$\mathbf{x}_{0,j+1} = \begin{bmatrix} x_{0,j} + \varepsilon & 0 & 0 & 0 & y'_{0,j} & 0 \end{bmatrix}^T$$

A typical value for ε in the Earth-Moon System is around 20-40 km if position is the incremented variable. The TOF for the new perturbed state is still P_j, but a variable-time shooter is employed to solve for the new period value.

3. The initial state $\mathbf{x}_{0,j+1}$ provides an initial guess for the differential corrections procedure which converges to $\mathbf{x}_{0,j+1}^*$ with period P_{j+1}, a periodic solution near $\mathbf{x}_{0,j}^*$. Note that $\mathbf{x}_{0,j+1}^* = \mathbf{x}_{0,j}^*$ if the x state is allowed to vary in the design vector formulation. By omitting this state variable in the corrections scheme, the targeter is forced to find a solution with $x_{0,j} + \varepsilon$ as the initial x state.

4. The process is repeated until the family is computed.

Although intuitive and relatively straightforward to implement, NPC fails when the geometry of the family is not known apriori. Moreover, difficulties emerge as the obtained solutions increase in sensitivity. An adaptive step size ε is used to mitigate the effects of sensitivities near regions of nonlinear dynamics, however, some intuition is required to implement it as part of a numerical corrections scheme. Nevertheless, NPC is useful for certain applications like continuing both periodic and non-periodic trajectories, however, alternative continuation schemes are used to supplement shortcomings in its process.

Pseudo-Arclength Continuation

An alternative continuation scheme called pseudo-arclength continuation (PAC) differs from NPC in the selection of the increment quantity used to advance to the next member of the orbit family. This increment, Δs, is in the direction tangent to the family. In this continuation scheme, all free variables are updated simultaneously and prior knowledge about the family evolution is not necessary. Although, PAC enables a larger step size to be taken from the previously converged solution and is in general more efficient at finding members of the same periodic family, the incremental variable Δs is not an intuitive physical parameter. As a result, less insight is provided into the relative differences between solutions. Consider a previously converged solution denoted by design variable vector $\mathbf{X}_j^*$, thus $\mathbf{F}(\mathbf{X}_j^*) = 0$. The initial guess for the next member of the family that may not yet meet the constraints is denoted as $\mathbf{X}_{j+1}^0$. The PAC scheme is outlined as follows:

1. Given $\mathbf{X}_j^*$, a unit vector is constructed from null vector $\Delta \mathbf{X}_j^*$ of the Jacobian matrix $D\mathbf{F}(\mathbf{X}_j^*)$. The null vector is selected since adding a multiple of null space vector to the first order update equation ($\mathbf{F}(\mathbf{X}) = \mathbf{F}(\mathbf{X}^0) + D\mathbf{F}(\mathbf{X}^0)(\mathbf{X} - \mathbf{X}^0)$) does not change its solution.

2. An additional constraint is added to $\mathbf{F}(\mathbf{X}_{j+1})$ to ensure that the next solution $\mathbf{X}_{j+1}$ is incremented by a small step Δs along direction tangent to family. This pseudo-arclength constraint is defined as

$$(\mathbf{X}_{j+1} - \mathbf{X}_j^*)^T \Delta \mathbf{X}_j^* - \Delta s = 0 \tag{2.156}$$

The new constraint vector is then expressed as

$$\mathbf{G}(\mathbf{X}_{j+1}) = \begin{bmatrix} \mathbf{F}(\mathbf{X}_{j+1}) \\ (\mathbf{X}_{j+1} - \mathbf{X}_j^*)^T \Delta \mathbf{X}_j^* - \Delta s \end{bmatrix} = 0 \tag{2.157}$$

The derivative of the updated constraint vector, $\mathbf{G}(\mathbf{X}_{j+1})$, with respect to the design variable vector $\mathbf{X}_{j+1}$ produces an updated Jacobian matrix $D\mathbf{G}(\mathbf{X}_{j+1})$ defined as

$$D\mathbf{G}(\mathbf{X}_{j+1}) = \frac{\partial \mathbf{G}(\mathbf{X}_{j+1})}{\partial \mathbf{X}_{j+1}} = \begin{bmatrix} D\mathbf{F}(\mathbf{X}_{j+1}) \\ \Delta \mathbf{X}_j^{*T} \end{bmatrix} \tag{2.158}$$

3. The new constraint vector $\mathbf{G}(\mathbf{X}_{j+1})$ and Jacobian matrix $D\mathbf{G}(\mathbf{X}_{j+1})$ are iterated to yield a converged solution $\mathbf{X}_{j+1}^*$ which represents the next member in the orbit family.

Both NPC and PAC can be utilized in a continuation scheme to obtain a variety of orbit families in the CR3BP. In this investigation, a natural parameter continuation is utilized to obtain the first member of an orbit family and PAC is employed to compute the remaining orbits in the family.

2.4.5 Periodic Orbit Families

In this investigation, a number of periodic orbit families are computed and continued in the CR3BP. Single-shooter differential correction schemes are used to target either perpendicular crossings or periodicity. Once a member in a family is converged, pseudo-arclength continuation is employed to produce the family of periodic orbits.

All the orbits formulated in the CR3BP considered in this investigation are symmetrical across $\hat{\mathbf{x}}_s - \hat{\mathbf{z}}_s$ plane. Each periodic orbit family is introduced and plotted in two different views, (i) to represent each member of of the family and (ii) to parameterize the members of the family by Jacobi constant value.

Lyapunov Families

The Lyapunov orbits are two-dimensional families that originate from each of the collinear libration points: L_1, L_2, and L_3. At first, the first-order linear variational equations for the CR3BP are used to approximate periodic motion around the libration points and a single-shooter corrections scheme is employed to produce trajectories with perpendicular crossings. The L_1 Lyapunov family is plotted in Figure 2.15. The left plot in Figure 2.15 illustrates each member in the L_1 Lyapunov family and the right plot identifies each of the orbits' associated Jacobi constant value. An assessment of the linear stability of each of the orbit members indicates that that there are two bifurcations that exist in L_1 Lyapunov family, (i) one to the L_1 Halo family and (ii) one to the L_1 Axial family.
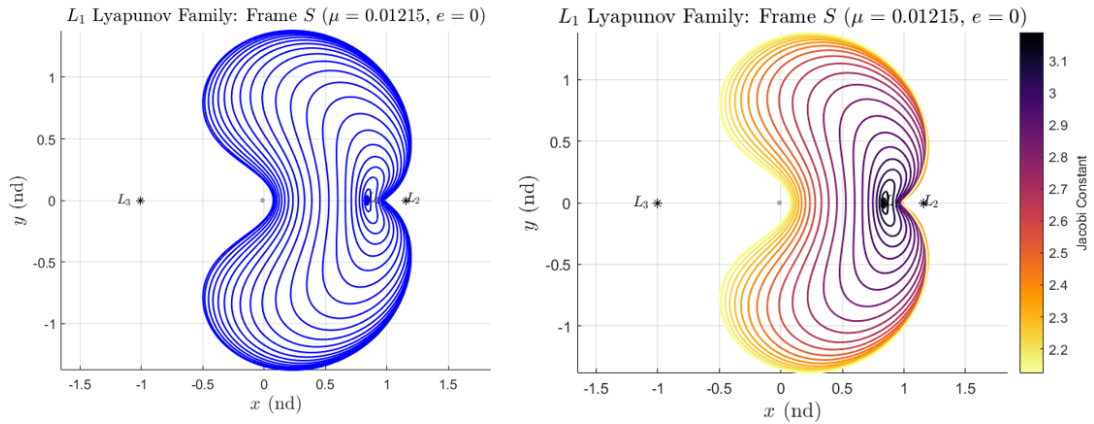
Fig. 2.15. L_1 Lyapunovs in Earth-Moon System

An identical procedure is employed to compute the L_2 Lyapunov and the L_3 Lyapunov families as plotted in Figure 2.16 and 2.17, respectively. Similar to the L_1 Lyapunovs, the L_2 Lyapunovs bifurcate to the L_2 Halos and L_2 Axials whereas the L_3 Lyapunovs bifurcate to the L_3 Halos and L_3 Axials, respectively.
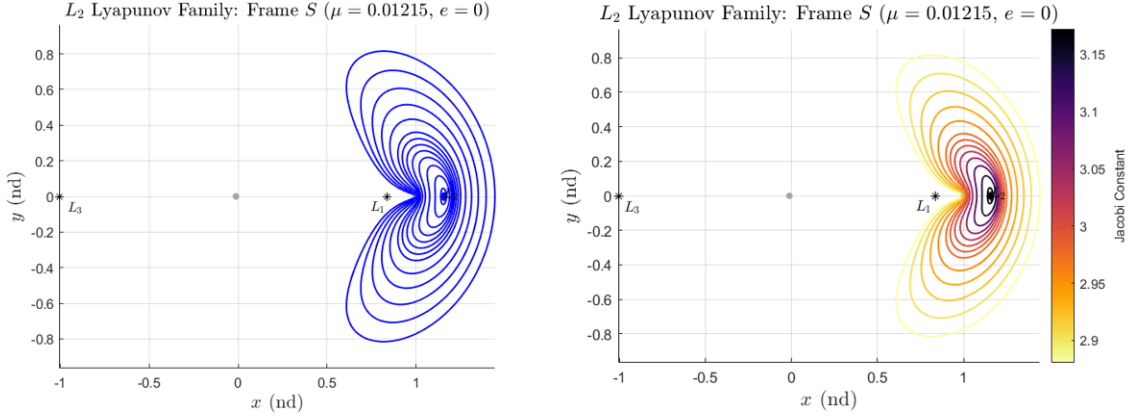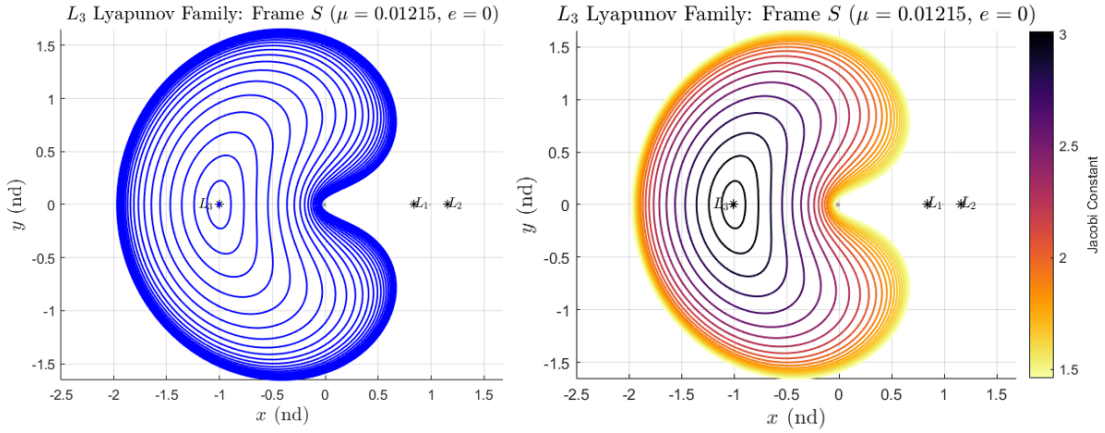

Fig. 2.16. L_2 Lyapunovs in Earth-Moon System

Fig. 2.17. L_3 Lyapunovs in Earth-Moon System

Halo Families

The Halo families are three-dimensional periodic orbits that also originate from the collinear libration points. Consider the L_1 Halo family as plotted in Figure 2.18. The orbits are symmetrical across the $\hat{\mathbf{x}}_s - \hat{\mathbf{z}}_s$ plane and originate from an L_1 Lyapunov. To compute the initial members of the L_1 Halo family, a natural parameter continuation scheme is applied to a L_1 Lyapunov orbit that undergoes a stability change (as indicated by the monodromy matrix for that particular orbit) by subsequently perturbing the state in either the $+z$ or $-z$ direction. The new perturbed state is then corrected to yield a perpendicular crossing along the $\hat{\mathbf{x}}_s - \hat{\mathbf{z}}_s$ plane. A pseudo-arclength continuation scheme is implemented to compute the remaining members of the orbit family. The orbits that possess apolune points above the plane of the primaries comprise the L_1 Northern Halo Family whereas those orbits that have apolune points below are part of the L_1 Southern Halo Family as presented in the top and bottom parts of Figure 2.18, respectively. A similar procedure is employed to obtain the L_2 Halo Families and the L_3 Halo Families, along with their corresponding Northern and Southern divisions, in Figures 2.19 and 2.21, respectively.

Consider the L_2 Southern Halo Family. Let the stability index for each orbit be defined as

$$\zeta_i = \frac{\text{Re}(\ln \lambda_i)}{P} \tag{2.159}$$

where the real part of the natural log of each eigenvalue λ_i is divided by the period of the corresponding orbit P. According to Boudad et al. [29], there are multiple ways to define the stability index, however, Equation (2.159) detects stability changes across a family of solutions and is not biased by orbital period. Moreover, the stability bound is equal to zero, therefore if *all* six eigenvalues are equal to zero then the corresponding orbit is stable in a linear sense. On the contrary, if at least *one* of the eigenvalues is non-zero, the orbit is unstable. A plot of the stability index value over perilune radius for each orbit is given in Figure 2.20. According to Zimovan et

al. [8], a subset of special orbits within the L_2 Southern Halo Family form the L_2 Near Rectilinear Halo Orbits (NRHOs) defined as the halo orbits between the first and third stability changes in the region of the smaller primary, as indicated in the left plot of Figure 2.20. These NRHOs are characterized by their extremely elongated shape and close proximity to the Moon. Moreover, they possess desirable stability properties and useful eclipse avoidance geometries in the Sun-Earth-Moon system. In fact, the baseline orbit for Gateway, NASA's proposed lunar outpost, is a specific type of NRHO denoted as the 9:2 L_2 Lunar Synodic Resonant NRHO. As the name suggests, the 9:2 NRHO is resonant with the Lunar period completing nine orbits for every two Lunar synodic revolutions around the Earth.
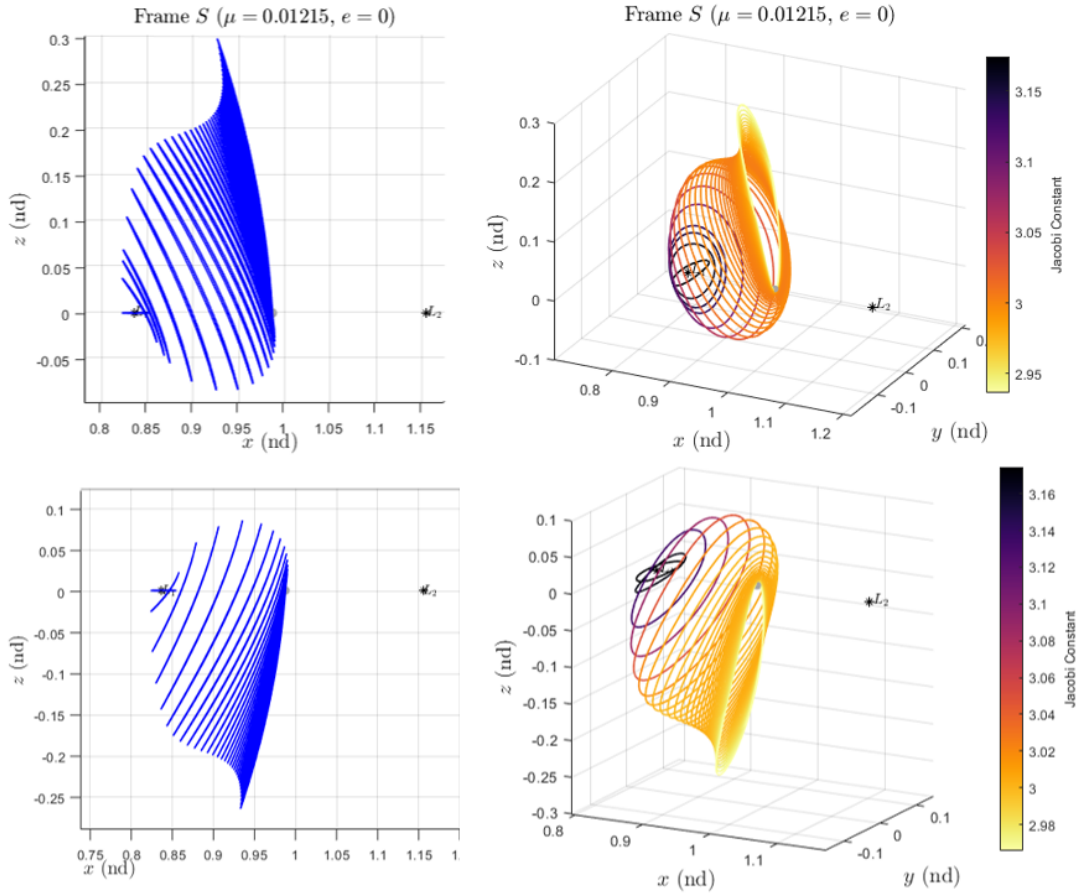
Fig. 2.18. L_1 Northern (top) and Southern (bottom) Halo Families in Earth-Moon System
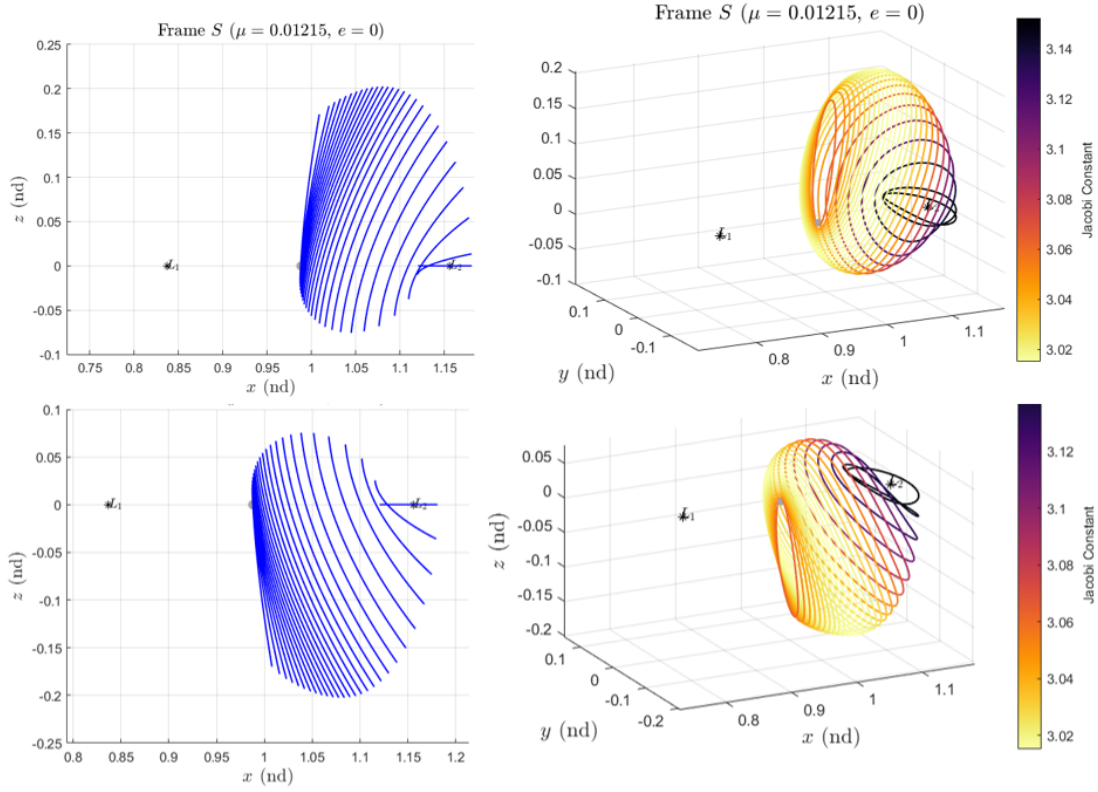
Fig. 2.19. L_2 Northern (top) and Southern (bottom) Halo Families in Earth-Moon System
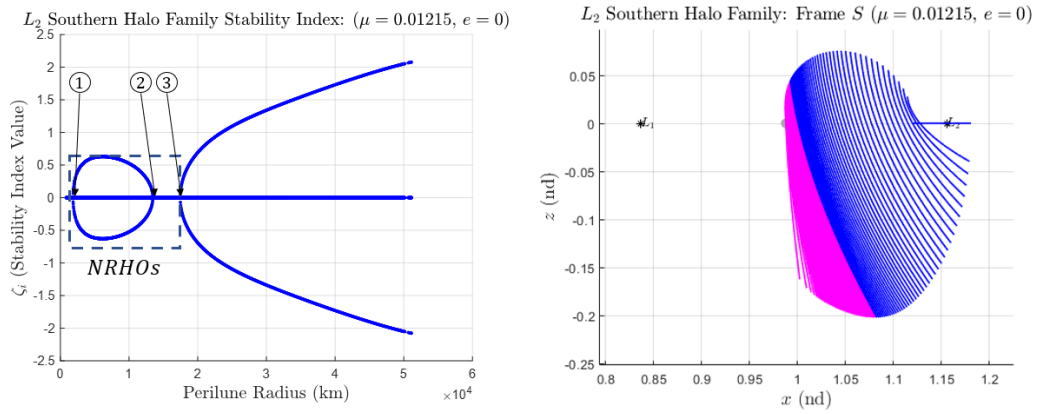
Fig. 2.20. Stability index plot for Earth-Moon L_2 Southern Halos (left) and identification of NRHOs in purple (right)
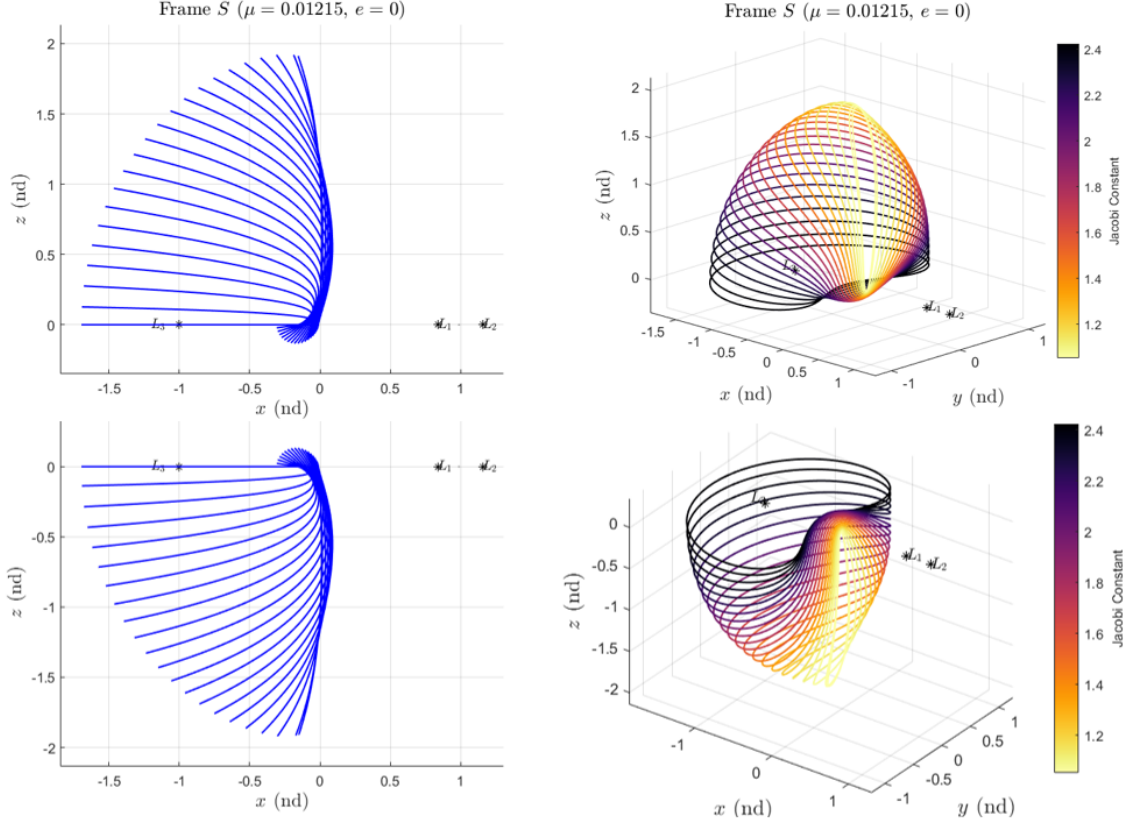
Fig. 2.21. L_3 Northern (top) and Southern (bottom) Halo Families in Earth-Moon System

Axial Families

The Axial Families are also another set of three-dimensional periodic orbits that exists in the CR3BP. They originate from the collinear libration points and are initially computed by targeting a perpendicular crossing along the $\hat{\mathbf{x}}_s - \hat{\mathbf{z}}_s$ plane. To compute the first members of the L_1 Axial Family, a L_1 Lyapunov orbit selected as the bifurcation orbit from the Halo to the Axial Family is slightly perturbed in the $\dot{z}$ direction. The perturbed state is targeted to obtain a perpendicular crossing and the converged result is applied to a pseudo-arclength continuation scheme to generate the other members of the family as plotted in Figure 2.22. A similar procedure is

employed to compute the L_2 and L_3 Axial Families as shown in Figures 2.23 and 2.24, respectively.
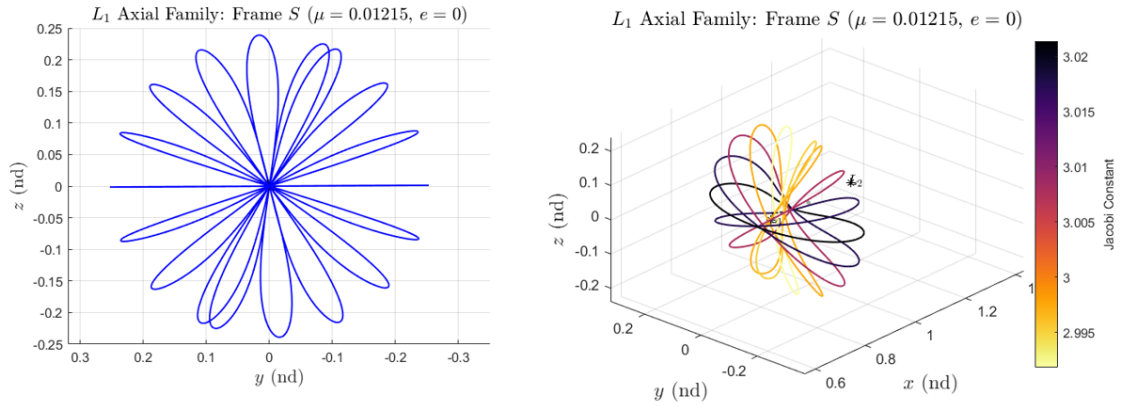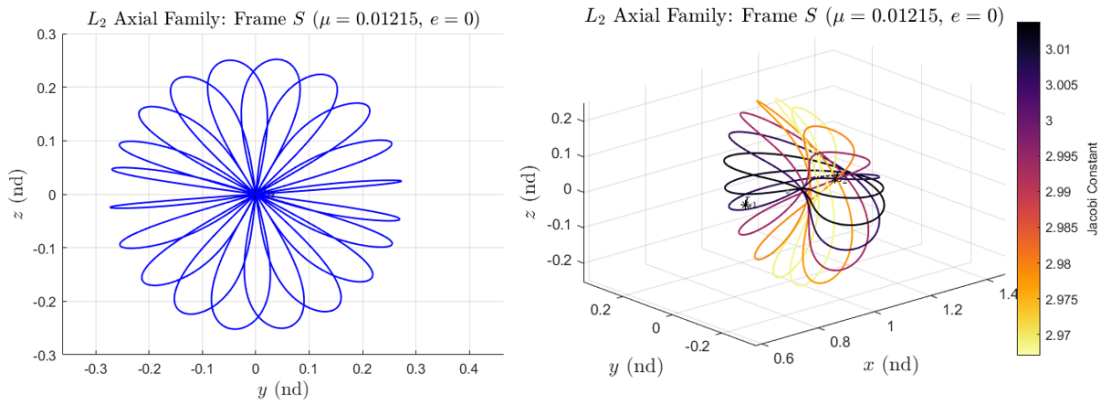

Fig. 2.22. L_1 Axials in Earth-Moon System

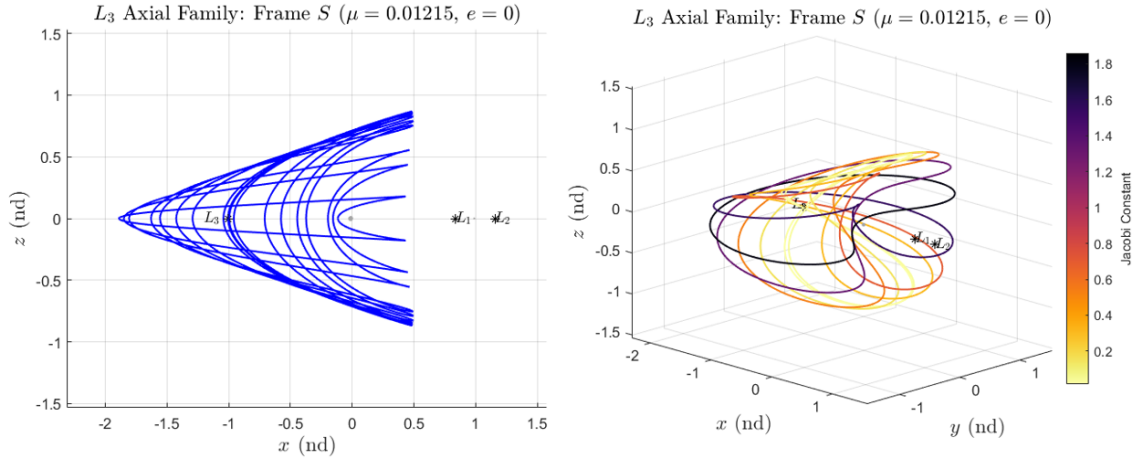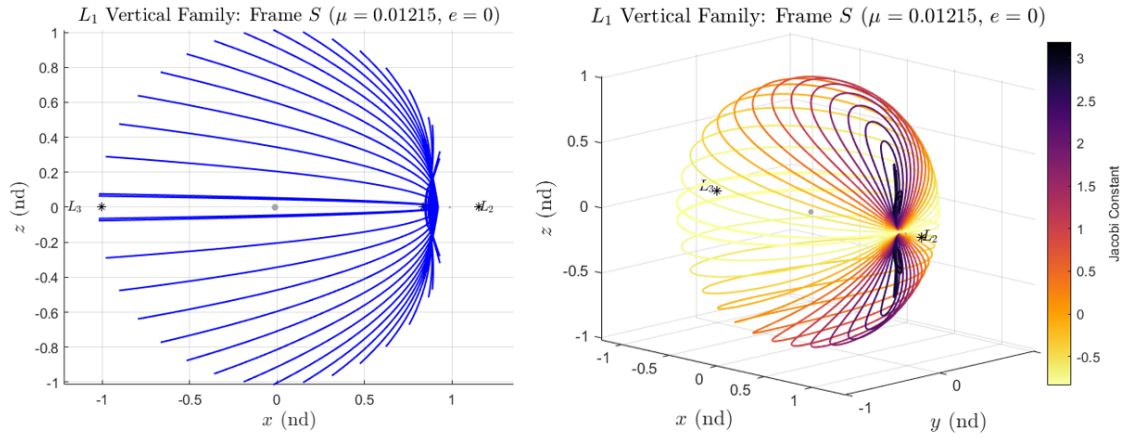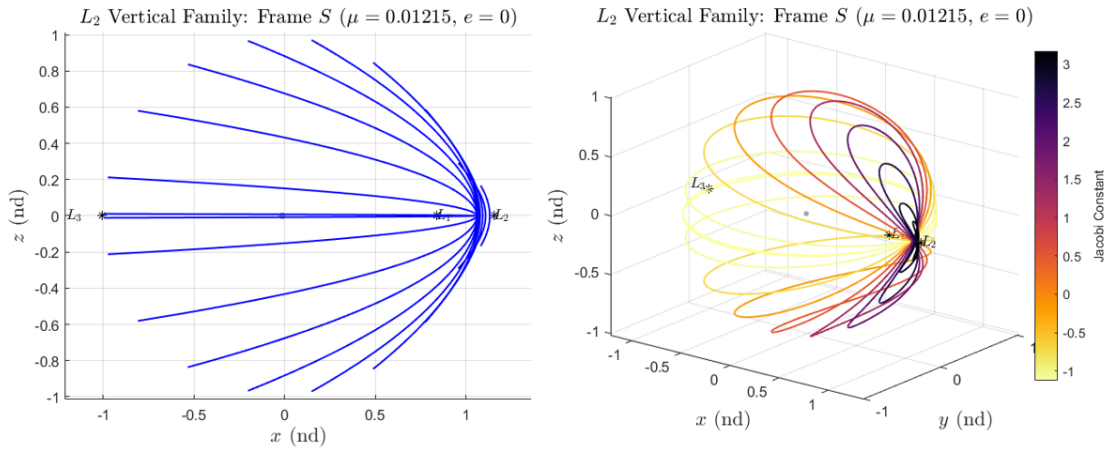Fig. 2.23. L_2 Axials in Earth-Moon System

Fig. 2.24. L_3 Axials in Earth-Moon System

Vertical Families

The Vertical Families are three-dimensional periodic orbits characterized by a substantial out-of-plane component of the motion in the CR3BP. The first member of the L_1 Vertical Family is initially computed by slightly perturbing the bifurcating orbit from the L_1 Axial to the L_1 Vertical Family in the $\dot{z}$ direction. The perturbed state is corrected for a perpindicular crossing at the $\hat{\mathbf{x}}_s - \hat{\mathbf{z}}_s$ plane and continued using a pseudo-arclength continuation scheme as plotted in Figure 2.25. A similar procedure is used to compute the L_2 and L_3 Vertical Families, as plotted in Figures 2.26 and 2.27, respectively.

Fig. 2.25. L_1 Verticals in Earth-Moon System
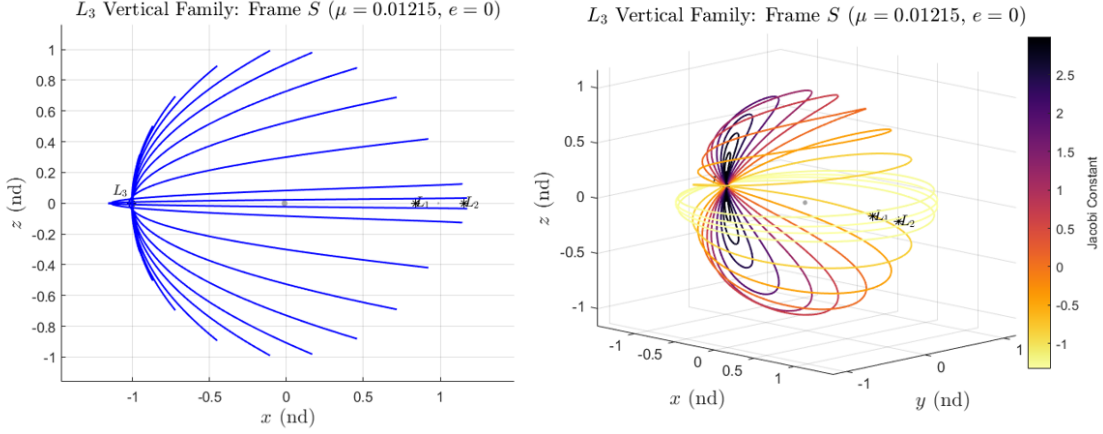

Fig. 2.26. L_2 Verticals in Earth-Moon System

Fig. 2.27. L_3 Verticals in Earth-Moon System

DRO Family

The Distant Retrograde Orbit (DRO) Family are a set of planar periodic orbits that originate from the smaller primary. In this investigation, two-body approximations for periodic motion around the Moon are utilized as initial guesses to target perpendicular crossings along the $\hat{\mathbf{x}}_s - \hat{\mathbf{z}}_s$ plane. The orbits are then continued using a pseudo-arclength continuation method to obtain the remaining members of the family as plotted in Figure 2.28. From an initial glance, it appears that Jacobi constant decreases (and subsequently orbital period increases) as the perilune radius grows for each member of the family. The DROs possess favorable stability properties and a DRO with a periline of 72,000 km is selected to be one of the baseline orbits for NASA's proposed Artemis Missions.
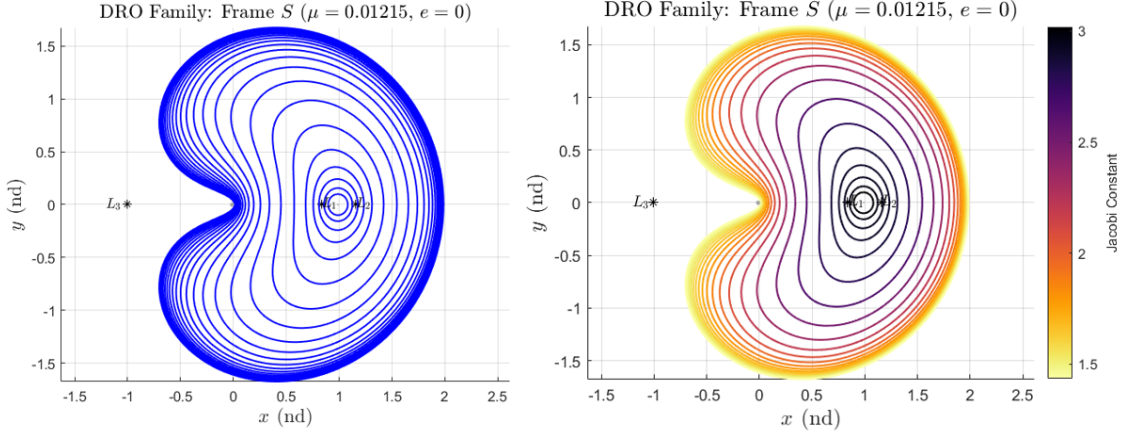
Fig. 2.28. DROs in Earth-Moon System

Northern L_2 Butterfly Family

The L_2 Butterfly Family is another example of a periodic orbit family that exists in the CR3BP. These orbits are characterized by their unique wrapping shape around the second primary. Similar to the NRHOs in the Earth-Moon system, the Butterfly Family exhibit nearly-stable behavior and approach close to the lunar surface. They are examined as potential orbits to provide low lunar orbit and surface access in Davis et al. [30]. The Butterfly Family bifurcates off a L_2 NRHO with a perilune radius of approximately 1830 km. Since the type of bifurcation is classified as period doubling, their periods are almost double that of the L_2 NRHO where most of the time is spent in the L_2 lobe instead of the L_1 lobe.
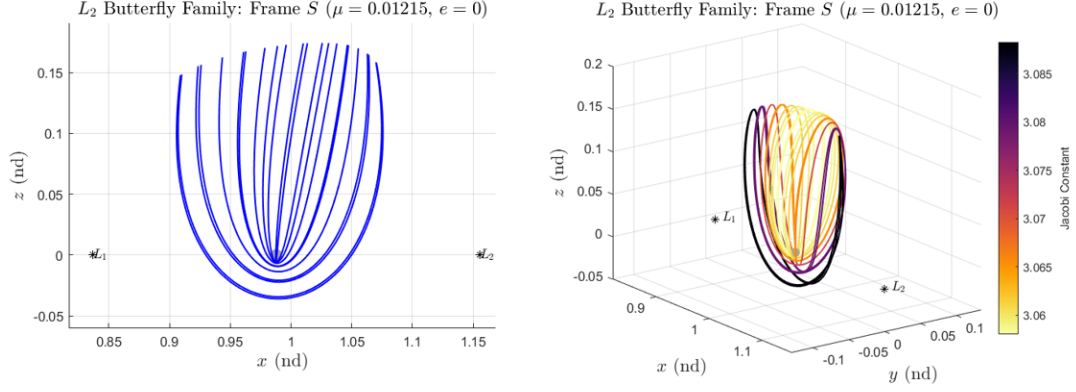
Fig. 2.29. Northern L_2 Butterfly Family in Earth-Moon System

2.5   Selection of Reference Orbits

In this investigation, three periodic orbits in the CR3BP for the Earth-Moon system are selected as reference trajectories for analysis in the relative motion problem. The first reference orbit is the 9:2 L_2 NRHO. The 9:2 NRHO is lunar synodic resonant such that for every two lunar synodic revolutions around the system barycenter, the orbit correspondingly undergoes nine revolutions. The NRHO is very nearly stable in a linear sense and thus it is identified as favorable for stationkeeping applications. The period of the 9:2 NRHO is approximately 6.5 days with a perilune distance of about 3,250 km and an apolune radius of 71,000 km. Moreover, the orbit is selected as the baseline trajectory for the Gateway platform. Figure 2.30 plots the L_2 Southern Halo Family and identifies the 9:2 NRHO within the family. The second reference orbit is a small DRO with a close proximity to the Moon. The small DRO is intended to represent orbits that possess a larger gravitational influence from the Moon and thus appear more Keplerian in geometry. The corresponding small DRO considered in this investigation has a period of about 21.5 hours with a perilune radius of about 8,860 km and an apolune distance of approximately 9,725 km. Figure 2.31 plots the DRO

family in the Earth-Moon system and identifies the small DRO within the members of the family. The third and final reference orbit incorporated in this investigation is a large DRO with a period of about 14.2 days. The perilune distance for the large DRO is about 71,690 km and the apolune radius is approximately 98,480 km. The large DRO is intended to be flown during the Artemis I mission. Figure 2.32 plots the DRO family and identifies the large DRO. The orbits used in this investigation are selected to simulate possible flight trajectories for NASA's Artemis and Gateway missions.
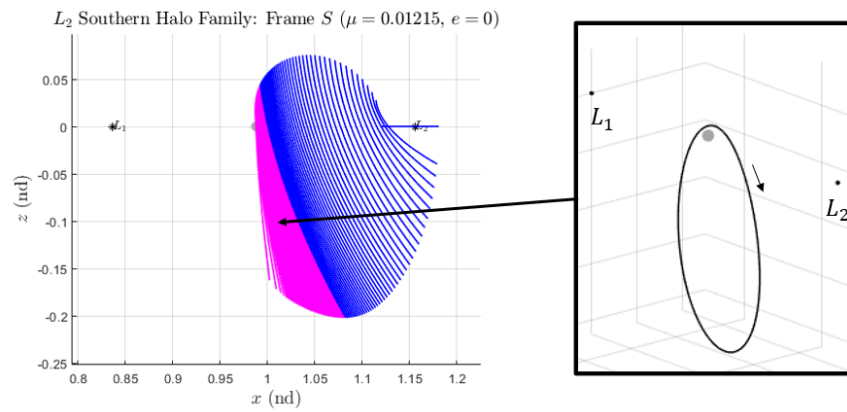

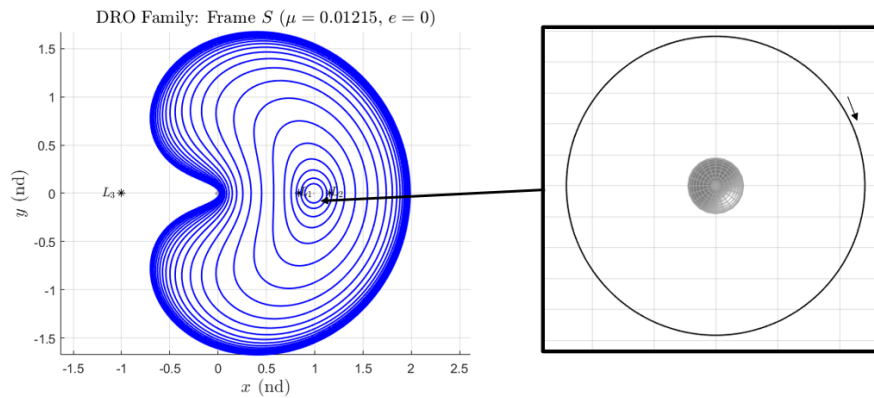Fig. 2.30. L_2 Southern Halo Family with NRHOs in purple (left) and 9:2 NRHO (right)

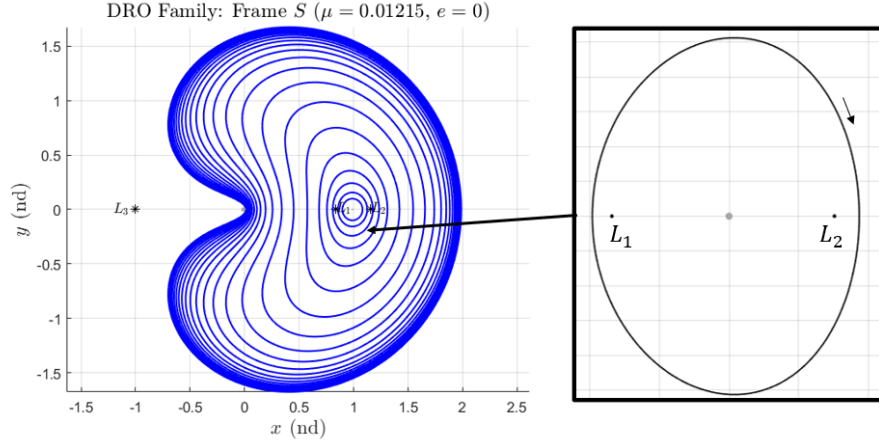Fig. 2.31. DRO Family (left) and a small DRO (right)

Fig. 2.32. DRO Family (left) and a large DRO (right)

2.5.1 Transitioning Solutions from CR3BP to ER3BP

The reference orbits used in this investigation are selected from the CR3BP. In mission design applications, it is beneficial to start with solutions from a simpler model and transition the solutions to more complicated dynamical systems. The employment of the ER3BP accounts for the Moon's nonzero eccentricity and therefore stipulates a changing distance between the two primaries over time. As a result, reference trajectories obtained in the CR3BP are inadequate for implementation in the ER3BP and, thus, require a corrections scheme to transition the solutions. A multiple shooting algorithm is utilized to correct for continuity in both position and velocity using a stacked revolutions approach. The steps for transitioning between solutions in the CR3BP and ER3BP are outlined as follows:

1. A periodic orbit is identified in the CR3BP and discretized into a series of n patchpoints with $n-1$ segments between them. The patchpoints are then reproduced for a number of orbital periods in a method called stacking revolutions. For the 9:2 NRHO and the small DRO, one patchpoint per revolution for 9 orbital periods is found to be an effective approach. For orbits with larger

periods, including the large DRO, multiple patchpoints are selected along one revolution to preserve the orbit geometry.

2. The patchpoints are transitioned into the ER3BP and propagated for approximately the same time between them in the CR3BP. In the initial transition, the patchpoints and their corresponding segments are discontinuous in the ER3BP since the Earth-Moon distance changes at every time step. A multiple shooting scheme is devised to correct for position and velocity continuity between the end of each segment and the following patchpoint.

3. A differential corrections scheme is implemented to update the positions and velocities of each of the patchpoints until state continuity is achieved within a set numerical tolerance.

In this investigation, the three reference orbits selected in the CR3BP, namely the 9:2 NRHO, the small DRO, and the large DRO, are transitioned into the ER3BP. Figure 2.33 plots the 9:2 NRHO in the CR3BP along with nine revolutions of its ER3BP equivalent based on the results of the employed multiple shooting algorithm. Unlike the CR3BP periodic orbit, the trajectory obtained in the ER3BP is not periodic. Nevertheless, the orbit geometry is preserved in the transition given by 9:2 NRHO's elongated shape and and perilune and apolune locations. Since the converged orbit in the ER3BP is not periodic, its constantly varying period is given by the time between perilunes for each revolution. The plot of the NRHO in the ER3BP also includes the range of locations for the L_1 and L_2 libration points which oscillate with the changing distance between the Earth and the Moon. Likewise, a similar procedure is employed for the small DRO in the CR3BP and its ER3BP result as plotted in Figure 2.34. Once again, the ER3BP orbit is not periodic, however, the resulting solution retains the geometry of the initial CR3BP reference solution. Finally, the large DRO is transitioned into the ER3BP and plotted in Figure 2.35. Due to the longer period of the large DRO, multiple patchpoints are discretized along a single revolution to ensure that the shape of the DRO is preserved in the transition process. Although it

is important to note that ER3BP resulting solutions are not identical to their CR3BP counterparts, the motion obtained still captures the dynamical characteristics of each of the selected reference orbits and provides a good baseline trajectory for the relative motion analysis in this investigation.
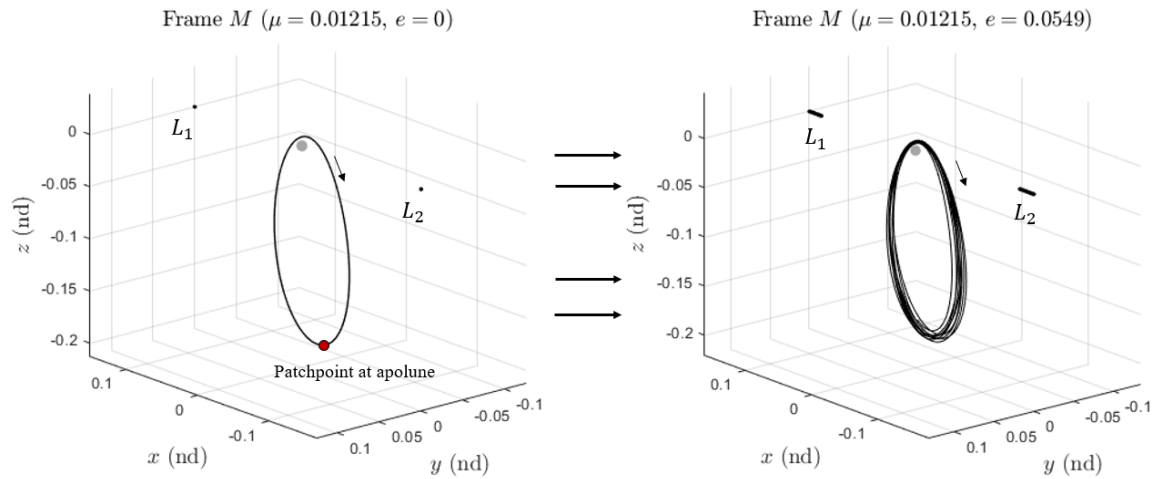

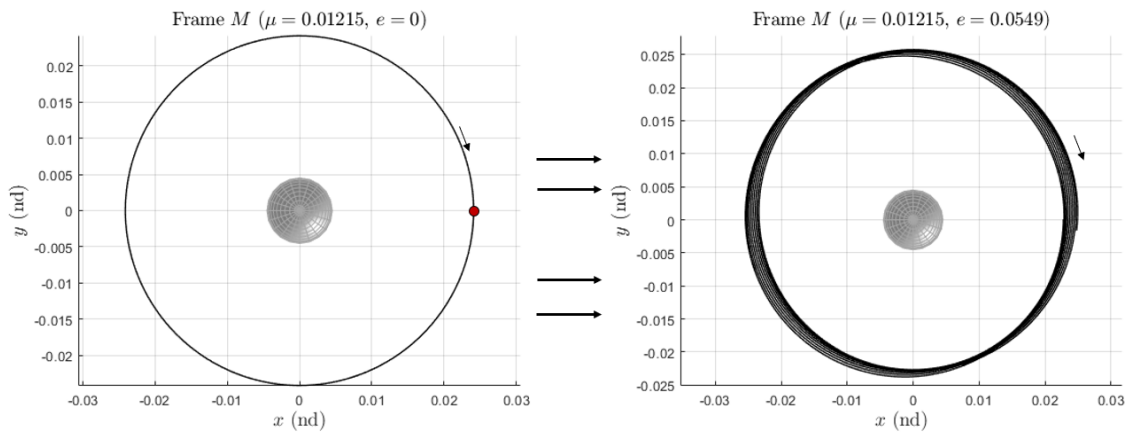Fig. 2.33. 9:2 NRHO in the CR3BP with the selected patchpoint (left) and its ER3BP equivalent (right)

Fig. 2.34. The small DRO in the CR3BP with the selected patchpoint (left) and its ER3BP equivalent (right)
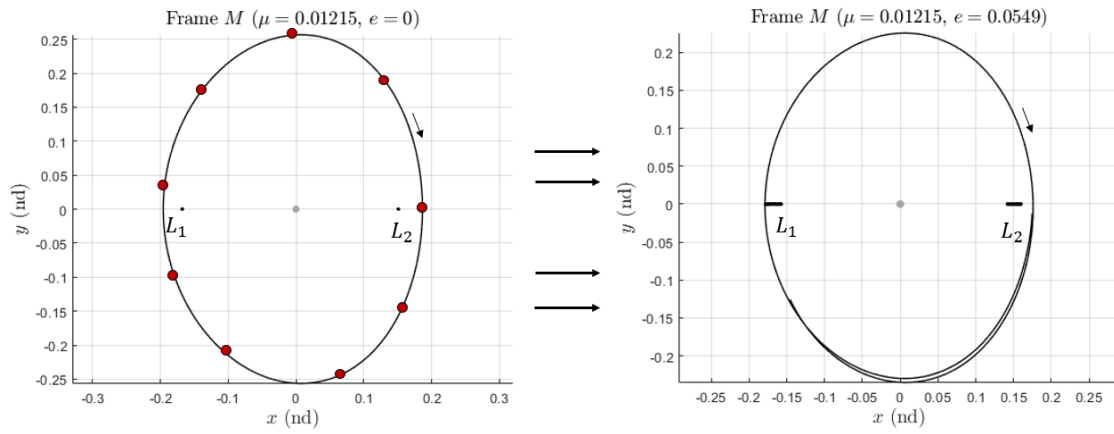
Fig. 2.35. The large DRO in the CR3BP with the selected patchpoints (left) and its ER3BP equivalent (right)

3. RELATIVE MOTION MODELS

The first step involved with relative motion analysis in any dynamical system is the formulation of a relative motion model involving the motion of two or more spacecraft. Usually, two spacecraft denoted as a target (or chief) and chaser (or deputy) are identified to formulate the relative equations of motion. These models must provide an accurate prediction of the chaser's relative state from the perspective of the target over time. Conventionally, relative motion models are expressed using a rotating frame attached to a target spacecraft. This local frame is denoted as the Local-Vertical-Local-Horizontal (LVLH) frame. One of the earliest relative motion models to employ an LVLH frame are the Hill-Clohessy-Wiltshire (HCW) equations developed in the 20th century [2]. These equations assume that the target orbit is circular and the chaser's orbit is near circular given that the initial relative position between the spacecraft is small. The HCW model is based on two-body dynamics and has proven to be effective for rendezvous in Low Earth Orbit. Extensions to the HCW model have accounted for target orbits of arbitrary eccentricity including the Yamanaka-Ankersen STM [3]. Moreover, other proposed models have incorporated J_2 and atmospheric drag perturbations including the formuation presented in Kechichian [31]. Xu and Wang [32] incorporate lunar perturbations in their relative motion model for near Earth orbits. A comprehensive survey of available relative motion models with a description of perturbations incorporated in each set of equations is provided by Sullivan et al. [12]. Though some of the proposed relative models offer closed-form descriptions of the relative dynamics, a vast majority of them are formulated with the two-body assumption. The inclusion of other forces in these models is usually accomplished with special and general perturbation techniques and only a specific set of perturbations are considered. Nevertheless, there is limited work on the formulation of relative models developed in the restricted three-body problem.

Casotto [33] initially proposed a general set of equations to model relative dynamics subject to arbitrary perturbations, however, his analysis still retains a Keplerian description of the motion as an initial assumption. To that end, his work outlines a method to solve for the time history of the LVLH frame's motion under a general set of perturbations by exploiting only kinematic relationships between the local frame and the inertial frame. Franzini et al. [1] adopted Casotto's technique to formulate the nonlinear equations of relative motion from both the two-body and the restricted three-body problems. Their analysis provides a general set of equations to obtain an exact description of the relative dynamics under arbitrary orbital perturbations. This investigation employs the formulation presented in Franzini et al. [1] and extends the validation of the equations of motion for other target orbits of interest.

3.1 LVLH Frame Definition

The formulation of the equations of relative motion begin with a description of the LVLH frame L. There are a variety of ways to define the local frame, yet the definition used in this investigation is portrayed in Figure 3.1. Consider the following formulation comprised of vectors denoting the target state about the central body.

$$\hat{\mathbf{i}} = \hat{\mathbf{j}} \times \hat{\mathbf{k}} \tag{3.1}$$

$$\hat{\mathbf{j}} = -\frac{\mathbf{h}}{h} \tag{3.2}$$

$$\hat{\mathbf{k}} = -\frac{\mathbf{r}}{r} \tag{3.3}$$

In this LVLH frame definition, $\mathbf{r}$ denotes the target position vector from the central body, and $\mathbf{h}$ is the target specific angular momentum vector computed as $\mathbf{h} = \mathbf{r} \times \mathbf{v}$, where $\mathbf{v}$ is the target velocity relative to the central body. The directions defined in Equations (3.1)-(3.3) are sometimes referred to as V-BAR, H-BAR, and R-BAR, respectively.
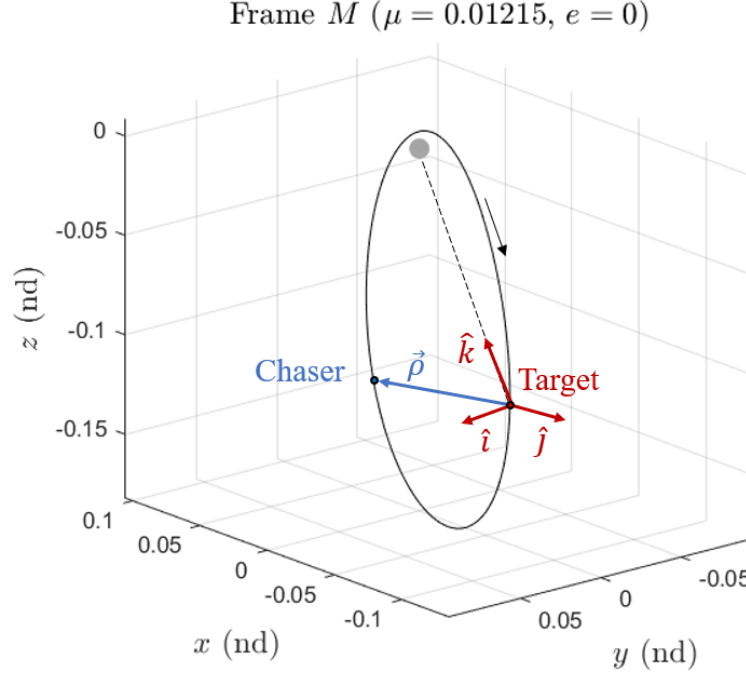
Frame M ($\mu = 0.01215$, $e = 0$)

Fig. 3.1. The LVLH frame attached to a target spacecraft with its associated directions

3.2 Keplerian-Based Relative Motion

Assume the target, a passive spacecraft, and the chaser, a maneuverable spacecraft, orbit about a central body. The equations governing the motion of both spacecraft follow as

$$[\ddot{\mathbf{r}}]_I = \frac{d^2\mathbf{r}}{dt^2} = -\frac{\mu}{r^3}\mathbf{r} + \boldsymbol{\eta}_t \tag{3.4}$$

$$[\ddot{\mathbf{r}}_c]_I = \frac{d^2\mathbf{r}_c}{dt^2} = -\frac{\mu}{r_c^3}\mathbf{r}_c + \boldsymbol{\eta}_c + \mathbf{u} \tag{3.5}$$

where the brackets $[\ddot{\mathbf{r}}]_I$ or $d^2\mathbf{r}/dt^2$ denote the acceleration of the corresponding position vector observed in the inertial frame I. The vector $\mathbf{r}$ corresponds to the position vector from the central body to the target and $\mathbf{r}_c$ denotes the position from the central body to the chaser, respectively. Moreover, μ is the central body's gravitational parameter.

The quantities summed to the right of the acceleration terms in Equations (3.4) and (3.5) are defined such that

- $\boldsymbol{\eta}_i = \eta_{i,x}\hat{\mathbf{i}} + \eta_{i,y}\hat{\mathbf{j}} + \eta_{i,z}\hat{\mathbf{k}}$ denote the components of other orbital perturbations in the LVLH frame for the target as $\boldsymbol{\eta}_t$ and the chaser as $\boldsymbol{\eta}_c$, respectively.

- $\mathbf{u} = u_x\hat{\mathbf{i}} + u_y\hat{\mathbf{j}} + u_z\hat{\mathbf{k}}$ expresses the chaser's control vector.

It is advantageous to formulate the equations of motion in the LVLH frame L so that the relative dynamics can be characterized from the perspective of the target. To that end, analytical descriptions for the angular velocity and acceleration vectors of L with respect to the inertial frame are derived, as presented in Casotto [33] and Franzini [1].

Exploiting purely kinematic relationships, an analytical description of the LVLH frame L angular velocity with respect to the inertial frame I is obtained. It is assumed that all quantities represented by $\frac{d\mathbf{r}}{dt}$ are inertially-based derivatives, whereas quantites denoted as $\dot{\mathbf{r}}$ are derivatives taken in the local frame L. The derivatives of the LVLH frame unit vectors are taken as

$$\frac{d\hat{\mathbf{i}}}{dt} = \boldsymbol{\omega}_{I/L} \times \hat{\mathbf{i}} \tag{3.6}$$

$$\frac{d\hat{\mathbf{j}}}{dt} = \boldsymbol{\omega}_{I/L} \times \hat{\mathbf{j}} \tag{3.7}$$

$$\frac{d\hat{\mathbf{k}}}{dt} = \boldsymbol{\omega}_{I/L} \times \hat{\mathbf{k}} \tag{3.8}$$

where $\boldsymbol{\omega}_{I/L}$ denotes the angular velocity vector of the LVLH frame L with respect to the inertial frame I. The following cross products between each of the unit vectors and their corresponding time derivatives yield

$$\hat{\mathbf{i}} \times \frac{d\hat{\mathbf{i}}}{dt} = \hat{\mathbf{i}} \times (\boldsymbol{\omega}_{I/L} \times \hat{\mathbf{i}}) = \boldsymbol{\omega}_{I/L} - (\boldsymbol{\omega}_{I/L} \cdot \hat{\mathbf{i}})\hat{\mathbf{i}} \tag{3.9}$$

$$\hat{\mathbf{j}} \times \frac{d\hat{\mathbf{j}}}{dt} = \hat{\mathbf{j}} \times (\boldsymbol{\omega}_{I/L} \times \hat{\mathbf{j}}) = \boldsymbol{\omega}_{I/L} - (\boldsymbol{\omega}_{I/L} \cdot \hat{\mathbf{j}})\hat{\mathbf{j}} \tag{3.10}$$

$$\hat{\mathbf{k}} \times \frac{d\hat{\mathbf{k}}}{dt} = \hat{\mathbf{k}} \times (\boldsymbol{\omega}_{I/L} \times \hat{\mathbf{k}}) = \boldsymbol{\omega}_{I/L} - (\boldsymbol{\omega}_{I/L} \cdot \hat{\mathbf{k}})\hat{\mathbf{k}} \tag{3.11}$$

Summing up Equations (3.9) - (3.11) yields

$$\boldsymbol{\omega}_{I/L} = \frac{1}{2}\left(\hat{\mathbf{i}} \times \frac{d\hat{\mathbf{i}}}{dt} + \hat{\mathbf{j}} \times \frac{d\hat{\mathbf{j}}}{dt} + \hat{\mathbf{k}} \times \frac{d\hat{\mathbf{k}}}{dt}\right) \tag{3.12}$$

First, the time derivative of the $\hat{\mathbf{k}}$ unit vector is given as

$$\frac{d\hat{\mathbf{k}}}{dt} = -\frac{1}{r}(\mathbf{v} + \dot{r}\hat{\mathbf{k}}) \tag{3.13}$$

where $\mathbf{v} = \dot{\mathbf{r}} + {}^{I}\boldsymbol{\omega}^{L} \times \mathbf{r}$. Noting that the position and velocity vectors in Frame L are written as $\mathbf{r} = -r\hat{\mathbf{k}}$ and $\dot{\mathbf{r}} = -\dot{r}\hat{\mathbf{k}}$, the following equation can be written as

$$\begin{aligned}
\dot{r} &= -\dot{\mathbf{r}} \cdot \hat{\mathbf{k}} \\
&= -\mathbf{v} \cdot \hat{\mathbf{k}} + (\boldsymbol{\omega}_{I/L} \times \mathbf{r}) \cdot \hat{\mathbf{k}} \\
&= -\mathbf{v} \cdot \hat{\mathbf{k}} + \boldsymbol{\omega}_{I/L} \cdot (\mathbf{r} \times \hat{\mathbf{k}}) \\
&= -\mathbf{v} \cdot \hat{\mathbf{k}} \tag{3.14}
\end{aligned}$$

Substituting Equation (3.14) into (3.13) yields

$$\begin{aligned}
\frac{d\hat{\mathbf{k}}}{dt} &= -\frac{1}{r}((\mathbf{v} \cdot \hat{\mathbf{i}})\hat{\mathbf{i}} + (\mathbf{v} \cdot \hat{\mathbf{j}})\hat{\mathbf{j}}) \\
&= -\frac{1}{r}(\mathbf{v} \cdot \hat{\mathbf{i}})\hat{\mathbf{i}} \tag{3.15}
\end{aligned}$$

Since the definition of the LVLH frame stipulates that the target velocity vector is perpendicular to the specific angular momentum vector $\hat{\mathbf{h}}$, it follows that $\mathbf{v} \cdot \hat{\mathbf{j}} = 0$. Similarly, the time derivative of the $\hat{\mathbf{j}}$ unit vector is written as

$$\frac{d\hat{\mathbf{j}}}{dt} = -\frac{1}{h}\left(\frac{d\mathbf{h}}{dt} + \dot{h}\hat{\mathbf{j}}\right)$$

$$= -\frac{1}{h}\left(\left(\frac{d\mathbf{h}}{dt} \cdot \hat{\mathbf{i}}\right)\hat{\mathbf{i}} + \left(\frac{d\mathbf{h}}{dt} \cdot \hat{\mathbf{k}}\right)\hat{\mathbf{k}}\right)$$

$$= -\frac{1}{h}\left(\left(\mathbf{r} \times \frac{d^2\mathbf{r}}{dt^2}\right) \cdot \hat{\mathbf{i}}\right)\hat{\mathbf{i}}$$

$$= -\frac{1}{h}\left(\frac{d^2\mathbf{r}}{dt^2} \cdot (\hat{\mathbf{i}} \times \mathbf{r})\right)\hat{\mathbf{i}}$$

$$= -\frac{r}{h}\left(\frac{d^2\mathbf{r}}{dt^2} \cdot \hat{\mathbf{j}}\right)\hat{\mathbf{i}} \tag{3.16}$$

where the following relationships are employed to simplify to Equation (3.16):

$$\dot{\mathbf{h}} = \frac{d\mathbf{h}}{dt} - \boldsymbol{\omega}_{I/L} \times \mathbf{h} = -\dot{h}\hat{\mathbf{j}} = \left(\frac{d\mathbf{h}}{dt} \cdot \hat{\mathbf{j}}\right)\hat{\mathbf{j}} \tag{3.17}$$

$$\frac{d\mathbf{h}}{dt} \cdot \hat{\mathbf{k}} = \left(\mathbf{r} \times \frac{d^2\mathbf{r}}{dt^2}\right) \cdot \hat{\mathbf{k}} = \frac{d^2\mathbf{r}}{dt^2} \cdot (\mathbf{r} \times \hat{\mathbf{k}}) = 0 \tag{3.18}$$

Finally the time derivative of vector $\hat{\mathbf{i}}$ is expressed as

$$\frac{d\hat{\mathbf{i}}}{dt} = \frac{d\hat{\mathbf{j}}}{dt} \times \hat{\mathbf{k}} + \hat{\mathbf{j}} \times \frac{d\hat{\mathbf{k}}}{dt} = \frac{r}{h}\left(\frac{d^2\mathbf{r}}{dt^2} \cdot \hat{\mathbf{j}}\right)\hat{\mathbf{j}} + \frac{1}{r}(\mathbf{v} \cdot \hat{\mathbf{i}})\hat{\mathbf{k}} \tag{3.19}$$

Substituting Equations (3.15) - ((3.19) into Equation (3.12) yields

$$\boldsymbol{\omega}_{I/L} = \omega_y\hat{\mathbf{j}} + \omega_z\hat{\mathbf{k}} = -\frac{1}{r}(\mathbf{v} \cdot \hat{\mathbf{i}})\hat{\mathbf{j}} + \frac{r}{h}\left(\frac{d^2\mathbf{r}}{dt^2} \cdot \hat{\mathbf{j}}\right)\hat{\mathbf{k}} \tag{3.20}$$

Equation (3.20) demonstrates that there is no component of the LVLH Frame L angular velocity in the direction of $\hat{\mathbf{i}}$ or V-BAR. This is due to the definition of the LVLH frame as stipulated by the construction of its axes. Therefore, ω_y is denoted as the orbital rate while ω_z is the steering rate of the orbital plane, as introduced

by Franzini et al. [1]. Futhermore, Equation (3.20) obtains an anaytical description of the LVLH angular velocity vector through the projections of the target inertially-based velocity and acceleration vectors along the LVLH axes. To further simplify the expression in Equation (3.20), the following quantities are evaluated as

$$\mathbf{v} \cdot \hat{\mathbf{i}} = \frac{1}{hr}\mathbf{v} \cdot (\mathbf{h} \times \mathbf{r}) = \frac{1}{hr}\mathbf{h} \cdot (\mathbf{r} \times \mathbf{v}) = \frac{h}{r} \tag{3.21}$$

$$\frac{d^2\mathbf{r}}{dt^2} \cdot \hat{\mathbf{j}} = \boldsymbol{\eta}_t \cdot \hat{\mathbf{j}} = \eta_{t,y} \tag{3.22}$$

where Equation (3.4) is employed in Equation (3.22). Finally, the substitution of Equations (3.21) and (3.22) into Equation (3.20) yields

$$\omega_y = -\frac{h}{r^2} \tag{3.23}$$

$$\omega_z = \frac{r}{h}\eta_{t,y} \tag{3.24}$$

Next, a general expression for the LVLH angular acceleration $^I\dot{\boldsymbol{\omega}}^L$ is obtained by direct derivation of Equation (3.20). First, the derivative of ω_y is expressed as

$$\begin{aligned}
\dot{\omega}_y &= -\frac{1}{r}\left(\frac{d^2\mathbf{r}}{dt^2} \cdot \hat{\mathbf{i}} + \mathbf{v} \cdot \frac{d\hat{\mathbf{i}}}{dt} - \frac{\dot{r}}{r}\mathbf{v} \cdot \hat{\mathbf{i}}\right) \\
&= -\frac{1}{r}\left(\frac{d^2\mathbf{r}}{dt^2} \cdot \hat{\mathbf{i}} + \mathbf{v} \cdot \frac{d\hat{\mathbf{i}}}{dt} + \dot{r}\omega_y\right)
\end{aligned} \tag{3.25}$$

The term $\mathbf{v} \cdot \frac{d\hat{\mathbf{i}}}{dt}$ can be simplified by evaluating

$$\begin{aligned}
\mathbf{v} \cdot \frac{d\hat{\mathbf{i}}}{dt} &= (\dot{r} + \boldsymbol{\omega}_{I/L} \times \mathbf{r}) \cdot \left(\frac{r}{h}\left(\frac{d^2\mathbf{r}}{dt^2} \cdot \hat{\mathbf{j}}\right)\hat{\mathbf{j}} + \frac{1}{r}(\mathbf{v} \cdot \hat{\mathbf{i}})\hat{\mathbf{k}}\right) \\
&= (-\dot{r}\hat{\mathbf{k}} - r\omega_y\hat{\mathbf{i}}) \cdot (\omega_z\hat{\mathbf{j}} - \omega_y\hat{\mathbf{j}}) \\
&= \dot{r}\omega_y
\end{aligned} \tag{3.26}$$

Substituting the term in Equation (3.26) into Equation (3.25) yields

$$\dot{\omega}_y = -\frac{1}{r}\left(\frac{d^2\mathbf{r}}{dt^2}\cdot\hat{\mathbf{i}} + 2\dot{r}\omega_y\right) \tag{3.27}$$

Likewise, the angular acceleration component along the $\hat{\mathbf{k}}$ direction is expressed

$$\dot{\omega}_z = \frac{r}{h}\left(\frac{\dot{r}}{r}\frac{d^2\mathbf{r}}{dt^2}\cdot\hat{\mathbf{j}} + \frac{d^3\mathbf{r}}{dt^3}\cdot\hat{\mathbf{j}} + \frac{d^2\mathbf{r}}{dt^2}\cdot\frac{d\hat{\mathbf{j}}}{dt} - \frac{h}{h}\frac{d^2\mathbf{r}}{dt^2}\cdot\hat{\mathbf{j}}\right) \tag{3.28}$$

Simplifying Equation 3.28 is accomplished by evaluating

$$\frac{d^2\mathbf{r}}{dt^2}\cdot\frac{d\hat{\mathbf{j}}}{dt} = \left(\left(\frac{d^2\mathbf{r}}{dt^2}\cdot\hat{\mathbf{i}}\right)\hat{\mathbf{i}} + \left(\frac{d^2\mathbf{r}}{dt^2}\cdot\hat{\mathbf{j}}\right)\hat{\mathbf{j}} + \left(\frac{d^2\mathbf{r}}{dt^2}\cdot\hat{\mathbf{k}}\right)\hat{\mathbf{k}}\right)\cdot\left(-\frac{r}{h}\left(\frac{d^2\mathbf{r}}{dt^2}\cdot\hat{\mathbf{j}}\right)\hat{\mathbf{i}}\right)$$

$$= -\frac{r}{h}\left(\frac{d^2\mathbf{r}}{dt^2}\cdot\hat{\mathbf{i}}\right)\left(\frac{d^2\mathbf{r}}{dt^2}\cdot\hat{\mathbf{j}}\right) \tag{3.29}$$

Therefore, Equation 3.28 is simplified to

$$\dot{\omega}_z = \frac{r}{h}\left(\frac{\dot{r}}{r}\frac{d^2\mathbf{r}}{dt^2}\cdot\hat{\mathbf{j}} + \frac{d^3\mathbf{r}}{dt^3}\cdot\hat{\mathbf{j}} - \frac{r}{h}\left(\frac{d^2\mathbf{r}}{dt^2}\cdot\hat{\mathbf{i}} + \frac{h}{r}\right)\frac{d^2\mathbf{r}}{dt^2}\cdot\hat{\mathbf{j}}\right) \tag{3.30}$$

By defining $\mathbf{h} = -h\hat{\mathbf{j}}$ and noting that

$$\mathbf{h} = \mathbf{r}\times\mathbf{v}$$
$$= -r\hat{\mathbf{k}}\times(\dot{\mathbf{v}} + \boldsymbol{\omega}_{I/L}\times\mathbf{r})$$
$$= -r\hat{\mathbf{k}}\times(-\dot{r}\hat{\mathbf{k}} - r\omega_y\hat{\mathbf{i}})$$
$$= r^2\omega_y\hat{\mathbf{j}} \tag{3.31}$$

Direct differentiation of Equation (3.31) yields

$$\dot{h} = -2r\dot{r}\omega_y - r^2\dot{\omega}_y = r\frac{d^2\mathbf{r}}{dt^2}\cdot\hat{\mathbf{i}} \tag{3.32}$$

which denotes the derivative of the target specific angular momentum in the LVLH frame. Equation (3.30) is further simplified by substituting Equation (3.32) such that

$$\dot{\omega}_z = \frac{r}{h}\left(\frac{\dot{r}}{r}\frac{d^2\mathbf{r}}{dt^2}\cdot\hat{\mathbf{j}} + \frac{d^3\mathbf{r}}{dt^3}\cdot\hat{\mathbf{j}} - 2\frac{r}{h}\left(\frac{d^2\mathbf{r}}{dt^2}\cdot\hat{\mathbf{i}}\right)\left(\frac{d^2\mathbf{r}}{dt^2}\cdot\hat{\mathbf{j}}\right)\right) \tag{3.33}$$

The third derivative of the target position is denoted as the target jerk defined as

$$\frac{d^3\mathbf{r}}{dt^3} = \frac{\partial}{\partial t}\left(\frac{d^2\mathbf{r}}{dt^2}\right) + \frac{\partial}{\partial \mathbf{r}}\left(\frac{d^2\mathbf{r}}{dt^2}\right)\mathbf{v} + \frac{\partial}{\partial \mathbf{v}}\left(\frac{d^2\mathbf{r}}{dt^2}\right)\frac{d^2\mathbf{r}}{dt^2} \tag{3.34}$$

where the term $\partial(d^2\mathbf{r}/dt^2)/\partial t$ accounts for the time variation in the gravitational and perturbation parameters. Franzini [1] and Casotto [33] equate this term to zero since the assumptions of a constant mass distribution and a conservative force field are employed. Therefore Equation (3.33) simplifies as

$$\dot{\omega}_z = \frac{r}{h}\left(\frac{\dot{r}}{r}\frac{d^2\mathbf{r}}{dt^2}\cdot\hat{\mathbf{j}} + \hat{\mathbf{j}}^T\frac{\partial}{\partial \mathbf{r}}\left(\frac{d^2\mathbf{r}}{dt^2}\right)\mathbf{v} - 2\frac{r}{h}\left(\frac{d^2\mathbf{r}}{dt^2}\cdot\hat{\mathbf{i}}\right)\left(\frac{d^2\mathbf{r}}{dt^2}\cdot\hat{\mathbf{j}}\right)\right) \tag{3.35}$$

In this investigation, the gravitational parameter is assumed constant, yet the expressions of the angular velocity and acceleration vectors in the LVLH frame can incorporate other perturbations as extensions of the two-body model. Perturbations including solar radiation pressure, atmospheric drag, and linearized lunar perturbation effects written as series expansions can be defined and incorporated into the relative dynamical model.

3.2.1 Nonlinear Equations of Relative Motion

Using the geometry outlined in Figure 3.1, the relative dynamics are formulated by defining

$$\boldsymbol{\rho} = x\hat{\mathbf{i}} + y\hat{\mathbf{j}} + z\hat{\mathbf{k}} \tag{3.36}$$

$$\dot{\boldsymbol{\rho}} = \dot{x}\hat{\mathbf{i}} + \dot{y}\hat{\mathbf{j}} + \dot{z}\hat{\mathbf{k}} \tag{3.37}$$

$$\tag{3.38}$$

where $\boldsymbol{\rho}$ and $\dot{\boldsymbol{\rho}}$ denote the relative position and velocity vectors of the chaser with respect to the target, defined in the LVLH frame L. To specify the chaser's position with respect to the central body, the following vector is defined as

$$\mathbf{r}_c = \mathbf{r} + \boldsymbol{\rho} = x\hat{\mathbf{i}} + y\hat{\mathbf{j}} + (z - r)\hat{\mathbf{k}} \tag{3.39}$$

$$r_c = ||\mathbf{r}_c|| = \sqrt{x^2 + y^2 + (z - r)^2} \tag{3.40}$$

Using the transport theorem, the inertially-based velocity of the chaser in LVLH coordinates is given as

$$\mathbf{v}_c = \frac{d\mathbf{r}_c}{dt} = \frac{d\mathbf{r}}{dt} + \frac{d\boldsymbol{\rho}}{dt} = \frac{d\mathbf{r}}{dt} + \dot{\boldsymbol{\rho}} + \boldsymbol{\omega}_{I/L} \times \boldsymbol{\rho} \tag{3.41}$$

where it is repeated that any quantities expressed in the form $\frac{d\mathbf{r}}{dt}$ are inertially-based quantities whereas those quantities expressed with dot notation $\dot{\boldsymbol{\rho}}$ are derivatives taken in the LVLH frame L. Taking the derivative of Equation (3.41) yields

$$\frac{d^2\mathbf{r}_c}{dt^2} = \frac{d^2\mathbf{r}}{dt^2} + \ddot{\boldsymbol{\rho}} + 2\boldsymbol{\omega}_{I/L} \times \dot{\boldsymbol{\rho}} + \dot{\boldsymbol{\omega}}_{I/L} \times \boldsymbol{\rho} + \boldsymbol{\omega}_{I/L} \times (\boldsymbol{\omega}_{I/L} \times \boldsymbol{\rho}) \tag{3.42}$$

Substituting Equations (3.4) and (3.5) into Equation (3.42) yields

$$\ddot{\boldsymbol{\rho}} + 2\boldsymbol{\omega}_{I/L} \times \dot{\boldsymbol{\rho}} + \dot{\boldsymbol{\omega}}_{I/L} \times \boldsymbol{\rho} + \boldsymbol{\omega}_{I/L} \times (\boldsymbol{\omega}_{I/L} \times \boldsymbol{\rho}) = \frac{\mu}{r^3}\mathbf{r} - \frac{\mu}{r_c^3}(\mathbf{r} + \boldsymbol{\rho}) + \Delta\boldsymbol{\eta} + \mathbf{u} \tag{3.43}$$

where $\Delta\boldsymbol{\eta}$ denotes the differences between the perturbing accelerations of the target and chaser such that

$$\Delta\boldsymbol{\eta} = \boldsymbol{\eta}_c - \boldsymbol{\eta}_t = \Delta\eta_x\hat{\mathbf{i}} + \Delta\eta_y\hat{\mathbf{j}} + \Delta\eta_z\hat{\mathbf{k}} \tag{3.44}$$

and $\mathbf{u}$ is the chaser control vector expressed in the LVLH frame. Evaluating Equation (3.43) for each component in the LVLH directions results in three second-order differential equations written as

$$\ddot{x} = \left(\omega_y^2 + \omega_z^2 - \frac{\mu}{r_c^3}\right)x + \dot{\omega}_z y - \dot{\omega}_y z + 2\omega_z\dot{y} - 2\omega_y\dot{z} + \Delta\eta_x + u_x \tag{3.45}$$

$$\ddot{y} = -\dot{\omega}_z x + \left(\omega_z^2 - \frac{\mu}{r_c^3}\right)y - \omega_y\omega_z z - 2\omega_z\dot{x} + \Delta\eta_y + u_y \tag{3.46}$$

$$\ddot{z} = \dot{\omega}_y x - \omega_y\omega_z y + \left(\omega_y^2 - \frac{\mu}{r_c^3}\right)z + 2\omega_y\dot{x} - \mu\left(\frac{1}{r^2} - \frac{r}{r_c^3}\right) + \Delta\eta_z + u_z \tag{3.47}$$

which are termed the nonlinear equations of relative motion for the two-body problem or 2B-NLERM. To implement Equations (3.45) - (3.47), the target spacecraft's time history must be computed in the LVLH frame L. The target velocity vector is expressed as

$$\mathbf{v} = \frac{d\mathbf{r}}{dt} = \dot{\mathbf{r}} + \boldsymbol{\omega}_{I/L} \times \mathbf{r} = -r\omega_y\hat{\mathbf{i}} - \dot{r}\hat{\mathbf{k}} \tag{3.48}$$

Taking the time derivative of Equation (3.48) yields

$$\begin{aligned}
\frac{d\mathbf{v}}{dt} &= \dot{\mathbf{v}} + \boldsymbol{\omega}_{I/L} \times \mathbf{v} \\
&= -(r\dot{\omega}_y + 2\dot{r}\omega_y)\hat{\mathbf{i}} - r\omega_y\omega_z\hat{\mathbf{j}} + (r\omega_y^2 - \ddot{r})\hat{\mathbf{k}} \\
&= \eta_{t,x}\hat{\mathbf{i}} + \eta_{t,y}\hat{\mathbf{j}} + (r\omega_y^2 - \ddot{r} + \eta_{t,z})\hat{\mathbf{k}}
\end{aligned} \tag{3.49}$$

Evaluating for the scalar value $\ddot{r}$ by equating the components along the $\hat{\mathbf{k}}$ direction yields

$$\ddot{r} = -\frac{\mu}{r^2} + r\omega_y^2 - \eta_{t,z} \qquad (3.50)$$

which is integrated twice to obtain a time history for the target distance r and speed $\dot{r}$, respectively. The nonlinear equations of relative motion for the two-body problem (2B-NLERM) are fully described using 9 first order differential equations with the full state vector defined as

$$\mathbf{X}_{\text{state}} = \begin{bmatrix} x, & y, & z, & \dot{x}, & \dot{y}, & \dot{z}, & r, & \dot{r}, & h \end{bmatrix}^T$$

with each of the state vector's derivatives expressed in analytical form. Differential perturbing forces are expressed in the LVLH frame L and added to the accelerations for the relative position vector $\boldsymbol{\rho}$. *For the rest of the investigation, the additional perturbing forces are omitted from the analysis since they are not incorporated for the applications demonstrated in this work.* Nevertheless, the formulation presented (based on the work in Franzini et al. [1]) allows for the inclusion of other perturbations since the angular velocity and accelerations of the LVLH frame are written in general form.

3.2.2 Linear Equations of Relative Motion

Simplifications to the 2B-NLERM are obtained by linearizing the gravitational accelerations due to the Moon and the Earth. Assuming that there are no additional perturbations, Equation (3.43) simplifies to

$$\ddot{\boldsymbol{\rho}} + 2\boldsymbol{\omega}_{I/L} \times \dot{\boldsymbol{\rho}} + \dot{\boldsymbol{\omega}}_{I/L} \times \boldsymbol{\rho} + \boldsymbol{\omega}_{I/L} \times (\boldsymbol{\omega}_{I/L} \times \boldsymbol{\rho}) = \frac{\mu}{r^3}\mathbf{r} - \frac{\mu}{r_c^3}(\mathbf{r} + \boldsymbol{\rho}) + \mathbf{u} \qquad (3.51)$$

Moreover, the angular velocity and acceleration vectors of LVLH frame L with respect to the inertial frame I are expressed as

$$\boldsymbol{\omega}_{L/I} = -\frac{h}{r^2}\hat{\mathbf{j}} = \dot{f}\hat{\mathbf{j}} \tag{3.52}$$

$$\dot{\boldsymbol{\omega}}_{L/I} = -2\frac{\dot{r}\dot{f}}{r}\hat{\mathbf{j}} \tag{3.53}$$

where $\dot{f}$ is the target true anomaly rate. A Taylor expansion to the first order is applied around the target position such that

$$\frac{\mu}{r_c^3}\mathbf{r}_c \approx \frac{\mu}{r^3}\mathbf{r} + \frac{\partial}{\partial\mathbf{r}}\left[\frac{\mu}{r^3}\mathbf{r}\right](\mathbf{r}_c - \mathbf{r})$$

$$\approx \frac{\mu}{r^3}\mathbf{r} + \frac{\mu}{r^3}\left(\mathbf{I} - 3\frac{\mathbf{rr}^T}{r^2}\right)\boldsymbol{\rho} \tag{3.54}$$

where $\mathbf{r}_c$ denotes the position vector of the chaser and $\boldsymbol{\rho}$ is the relative vector from the target to the chaser. Substituting Equation (3.54) into (3.51) yields

$$\ddot{\boldsymbol{\rho}} + 2\boldsymbol{\omega}_{I/L} \times \dot{\boldsymbol{\rho}} + \dot{\boldsymbol{\omega}}_{I/L} \times \boldsymbol{\rho} + \boldsymbol{\omega}_{I/L} \times (\boldsymbol{\omega}_{I/L} \times \boldsymbol{\rho}) = -\frac{\mu}{r^3}\left(\mathbf{I} - 3\frac{\mathbf{rr}^T}{r^2}\right)\boldsymbol{\rho} + \mathbf{u} \tag{3.55}$$

what are denoted as the linear equations of relative motion or 2B-LERM. The employment of the Taylor series expansion for the gravitation acceleration stipulates that the chaser and target must be sufficiently close to one another to be considered valid in the domain of linearization. Alfriend et al. [11] conclude that the 2B-LERM provide an accurate depiction of the relative dynamics when $||\boldsymbol{\rho}|| < 50$ km. Further simplifications to the linear equation are obtained by utilizing the angular momentum expression from the Keplerian model written as

$$h = \sqrt{\mu p} \tag{3.56}$$

where h and p denote the specific angular momentum and semilatus rectum of the target around the central body, respectively. Using the relationship in Equation (3.56) simplifies the following expression

$$\frac{\mu}{r^3} = \frac{h^2}{pr^3} = \dot{f}^2 \frac{r}{p} \qquad (3.57)$$

Thus, the following term in Equation (3.55) is simplified to

$$\mathbf{I} - 3\frac{\mathbf{r}\mathbf{r}^T}{r^2} = \begin{bmatrix} 1 & 0 & 0 \\ 0 & 1 & 0 \\ 0 & 0 & 2 \end{bmatrix} \qquad (3.58)$$

where $\mathbf{r} = -r\hat{\mathbf{k}}$. Evaluating the 2B-LERM in component-wise form yields

$$\ddot{x} = \dot{f}^2 \left(1 - \frac{r}{p} \right) x - 2\dot{f} \left(\frac{\dot{r}}{r} z - \dot{z} \right) + u_x \qquad (3.59)$$

$$\ddot{y} = -\frac{r}{p} \dot{f}^2 y + u_y \qquad (3.60)$$

$$\ddot{z} = 2\dot{f} \left(\frac{\dot{r}}{r} x - \dot{x} \right) + \dot{f}^2 \left(1 + 2\frac{r}{p} \right) z + u_z \qquad (3.61)$$

It is apparent from Equations (3.59) - (3.61) that the 2B-LERM indicate a decoupling between the in-plane motion along the $\hat{\mathbf{i}} - \hat{\mathbf{k}}$ plane and the out-of-plane motion along the $\hat{\mathbf{j}}$ direction.

3.2.3 Euler-Hill (HCW) Equations

Equations (3.59) - (3.61) further simplify under additional assumptions when the target orbit is circular. To that end, the angular velocity of the LVLH frame $\boldsymbol{\omega}_{I/L}$ is constant and equivalent to the mean motion of the target orbit around the central body, expressed as $n = 2\pi/P$, where P denotes the target period. Moreover the target orbital radius r is equal to its semilatus rectum p. The equations of motion are them simplified as

$$\ddot{x} = 2n\dot{z} + u_x \tag{3.62}$$

$$\ddot{y} = -n^2 y + u_y \tag{3.63}$$

$$\ddot{z} = -2n\dot{x} + 3n^2 z + u_x \tag{3.64}$$

Equations (3.62)- (3.64) are referred to as Hill's equations, first developed to characterize the Moon's motion around the Earth. In relative motion applications, these equations are also called the Hill-Clohessy-Wiltshire (HCW) equations since they were introduced by Clohessy and Wiltshire to facilitate the design of a terminal rendezvous system [2].

3.3   Relative Motion in the Restricted Three-Body Problem

The two-body models for relative motion introduced in the preceding section have been investigated and applied extensively for Keplerian-based dynamical systems. Though these models have been largely successful at characterizing the relative motion between spacecraft in their respective regimes, they are inadequate for describing the dynamics between spacecraft in orbits that exist in more complicated dynamical systems. Such dynamical systems, like the restricted three-body problem, have to be incorporated in the formulation of the relative equations of motion to accurately analyze relative motion in the reference orbits for the Gateway and Artemis missions. Relative motion in the restricted three-body problem is conventionally obtained by differencing the equations of motion for two spacecraft, namely a target and a chaser, under the influence of two primary bodies. The equations are subsequently developed into a local frame to obtain a description of the relative dynamics with respect to the target. The frame employed in the derivation of the equations is the Local-Vertical-Local-Horizontal (LVLH) frame, identical to the one introduced in Figure 3.1. The LVLH frame is useful for relative motion analysis since it incorporates relative information between the spacecraft and can be utilized to design a relative guidance, navigation, and control system to maneuver the chaser to a desired relative position with respect to the target. In this investigation, the nonlinear relative equations of motion

for the restricted three-body problem (3B-NLERM) are formulated with a procedure identical to the one proposed by Franzini et al. [1]. The advantage of this formulation lies in the fact that the equations of motion are developed in the LVLH frame L using only kinematic relationships between the inertial frame I and the synodic frame M, where M is based at the second primary. Moreover, the derivation employs no assumptions for the Earth-Moon dynamics allowing the equations to incorporate frameworks consistent with the CR3BP and ER3BP models. Simplifications to the 3B-NLERM are made by linearizing the gravitational accelerations due to the two primaries by a Taylor series about the target position obtaining the linear relative equations of motion for the restricted three-body problem (3B-LERM). Ultimately, the 3B-LERM provide first-order linear variational equations governing the relative dynamics which are used to construct a relative state transition matrix (RSTM). The RSTM serves as a foundation for the development of shooting schemes that can be applied to a variety of orbital rendezvous and spacecraft loitering scenarios.

3.3.1 Nonlinear Equations of Relative Motion

The nonlinear equations of relative motion are formulated to characterize the relative dynamics between a chaser and target subject to the gravitational influences of the Earth and the Moon. The equations governing the motion of both spacecraft with respect to the Moon are written as

$$\left[\ddot{\mathbf{r}}\right]_I = -\mu \frac{\mathbf{r}}{r^3} - (1-\mu)\left(\frac{\mathbf{r} + \mathbf{r}_{em}}{||\mathbf{r} + \mathbf{r}_{em}||^3} - \frac{\mathbf{r}_{em}}{r_{em}^3}\right) \tag{3.65}$$

$$\left[\ddot{\mathbf{r}}_c\right]_I = -\mu \frac{\mathbf{r}_c}{r_c^3} - (1-\mu)\left(\frac{\mathbf{r}_c + \mathbf{r}_{em}}{||\mathbf{r}_c + \mathbf{r}_{em}||^3} - \frac{\mathbf{r}_{em}}{r_{em}^3}\right) \tag{3.66}$$

where $\mathbf{r}$ and $\mathbf{r}_c$ denote the position vector measured from the Moon to the target and chaser, respectively. Moreover, $\mathbf{r}_{em}$ is the position vector from the Earth to the Moon with r_{em} as its norm. In this investigation, the following parameters are used to describe the Earth-Moon system:

- nondimensional gravitational parameter $\mu = 0.012151$

- semimajor axis of the Moon as $a = 384400$ km

- eccentricity of the Moon as $e = 0$ for the CR3BP and $e = 0.0549$ for the ER3BP

- mean motion of the moon as $n_{\text{Moon}} = 2.6814e - 6$ rad/s

- All quantities are nondimensionalized using a and n_{Moon}

Moreover, it is understood that any derivatives with surrounding brackets such as

$$\left[\dot{\mathbf{r}}\right]_I \;,\; \left[\dot{\mathbf{r}}\right]_M \;,\; \left[\dot{\mathbf{r}}\right]_L$$

denote derivatives taken in the inertial frame I, Moon frame M, and LVLH frame L, respectively. Using the geometry depicted in Figure 3.1, the chaser position with respect to the Moon is expressed as

$$\mathbf{r}_c = \mathbf{r} + \boldsymbol{\rho} \tag{3.67}$$

where $\boldsymbol{\rho}$ denotes the relative position vector from the target to the chaser. The time derivative of Equation (3.67) in the inertial frame I follows as

$$\left[\dot{\mathbf{r}}_c\right]_I = \left[\dot{\mathbf{r}}\right]_I + \left[\dot{\boldsymbol{\rho}}\right]_I \tag{3.68}$$

$$= \left[\dot{\mathbf{r}}\right]_I + \left[\dot{\boldsymbol{\rho}}\right]_L + \boldsymbol{\omega}_{L/I} \times \boldsymbol{\rho} \tag{3.69}$$

where $\boldsymbol{\omega}_{L/I}$ denotes the angular velocity of the LVLH frame L with respect to the inertial frame I. Differentiating Equation (3.69) obtains

$$\left[\ddot{\mathbf{r}}_c\right]_I = \left[\ddot{\mathbf{r}}\right]_I + \left[\ddot{\boldsymbol{\rho}}\right]_L + 2\boldsymbol{\omega}_{L/I} \times \left[\dot{\boldsymbol{\rho}}\right]_L + \left[\dot{\boldsymbol{\omega}}_{L/I}\right]_L \times \boldsymbol{\rho} + \boldsymbol{\omega}_{L/I} \times \left(\boldsymbol{\omega}_{L/I} \times \boldsymbol{\rho}\right) \tag{3.70}$$

where

$$\left[\dot{\boldsymbol{\omega}}_{L/I}\right]_I = \left[\dot{\boldsymbol{\omega}}_{L/I}\right]_L$$

Substituting Equations (3.65) and (3.66) into (3.70) yields

$$\left[\ddot{\boldsymbol{\rho}}\right]_L = -2\boldsymbol{\omega}_{L/I}\times\left[\dot{\boldsymbol{\rho}}\right]_L - \left[\dot{\boldsymbol{\omega}}_{L/I}\right]_L \times \boldsymbol{\rho} - \boldsymbol{\omega}_{L/I} \times \left(\boldsymbol{\omega}_{L/I} \times \rho\right)$$
$$+ \mu\left(\frac{\mathbf{r}}{r^3} - \frac{\mathbf{r}+\boldsymbol{\rho}}{||\mathbf{r}+\boldsymbol{\rho}||^3}\right) + (1-\mu)\left(\frac{\mathbf{r}+\mathbf{r}_{em}}{||\mathbf{r}+\mathbf{r}_{em}||^3} - \frac{\mathbf{r}+\boldsymbol{\rho}+\mathbf{r}_{em}}{||\mathbf{r}+\boldsymbol{\rho}+\mathbf{r}_{em}||^3}\right)$$
$$(3.71)$$

which are referred to as the nonlinear equations of relative motion for the restricted three-body problem (3B-NLERM). The angular velocity of the LVLH frame L with respect to the inertial frame I is computed by adding the following angular velocity vectors as

$$\boldsymbol{\omega}_{L/I} = \boldsymbol{\omega}_{L/M} + \boldsymbol{\omega}_{M/I} \qquad (3.72)$$

where $\boldsymbol{\omega}_{L/M}$ and $\boldsymbol{\omega}_{M/I}$ denote the angular velocity vector of frame L with respect to frame M and of frame M with respect to frame I, respectively. Likewise, the time derivative of $\boldsymbol{\omega}_{L/I}$ is evaluated as

$$\left[\dot{\boldsymbol{\omega}}_{L/I}\right]_L = \left[\dot{\boldsymbol{\omega}}_{L/M}\right]_L + \left[\dot{\boldsymbol{\omega}}_{M/I}\right]_L$$
$$= \left[\dot{\boldsymbol{\omega}}_{L/M}\right]_L + \left[\dot{\boldsymbol{\omega}}_{M/I}\right]_M - \boldsymbol{\omega}_{L/M} \times \boldsymbol{\omega}_{M/I} \qquad (3.73)$$

Equations (3.71)-(3.73) constitute a set of time-varying nonlinear equations where

- The target's motion around the Moon is characterized by $\mathbf{r}$, $\boldsymbol{\omega}_{L/M}$, and $\left[\dot{\boldsymbol{\omega}}_{L/M}\right]_L$

- The Moon's orbital motion is described by $\mathbf{r}_{em}$, $\boldsymbol{\omega}_{M/I}$, and $\left[\dot{\boldsymbol{\omega}}_{M/I}\right]_L$

Similar to the process outlined in the previous section resulting in an analytical description of the motion of frame L with respect to frame I, expressions are derived to describe the components of $\boldsymbol{\omega}_{L/M}$ and $[\dot{\boldsymbol{\omega}}_{L/M}]_L$. The terms of $\boldsymbol{\omega}_{M/I}$, and $[\dot{\boldsymbol{\omega}}_{M/I}]_L$ can be evaluated by employing the CR3BP or the ER3BP. Thus, using Equation (3.20), the angular velocity of Frame L is given as

$$\boldsymbol{\omega}_{L/M} = \omega_{L/M}^y \hat{\mathbf{j}} + \omega_{L/M}^z \hat{\mathbf{k}} \tag{3.74}$$

$$= \left(-\frac{1}{r}[\dot{\mathbf{r}}]_M \cdot \hat{\mathbf{i}} \right)\hat{\mathbf{j}} + \left(\frac{r}{h}[\ddot{\mathbf{r}}]_M \cdot \hat{\mathbf{j}} \right)\hat{\mathbf{k}} \tag{3.75}$$

Evaluation of the dot products in Equation (3.75) yields

$$\omega_{L/M}^y = -\frac{1}{r}[\dot{\mathbf{r}}]_M \cdot \hat{\mathbf{i}}$$

$$= -\frac{1}{hr^2}[\dot{\mathbf{r}}]_M \cdot (\mathbf{h} \times \mathbf{r})$$

$$= -\frac{1}{hr^2}\mathbf{h} \cdot (\mathbf{r} \times [\dot{\mathbf{r}}]_M)$$

$$= -\frac{h}{r^2} \tag{3.76}$$

which is identical to the two-body case. Similarly,

$$\omega_{L/M}^z = \frac{r}{h}[\ddot{\mathbf{r}}]_M \cdot \hat{\mathbf{j}}$$

$$= -\frac{r}{h^2}\mathbf{h} \cdot [\ddot{\mathbf{r}}]_M \tag{3.77}$$

where $[\ddot{\mathbf{r}}]_M$ denotes the target acceleration in frame M and is expressed as

$$[\ddot{\mathbf{r}}]_M = -2\boldsymbol{\omega}_{M/I} \times [\dot{\mathbf{r}}]_M - [\dot{\boldsymbol{\omega}}_{M/I}]_M \times \mathbf{r} - \boldsymbol{\omega}_{M/I} \times (\boldsymbol{\omega}_{M/I} \times \mathbf{r})$$

$$- \mu\frac{\mathbf{r}}{r^3} - (1-\mu)\left(\frac{\mathbf{r} + \mathbf{r}_{em}}{||\mathbf{r} + \mathbf{r}_{em}||^3} - \frac{\mathbf{r}_{em}}{r_{em}^3} \right) \tag{3.78}$$

The angular acceleration components along the LVLH frame are computed by differentiating Equations (3.76) and (3.77), respectively. Therefore,

$$\dot{\omega}_{L/M}^{y} = -\frac{\dot{h}}{r^2} + 2\frac{\dot{r}h}{r^3} = -\frac{1}{r}\left(\frac{\dot{h}}{r} + 2\dot{r}\omega_{L/M}^{y}\right) \tag{3.79}$$

where it follows that the derivative of the norm of $\mathbf{r}$ is computed as

$$\dot{r} = \frac{1}{r}\mathbf{r} \cdot [\dot{\mathbf{r}}]_{M} \tag{3.80}$$

The second angular acceleration component is evaluated as

$$\dot{\omega}_{L/M}^{z} = -\left(\frac{\dot{r}}{h^2} - 2\frac{r\dot{h}}{h^3}\right)\mathbf{h} \cdot [\ddot{\mathbf{r}}]_{M} - \frac{r}{h^2}([\dot{\mathbf{h}}]_{M} \cdot [\ddot{\mathbf{r}}]_{M} + \mathbf{h} \cdot [\dddot{\mathbf{r}}]_{M})$$

$$= \left(\frac{\dot{r}}{r} - 2\frac{\dot{h}}{h}\right)\omega_{L/M}^{z} - \frac{r}{h^2}\mathbf{h} \cdot [\dddot{\mathbf{r}}]_{M} \tag{3.81}$$

where the following relationships are used:

$$\mathbf{h} = \mathbf{r} \times [\dot{\mathbf{r}}]_{M} \tag{3.82}$$

$$[\dot{\mathbf{h}}]_{M} \cdot [\ddot{\mathbf{r}}]_{M} = (\mathbf{r} \times [\ddot{\mathbf{r}}]_{M}) \cdot [\ddot{\mathbf{r}}]_{M} = 0 \tag{3.83}$$

$$\dot{h} = -[\dot{\mathbf{h}}]_{M} \cdot \hat{\mathbf{j}} \tag{3.84}$$

Differentiating Equation (3.78) obtains an expression for the target jerk as

$$[\dddot{\mathbf{r}}]_{M} = -2\boldsymbol{\omega}_{M/I} \times [\ddot{\mathbf{r}}]_{M} - 3[\dot{\boldsymbol{\omega}}_{M/I}] \times [\dot{\mathbf{r}}]_{M} - [\ddot{\boldsymbol{\omega}}_{M/I}] \times \mathbf{r}$$

$$- [\dot{\boldsymbol{\omega}}_{M/I}] \times (\boldsymbol{\omega}_{M/I} \times \mathbf{r}) - \boldsymbol{\omega}_{M/I} \times ([\dot{\boldsymbol{\omega}}_{M/I}] \times \mathbf{r})$$

$$- \boldsymbol{\omega}_{M/I} \times (\boldsymbol{\omega}_{M/I} \times [\dot{\mathbf{r}}]_{M}) - \mu\frac{\partial}{\partial\mathbf{r}}\left[\frac{\mathbf{r}}{r^3}\right][\dot{\mathbf{r}}]_{M} - (1-\mu)\frac{\partial}{\partial\mathbf{r}}\left[\frac{\mathbf{r}+\mathbf{r}_{em}}{||\mathbf{r}+\mathbf{r}_{em}||^3}\right]([\dot{\mathbf{r}}]_{M} + [\dot{\mathbf{r}}_{em}]_{M})$$

$$+ (1-\mu)\frac{\partial}{\partial\mathbf{r}_{em}}\left[\frac{\mathbf{r}_{em}}{r_{em}^3}\right][\dot{\mathbf{r}}_{em}]_{M} \tag{3.85}$$

where

$$[\dot{\mathbf{r}}_{em}]_M = [\dot{\mathbf{r}}_{em}]_I - \boldsymbol{\omega}_{M/I} \times \mathbf{r}_{em}$$

and

$$\frac{\partial}{\partial \mathbf{q}}\left[\frac{\mathbf{q}}{q^3}\right] = \frac{1}{q^3}\left(\mathbf{I} - 3\frac{\mathbf{q}\mathbf{q}^T}{q^2}\right)$$

In conclusion, the angular components of the LVLH frame angular velocity and accelerations are expressed in terms of kinematic relationships between the two frames with quantities computed in frame M.

CR3BP Assumption

Simplifications to the 3B-NLERM are obtained by assuming that the two primaries, namely the Earth and the Moon, are described using the CR3BP. As a result, a number of the time-varying parameters are reduced to zero, such that

- The position vector from the Earth to the Moon is $\mathbf{r}_{em} = -\hat{\mathbf{i}}_m$

- The velocity vector from the Earth to the Moon is $[\dot{\mathbf{r}}_{em}]_M = \mathbf{0}$

- The angular velocity of frame M with respect to frame I is $\boldsymbol{\omega}_{M/I} = \hat{\mathbf{k}}_m$

- The angular acceleration of frame M with respect to frame I is $[\dot{\boldsymbol{\omega}}_{M/I}]_M = \mathbf{0}$

- The derivative of the angular acceleration of frame M with respect to frame I is $[\ddot{\boldsymbol{\omega}}_{M/I}]_M = \mathbf{0}$

where the quantities $\mathbf{r}_{em}$ and $\boldsymbol{\omega}_{M/I}$ have unitary norms due to the employment of nondimensional quantities. Moreover, the angular velocity and acceleration vector of frame L with respect to frame I are simplified as

$$\boldsymbol{\omega}_{L/I} = \boldsymbol{\omega}_{L/M} + \hat{\mathbf{k}}_m \tag{3.86}$$

$$[\dot{\boldsymbol{\omega}}_{L/I}]_L = [\dot{\boldsymbol{\omega}}_{L/M}]_L - \boldsymbol{\omega}_{L/M} \times \hat{\mathbf{k}}_m \tag{3.87}$$

Moreover, the target acceleration and jerk vectors simplify to

$$[\ddot{\mathbf{r}}]_M = -2\boldsymbol{\omega}_{M/I} \times [\dot{\mathbf{r}}]_M - \boldsymbol{\omega}_{M/I} \times (\boldsymbol{\omega}_{M/I} \times \mathbf{r}) - \mu\frac{\mathbf{r}}{r^3} - (1-\mu)\left(\frac{\mathbf{r}+\mathbf{r}_{em}}{||\mathbf{r}+\mathbf{r}_{em}||^3} - \mathbf{r}_{em}\right) \tag{3.88}$$

$$[\dddot{\mathbf{r}}]_M = -2\boldsymbol{\omega}_{M/I} \times [\ddot{\mathbf{r}}]_M - \boldsymbol{\omega}_{M/I} \times (\boldsymbol{\omega}_{M/I} \times [\dot{\mathbf{r}}]) - \mu\frac{\partial}{\partial\mathbf{r}}\left[\frac{\mathbf{r}}{r^3}\right][\dot{\mathbf{r}}]_M - (1-\mu)\frac{\partial}{\partial\mathbf{r}}\left[\frac{\mathbf{r}+\mathbf{r}_{em}}{||\mathbf{r}+\mathbf{r}_{em}||^3}\right][\dot{\mathbf{r}}]_M \tag{3.89}$$

The equations of relative motion in frame L are thus obtained by evaluating the angular velocity and acceleration components using the formulated analytical expressions. To implement the equations, the following state vector is defined such that

$$\mathbf{X}_{\text{state}} = \left[f_{\text{M}}, \ r_{x,M}, \ r_{y,M}, \ r_{z,M}, \ v_{x,M}, \ v_{y,M}, \ v_{z,M}, \ x, \ y, \ z, \ \dot{x}, \ \dot{y}, \ \dot{z}, \ \omega_y, \ \omega_z\right]^T$$

where f_M is the Moon's true anomaly, $r_{i,M}$ denote the target position in Frame M, $v_{i,M}$ denote the target velocity in Frame M, x, y, z define the relative position vector in Frame L, $\dot{x}, \dot{y}, \dot{z}$ pertain to the relative velocity vector in Frame L, and ω_y, ω_z are the angular velocity components of frame L with respect to frame M.

3.3.2   Linearized Equations of Relative Motion

As proposed in Franzini et al. [1], the nonlinear relative equations of motion, 3B-NLERM, can be further simplified by linearizing the gravitational accelerations around the target position. Consider the gravitational acceleration on the chaser due to the two primaries written as

$$\mathbf{g}_m(\mathbf{r}_c) = -\mu \frac{\mathbf{r}_c}{r_c^3} \tag{3.90}$$

$$\mathbf{g}_e(\mathbf{r}_c + \mathbf{r}_{em}) = -(1-\mu)\frac{\mathbf{r}_c + \mathbf{r}_{em}}{||\mathbf{r}_c + \mathbf{r}_{em}||^3} \tag{3.91}$$

where $\mathbf{g}_m$ and $\mathbf{g}_e$ denote the gravitational accelerations due to the Moon and the Earth, respectively. Employing a Taylor series around the target position and retaining to the first order yields the approximate expression for the chaser acceleration due to the Moon as

$$\mathbf{g}_m(\mathbf{r}_c) \approx \mathbf{g}_m(\mathbf{r}) + \frac{\partial \mathbf{g}_m(\mathbf{q})}{\partial \mathbf{q}}\bigg|_{\mathbf{q}=\mathbf{r}}(\mathbf{r}_c - \mathbf{r}) = -\mu\frac{\mathbf{r}}{r^3} - \frac{\mu}{r^3}\left(\mathbf{I} - 3\frac{\mathbf{r}\mathbf{r}^T}{r^2}\right)\boldsymbol{\rho} \tag{3.92}$$

Likewise, the chaser acceleration due to the Earth is approximated as

$$\mathbf{g}_e(\mathbf{r}_c + \mathbf{r}_{em}) \approx \mathbf{g}_e(\mathbf{r} + \mathbf{r}_{em}) + \frac{\partial \mathbf{g}_e(\mathbf{q})}{\partial \mathbf{q}}\bigg|_{\mathbf{q}=\mathbf{r}+\mathbf{r}_{em}}(\mathbf{r}_c - \mathbf{r})$$

$$= -(1-\mu)\frac{\mathbf{r} + \mathbf{r}_{em}}{||\mathbf{r} + \mathbf{r}_{em}||^3} - \frac{1-\mu}{||\mathbf{r} + \mathbf{r}_{em}||^3}\left(\mathbf{I} - 3\frac{(\mathbf{r} + \mathbf{r}_{em})(\mathbf{r} + \mathbf{r}_{em})^T}{||\mathbf{r} + \mathbf{r}_{em}||^2}\right)\boldsymbol{\rho}$$

$$\tag{3.93}$$

The gravitational accelerations approximated with the Taylor series expansion in Equations (3.92) and (3.93) can be substituted into Equation (3.71) to obtain the linear equations of motion.

3.3.3 Summary of Relative Motion Sets

To summarize the relative motion sets, two skew symmetric matrices that contain components of the angular velocity and acceleration vectors are introduced such that

$$\boldsymbol{\Omega}_{L/I} = \begin{bmatrix} 0 & -\omega_{L/I}^z & \omega_{L/I}^y \\ \omega_{L/I}^z & 0 & -\omega_{L/I}^x \\ -\omega_{L/I}^y & \omega_{L/I}^x & 0 \end{bmatrix} \qquad \dot{\boldsymbol{\Omega}}_{L/I} = \begin{bmatrix} 0 & -\dot{\omega}_{L/I}^z & \dot{\omega}_{L/I}^y \\ \dot{\omega}_{L/I}^z & 0 & -\dot{\omega}_{L/I}^x \\ -\dot{\omega}_{L/I}^y & \dot{\omega}_{L/I}^x & 0 \end{bmatrix}$$

where

$$\boldsymbol{\omega}_{L/I} = \omega_{L/I}^x \hat{\mathbf{i}} + \omega_{L/I}^y \hat{\mathbf{j}} + \omega_{L/I}^z \hat{\mathbf{k}} \qquad [\dot{\boldsymbol{\omega}}_{L/I}]_L = \dot{\omega}_{L/I}^x \hat{\mathbf{i}} + \dot{\omega}_{L/I}^y \hat{\mathbf{j}} + \dot{\omega}_{L/I}^z \hat{\mathbf{k}}$$

The skew symmetric matrices allow the relative motion sets to be written more compactly. The distinction between the relative motion sets used in the ER3BP and CR3BP is made by the assumptions characterizing the Earth-Moon motion.

ER3BP Relative Motion Equations

Assuming that the ER3BP is employed to describe the Earth-Moon system, the Moon's motion is computed using Keplerian orbit theory, with the Earth as its central body. The analytical solution available in the two-body problem provides the quantities

- $\mathbf{r}_{em}$: the position vector from the Earth to the Moon

- $\boldsymbol{\omega}_{M/I}$: the angular velocity of frame M with respect to frame I

- $[\dot{\boldsymbol{\omega}}_{M/I}]_M$: the angular acceleration of frame M with respect to frame I

As a result, the three-body elliptical nonlinear equations of motion or 3B-ENLERM are implemented to describe the relative dynamics as

$$[\ddot{\boldsymbol{\rho}}]_L = -2\boldsymbol{\Omega}_{L/I}[\dot{\boldsymbol{\rho}}]_L - ([\dot{\boldsymbol{\Omega}}_{L/I}]_L + \boldsymbol{\Omega}_{L/I}^2)\boldsymbol{\rho}$$
$$+ \mu\left(\frac{\mathbf{r}}{r^3} - \frac{\mathbf{r}+\boldsymbol{\rho}}{||\mathbf{r}+\boldsymbol{\rho}||^3}\right) + (1-\mu)\left(\frac{\mathbf{r}+\mathbf{r}_{em}}{||\mathbf{r}+\mathbf{r}_{em}||^3} - \frac{\mathbf{r}+\boldsymbol{\rho}+\mathbf{r}_{em}}{||\mathbf{r}+\boldsymbol{\rho}+\mathbf{r}_{em}||^3}\right)$$
$$(3.94)$$

where

- $\boldsymbol{\omega}_{L/I} = \boldsymbol{\omega}_{L/M} + \boldsymbol{\omega}_{M/I}$

- $[\dot{\boldsymbol{\omega}}_{L/I}]_{L} = [\dot{\boldsymbol{\omega}}_{L/M}]_{L} + [\dot{\boldsymbol{\omega}}_{M/I}]_{M} - \boldsymbol{\omega}_{L/M} \times \boldsymbol{\omega}_{M/I}$

- $\boldsymbol{\omega}_{L/M}$ is a function of the target acceleration $[\ddot{\mathbf{r}}]_{M}$ given in Equation (3.78)

- $\dot{\boldsymbol{\omega}}_{L/M}$ is a function of the target jerk $[\dddot{\mathbf{r}}]_{M}$ given in Equation (3.85)

The equations of motion can be further expressed as a nonlinear system, assuming that the chaser is maneuverable by a control vector $\mathbf{u}(\tau)$. Thus, Equation (3.94) is written as

$$\dot{\mathbf{x}}(\tau) = \mathbf{f}(\tau, \mathbf{x}(\tau)) + \mathbf{B}\mathbf{u}(\tau) \tag{3.95}$$

where

$$\mathbf{x}(\tau) = \begin{bmatrix} \boldsymbol{\rho}(\tau) \\ [\dot{\boldsymbol{\rho}}(\tau)]_{L} \end{bmatrix} \quad \text{and} \quad \mathbf{B} = \begin{bmatrix} \mathbf{0}_{3\times3} \\ \mathbf{I}_{3\times3} \end{bmatrix}$$

and $\mathbf{x}(\tau) \in \mathbb{R}^{6}$, $\mathbf{f} : [0, +\infty) \times \mathbb{R}^{6} \to \mathbb{R}^{6}$, $\mathbf{B} \in \mathbb{R}^{6\times3}$. Moreover, the gravitational acceleration terms are linearized around the target position to obtain the three body elliptical relative equations of motion or 3B-ELERM as

$$[\ddot{\boldsymbol{\rho}}]_{L} = -2\boldsymbol{\Omega}_{L/I}[\dot{\boldsymbol{\rho}}]_{L} - \left([\dot{\boldsymbol{\Omega}}_{L/I}]_{L} + \boldsymbol{\Omega}_{L/I}^{2} + \frac{\mu}{r^{3}}\left(\mathbf{I} - 3\frac{\mathbf{r}\mathbf{r}^{T}}{r^{2}} \right) \right. \tag{3.96}$$

$$\left. + \frac{1-\mu}{||\mathbf{r} + \mathbf{r}_{em}||^{3}}\left(\mathbf{I} - 3\frac{(\mathbf{r} + \mathbf{r}_{em})(\mathbf{r} + \mathbf{r}_{em})^{T}}{||\mathbf{r} + \mathbf{r}_{em}||^{2}} \right) \right)\boldsymbol{\rho} \tag{3.97}$$

Additionally, Equation (3.97) is written in state-space form such that

$$\dot{\mathbf{x}}(\tau) = \mathbf{A}(\tau)\mathbf{x}(\tau) + \mathbf{B}\mathbf{u}(\tau) \tag{3.98}$$

where the system matrix $\mathbf{A}(\tau)$ is defined as

$$\mathbf{A}(\tau) = \begin{bmatrix} \mathbf{0}_{3 \times 3} & \mathbf{I}_{3 \times 3} \\ \mathbf{A}_{\boldsymbol{\rho}\dot{\boldsymbol{\rho}}}(\tau) & -2\boldsymbol{\Omega}_{L/I}(\tau) \end{bmatrix}$$

and

$$\mathbf{A}_{\boldsymbol{\rho}\dot{\boldsymbol{\rho}}}(\tau) = -[\dot{\boldsymbol{\Omega}}_{L/I}(\tau)] - \boldsymbol{\Omega}_{L/I}(\tau)^2 - \frac{\mu}{r(\tau)^3}\left(\mathbf{I} - 3\frac{\mathbf{r}(\tau)\mathbf{r}(\tau)^T}{r(\tau)^2}\right)$$

$$+ \frac{1-\mu}{||\mathbf{r}(\tau) + \mathbf{r}_{em}(\tau)||^3}\left(\mathbf{I} - 3\frac{(\mathbf{r}(\tau) + \mathbf{r}_{em}(\tau))(\mathbf{r}(\tau) + \mathbf{r}_{em}(\tau))^T}{||\mathbf{r}(\tau) + \mathbf{r}_{em}(\tau)||^2}\right)$$

The system matrix is used to construct the relative state transition matrix (RSTM) to implement a shooting scheme to target relative states with respect to the target spacecraft. The advantage of targeting states in the LVLH frame L stems from the ability to obtain desired relative motion from the target's perspective.

CR3BP Relative Motion Equations

Similar to the formulation of the 3B-ENLERM and 3B-LERM, the assumptions from the employment of the CR3BP as the dynamical model for the Earth-Moon system dynamics simplifies a number of parameters such that

- $\boldsymbol{\omega}_{L/I} = \boldsymbol{\omega}_{L/M} + \boldsymbol{\omega}_{M/I}$

- $[\dot{\boldsymbol{\omega}}_{L/I}]_L = [\dot{\boldsymbol{\omega}}_{L/M}]_L - \boldsymbol{\omega}_{L/M} \times \hat{\mathbf{k}}$

- $\boldsymbol{\omega}_{L/M}$ is a function of the target acceleration $[\ddot{\mathbf{r}}]_M$ given in Equation (3.88)

- $\dot{\boldsymbol{\omega}}_{L/M}$ is a function of the target jerk $[\dddot{\mathbf{r}}]_M$ given in Equation (3.89)

The resulting equations are denoted as the three-body circular nonlinear equations of motion or 3B-CNLERM. If the linearization of the gravitational accelerations is taken into consideration, the equations are denoted the three-body circular linear equations of motion or 3B-CLERM.

3.4 Verification and Validation

Both the two-body and three-body relative equation models are tested and compared to characterize their accuracy in the 9:2 NRHO, the small DRO, and the large DRO. The truth model is taken as the 3B-ENLERM or the 3B-CNLERM, depending on the description of the Earth-Moon dynamics. The simulations are carried out in MATLAB using the ode113 differential solver with a absolute and relative tolerance of $10e - 12$. Moreover, the propagation time is set to 12 hours. Franzini et al. validated the equations of relative motion in a similar fashion in [4], however the relative position and velocity vectors were initiated independently and represent arbitrary perturbed states along the directions of the LVLH frame. This investigation initiates the relative state vector to characterize relative position and velocity combinations that accurately reflect placements along each of the reference orbits. Consequently, the obtained results are similar to Franzini et al [4], but they vary slightly due to the fact that both relative position and velocity states are initialized simultaneously. First, a definition for the mean anomaly is introduced to indicate the target along the reference orbit as

$$MA = 2\pi \frac{\tau}{P} \tag{3.99}$$

where τ is the time since perilune and P is the period of the corresponding reference orbit. Then, a series of chasers are placed behind and ahead of the target along the reference orbit and used to initialize a number of relative states for the simulation. Once these initial states are obtained, they are propagated with the 2B-HCW, 2B-LERM, and 3B-ELERM (or 3B-CLERM), respectively. Figure 3.2 presents a schematic of the validation scheme along the 9:2 NRHO. In this example, the target is placed at an initial mean anomaly along the NRHO and a number of fictitious chaser spacecraft are placed behind and ahead of the target's position along the NRHO. The relative states for each of the chaser spacecraft are computed and propagated with the different relative dynamical models for a TOF of 12 hours.
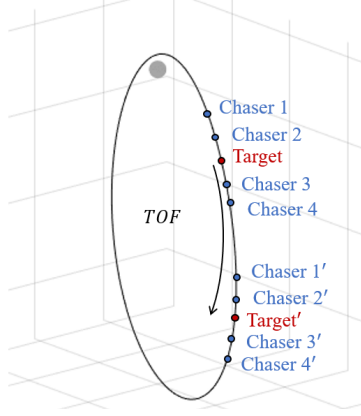
Fig. 3.2. Validation scheme along 9:2 NRHO

To compare the results obtained by the different models, a performance index is defined such that

$$e_p = \max_{\tau \in [0 \ \mathrm{TOF}]} ||\boldsymbol{\rho}(\tau) - \boldsymbol{\rho}^*(\tau)|| \quad , \quad e_v = \max_{\tau \in [0 \ \mathrm{TOF}]} ||\dot{\boldsymbol{\rho}}(\tau) - \dot{\boldsymbol{\rho}}^*(\tau)|| \qquad (3.100)$$

where e_p and e_v denote the maximum distance and speed errors over the time interval. Moreover, quantities with the star denote the true values whereas those without are obtained from the propagation using the selected dynamical model. In this investigation, the 9:2 NRHO and the Large DRO in both the CR3BP and ER3BP are used to compare the relative equations. In Figure 3.3, the x-axis of the plots indicate the target initial mean anomaly along the NRHO. The y-axis plots the initial relative distance of the chaser in km at the initial relative state. The plots convey configurations of the chaser both behind and ahead of the target, although there is no significant difference in results between the two cases. The color bar is intended to represent the common logarithm of the position or velocity error. For example, a color indicating a level of 3 indicates a position error of 1000 m. Similarly, a color indicating a level of 0 indicates a velocity error of 1 m/s. Figures 3.3 and 3.4 contain the error results in relative position and velocity for the 9:2 NRHO and Figures 3.5 and 3.6 for the Large DRO in the CR3BP and ER3BP, respectively.

CR3BP - 9:2 NRHO
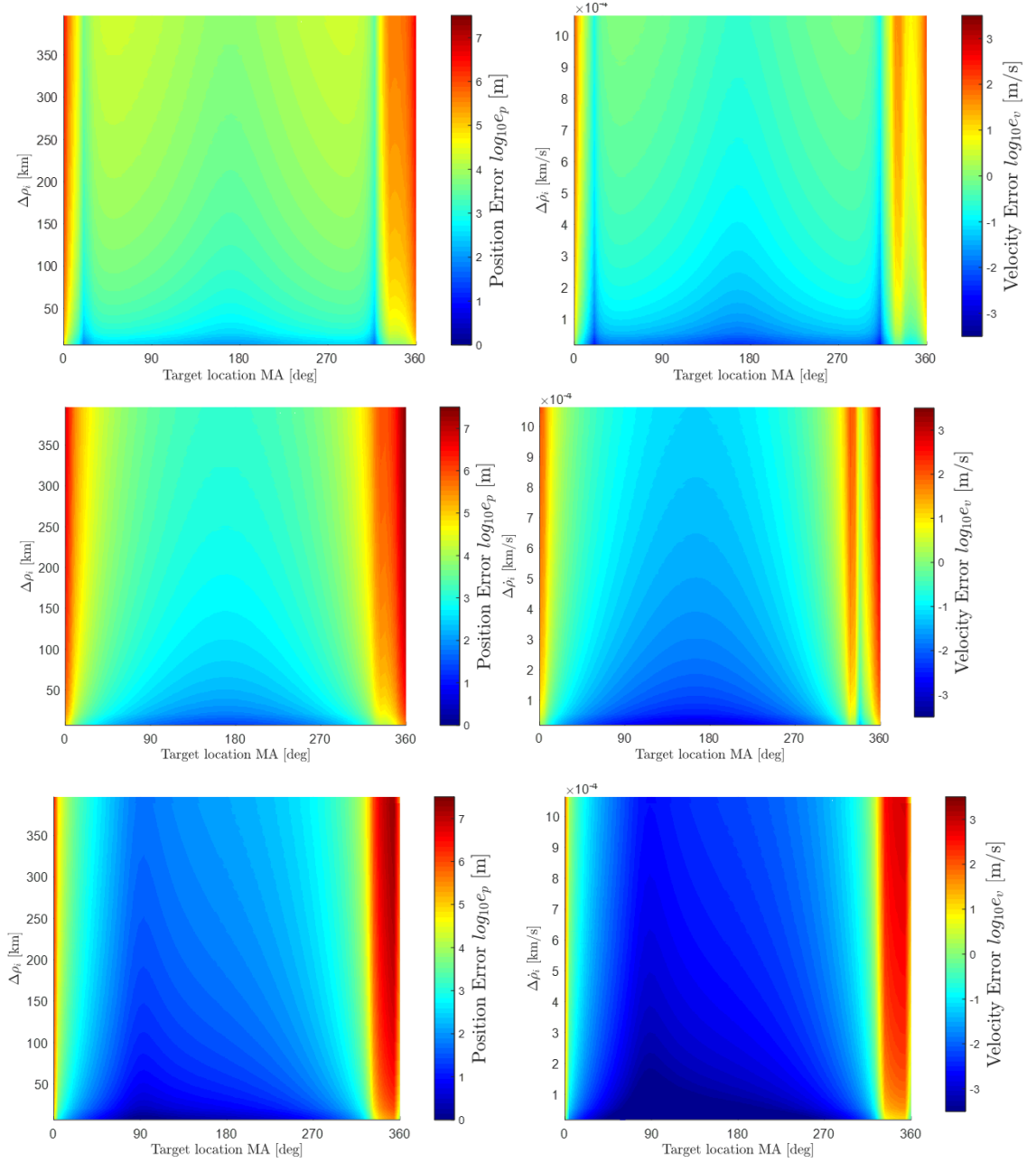
Fig. 3.3. Position and velocity error results after 12 hrs. for 2B-HCW (top), 2B-LERM (middle), and 3B-LERM (bottom) for the 9:2 NRHO in the CR3BP

ER3BP - 9:2 NRHO
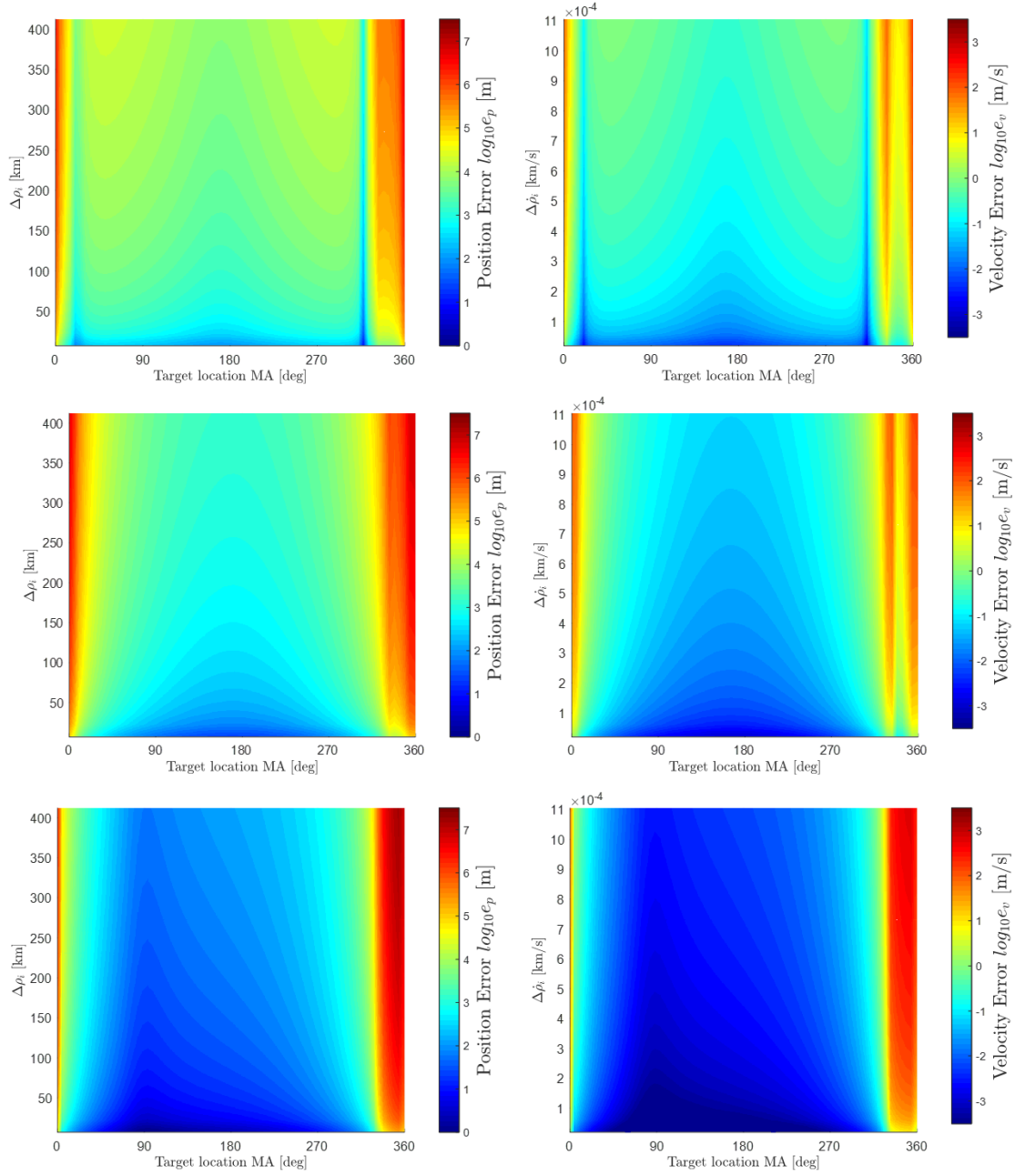
Fig. 3.4. Position and velocity error results after 12 hrs. for 2B-HCW (top), 2B-LERM (middle), and 3B-LERM (bottom) for the 9:2 NRHO in the ER3BP

CR3BP - Large DRO
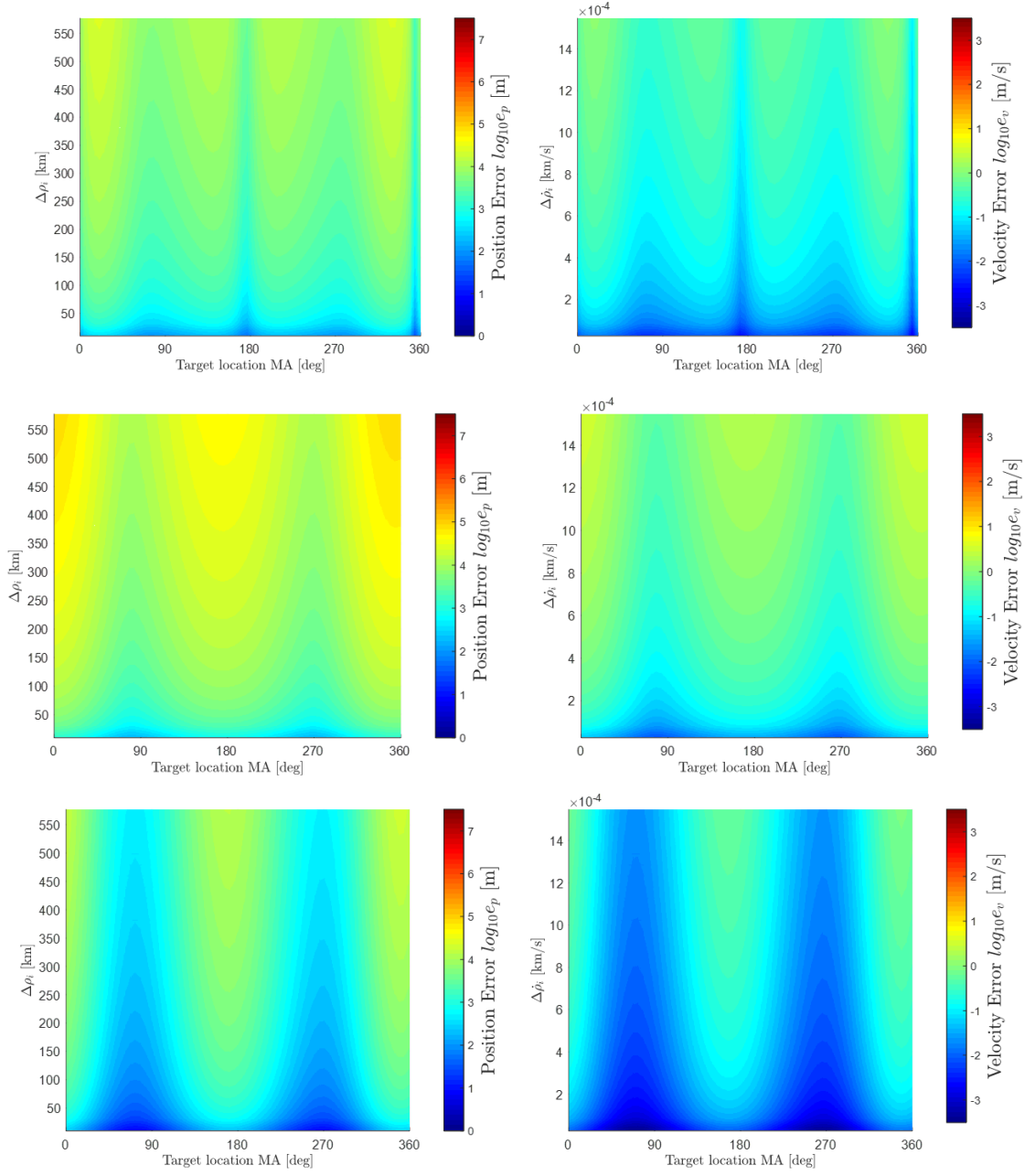
Fig. 3.5. Position and velocity error results for 2B-HCW (top), 2B-LERM (middle), and 3B-LERM (bottom) for the Large DRO in the CR3BP

ER3BP - Large DRO
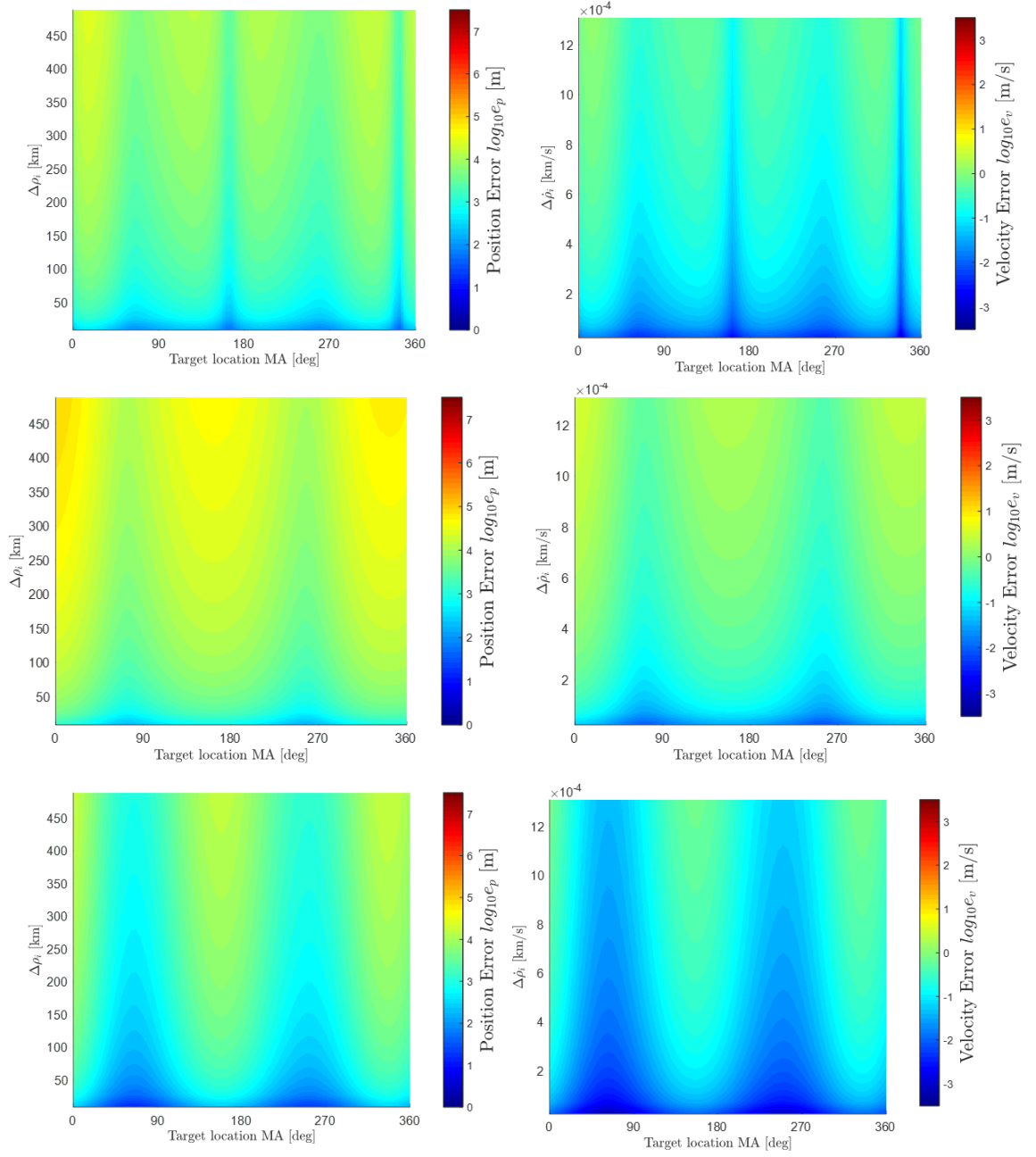
Fig. 3.6. Position and velocity error results for 2B-HCW (top), 2B-LERM (middle), and 3B-LERM (bottom) for the Large DRO in the ER3BP

A number of observations are in order. First, for both the 9:2 NRHO and the Large DRO, in both the CR3BP and ER3BP, the 3B-LERM outperform the 2B-HCW and 2B-LERM in the estimation of relative position and velocity for a 12 hour simulation time. For the 9:2 NRHO cases in Figures 3.3 and 3.4, the two body models generally perform better near apolune ($MA = 180°$) than anywhere else along the NRHO. This is due to the fact that relative velocities between the target and chaser are minimized at apolune. Since both the target and chaser reach their minimum velocity near apolune, the effect of the relative velocity between the spacecraft is reduced in the relative dynamics equations. Consequently, for a target initially near apolune, the 2B-HCW equations attain a 1-km position and 10 cm/s velocity error when the chaser and target are about 30 km apart on the reference orbit. Likewise, the 2B-LERM model performs slightly better where it attains a 1-km position and 10 cm/s velocity error at 150 km relative separation between the spacecraft when the target is near apolune. For the 3B-LERM, the results are more accurate at a larger distance yet they perform their best slightly before apolune. This would indicate that rendezvous maneuvers should take place near this region to obtain the best estimations of the relative states. Near perilune however, the 3B-LERM incur a significant amount of both position and velocity error. This is due to the fact that near perilune, the rapid separation between the chaser and target exceeds the domain of validity for the linearized assumption. Therefore, rendezvous maneuvers are not advised in regions near perilune for the NRHO. In the large DRO cases in Figures 3.5 and 3.6, the 2B-HCW equations actually perform better than the 2B-LERM. This is a surprising result since the 2B-LERM employ less assumptions in their formulation. Moreover, the 2B-HCW equations perform best near a $MA = 180°$, but the 2B-LERM are more accurate near $MA = 90°$ and $MA = 270°$, respectively. Note that a $MA = 180°$, the target is actually at another perilune due to the large DRO's shape. This is illustrated in Figure 3.7. Since regions near perilune are characterized by greater relative velocities between the spacecraft, two peaks are identified in the plot of the 2B-LERM for the large DRO indicating the target's encounter at the apolunes. The

same behavior is apparent in the 3B-LERM for the large DRO, yet they outperform the other two-body based models and attain a 1-km error in position when the target is at apolune and the initial relative distance between the spacecraft is about 550 km. Likewise, an initial relative velocity between the spacecraft exceeding 1 m/s leads to a velocity error of 1 cm/s for the 12 hour period near regions of apolune.
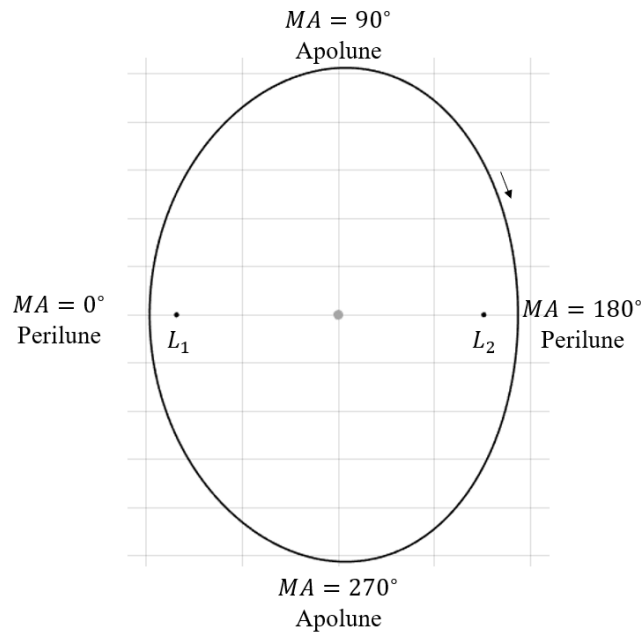
Fig. 3.7. Illustration of perilune and apolune points for the large DRO in CR3BP

Small DRO HCW Approximations

Similar analysis for the small DRO is performed characterizing a near circular reference orbit close to the Moon. The small DRO represents orbits where a majority of the gravitational influence is due to the second primary. Therefore, it is more useful to validate the 2B-HCW equations for the small DRO to determine the range of validity for the two-body assumption. Figure 3.8 plots the error profiles in relative position and velocity for the 2B-HCW model. As expected, the results are more uniform across the target mean anomaly where the model attains a 1 km position and

10 cm/s velocity error at a relative initial distance of 20 km between the spacecraft. Therefore, it can be concluded that the 2B-HCW equations may be used for the reference trajectory to provide a good initial guess to compute in the 3B-LERM. Nevertheless, it is important to consider that these results are only valid for within a 12-hour period.
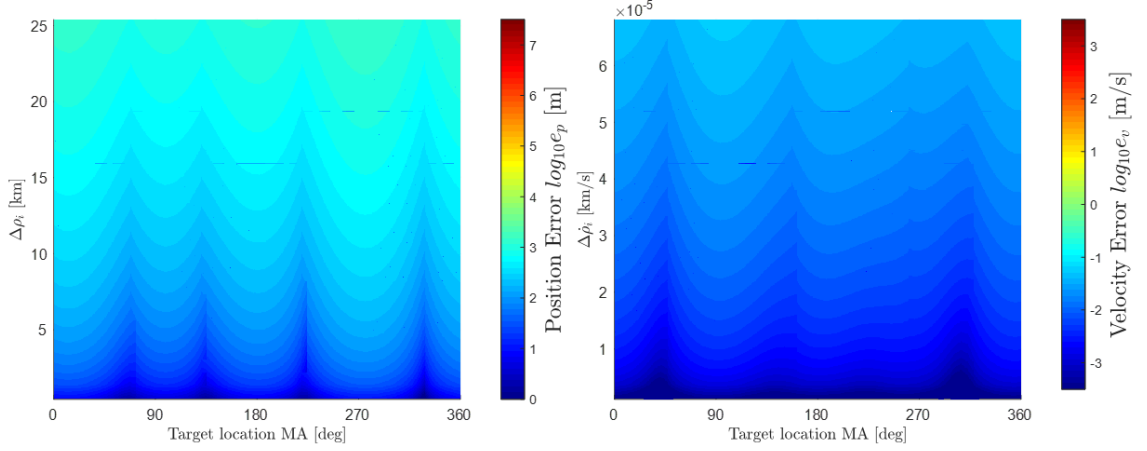
Fig. 3.8. Position and velocity error from the 2B-HCW model for a 12 hr period in the small DRO

3.5   Shooting Algorithms

In order to address rendezvous and spacecraft loitering problems, shooting algorithms are employed to target relative states in the LVLH frame L. Since the origin of frame L is the target, a chaser trajectory that reaches the origin indicates an interception with the target position. Similar to the construction of the single and multiple shooting schemes for targeting solutions in the CR3BP, the 3B-LERM and its associated system matrix is used to formulate the relative STM $(\mathbf{\Phi}_R)$ to assess the variations in the initial relative state to those downstream. The 3B-LERM are expressed in state-space form as

$$\dot{\mathbf{x}}(\tau) = \mathbf{A}(\tau)\mathbf{x}(\tau) + \mathbf{B}\mathbf{u}(\tau) \tag{3.101}$$

where

$$\mathbf{x}(\tau) = \begin{bmatrix} \boldsymbol{\rho}(\tau) \\ [\dot{\boldsymbol{\rho}}(\tau)]_L \end{bmatrix} \quad \text{and} \quad \mathbf{B} = \begin{bmatrix} \mathbf{0}_{3\times3} \\ \mathbf{I}_{3\times3} \end{bmatrix}$$

where the system matrix $\mathbf{A}(\tau)$ is defined as

$$\mathbf{A}(\tau) = \begin{bmatrix} \mathbf{0}_{3\times3} & \mathbf{I}_{3\times3} \\ \mathbf{A}_{\boldsymbol{\rho}\dot{\boldsymbol{\rho}}}(\tau) & -2\boldsymbol{\Omega}_{L/I}(\tau) \end{bmatrix} \tag{3.102}$$

and

$$\mathbf{A}_{\boldsymbol{\rho}\dot{\boldsymbol{\rho}}}(\tau) = -[\dot{\boldsymbol{\Omega}}_{L/I}(\tau)]_L - \boldsymbol{\Omega}_{L/I}(\tau)^2 - \frac{\mu}{r(\tau)^3}\left(\mathbf{I} - 3\frac{\mathbf{r}(\tau)\mathbf{r}(\tau)^T}{r(\tau)^2}\right)$$
$$+ \frac{1-\mu}{||\mathbf{r}(\tau) + \mathbf{r}_{em}(\tau)||^3}\left(\mathbf{I} - 3\frac{(\mathbf{r}(\tau) + \mathbf{r}_{em}(\tau))(\mathbf{r}(\tau) + \mathbf{r}_{em}(\tau))^T}{||\mathbf{r}(\tau) + \mathbf{r}_{em}(\tau)||^2}\right)$$

Since the state vector is comprised of relative states, the relative state transition matrix $\boldsymbol{\Phi}_R$ is defined as

$$\boldsymbol{\Phi}_R(\tau, \tau_0) = \frac{\partial \mathbf{x}(\tau)}{\partial \mathbf{x}(\tau_0)} = \begin{bmatrix} \frac{\partial x}{\partial x_0} & \frac{\partial x}{\partial y_0} & \frac{\partial x}{\partial z_0} & \frac{\partial x}{\partial x_0'} & \frac{\partial x}{\partial y_0'} & \frac{\partial x}{\partial z_0'} \\ \frac{\partial y}{\partial x_0} & \frac{\partial y}{\partial y_0} & \frac{\partial y}{\partial z_0} & \frac{\partial y}{\partial x_0'} & \frac{\partial y}{\partial y_0'} & \frac{\partial y}{\partial z_0'} \\ \frac{\partial z}{\partial x_0} & \frac{\partial z}{\partial y_0} & \frac{\partial z}{\partial z_0} & \frac{\partial z}{\partial x_0'} & \frac{\partial z}{\partial y_0'} & \frac{\partial z}{\partial z_0'} \\ \frac{\partial x'}{\partial x_0} & \frac{\partial x'}{\partial y_0} & \frac{\partial x'}{\partial z_0} & \frac{\partial x'}{\partial x_0'} & \frac{\partial x'}{\partial y_0'} & \frac{\partial x'}{\partial z_0'} \\ \frac{\partial y'}{\partial x_0} & \frac{\partial y'}{\partial y_0} & \frac{\partial y'}{\partial z_0} & \frac{\partial y'}{\partial x_0'} & \frac{\partial y'}{\partial y_0'} & \frac{\partial y'}{\partial z_0'} \\ \frac{\partial z'}{\partial x_0} & \frac{\partial z'}{\partial y_0} & \frac{\partial z'}{\partial z_0} & \frac{\partial z'}{\partial x_0'} & \frac{\partial z'}{\partial y_0'} & \frac{\partial z'}{\partial z_0'} \end{bmatrix} = \begin{bmatrix} \phi_{R,11} & \phi_{R,12} & \phi_{R,13} & \phi_{R,14} & \phi_{R,15} & \phi_{R,16} \\ \phi_{R,21} & \phi_{R,22} & \phi_{R,23} & \phi_{R,24} & \phi_{R,25} & \phi_{R,26} \\ \phi_{R,31} & \phi_{R,32} & \phi_{R,33} & \phi_{R,34} & \phi_{R,35} & \phi_{R,36} \\ \phi_{R,41} & \phi_{R,42} & \phi_{R,43} & \phi_{R,44} & \phi_{R,45} & \phi_{R,46} \\ \phi_{R,51} & \phi_{R,52} & \phi_{R,53} & \phi_{R,54} & \phi_{R,55} & \phi_{R,56} \\ \phi_{R,61} & \phi_{R,62} & \phi_{R,63} & \phi_{R,64} & \phi_{R,65} & \phi_{R,66} \end{bmatrix} \tag{3.103}$$

Moreover, the first-order matrix differential equation governing the relative STM evolution in time is

$$\boldsymbol{\Phi}_R'(\tau, \tau_0) = \mathbf{A}(\tau)\boldsymbol{\Phi}_R(\tau, \tau_0) \tag{3.104}$$

where $\mathbf{A}(\tau)$ is the relative system matrix defined in Equation (3.102). The advantage of this formulation stems from the fact that the same computational techniques formulated for obtaining solutions in the CR3BP and ER3BP are employed to find solutions in the LVLH frame L. Since the 3B-LERM demonstrate better accuracy in the reference orbits compared to the two-body relative models, the system matrix for these equations will be used to obtain relative information and solutions for rendezvous and spacecraft loitering problems.

4. APPLICATIONS

A number of applications are considered using the three-body linear relative equations of motion or 3B-LERM. The first application is orbital rendezvous between the target and chaser within a specified time interval. Initial relative positions of the chaser with respect to the target are considered as close as 300 m and as far as 1000 km along the 9:2 NRHO, small DRO, and large DRO. Impulsive maneuvers are assumed to obtain the changes in velocity (Δv) needed to first, insert along a rendezvous trajectory and finally, eliminate any excess velocity at the interception point. Configurations where the chaser is ahead and behind the target at some initial time are considered. Reference orbits for both the CR3BP and ER3BP are considered and they are compared regarding the overall Δv required to achieve terminal rendezvous. Although the reference orbits in both the CR3BP and ER3BP are slightly different and don't necessarily warrant a 1:1 comparison, the orbit geometry for both dynamical regimes possess similar characteristics. The main objective of the comparison is to understand the degree to which the Moon's eccentricity affects the differences in solutions between each dynamical regime. Summary tables detailing each rendezvous configuration, the model employed, and the total Δvs required are generated for each reference orbit.

The spacecraft loitering problem is investigated along two avenues, the first being natural loitering and the second described as forced loitering. As the name suggests, natural loitering produces bounded relative motion in the LVLH frame L with respect to the target without the execution of chaser maneuvers. On the contrary, forced loitering involves the implementation of multiple maneuvers to obtain a specified relative geometry. Spacecraft loitering geometries as close as 300 m and as far as 1000 km between the spacecraft are examined. Finally, scenarios comprised of both spacecraft loitering and orbital rendezvous are investigated.

4.1   Orbital Rendezvous

In each rendezvous example, two plots will be provided. The first plot on the left will indicate the target initial position along the NRHO represented by the value of the mean anomaly MA. The blue and red circles denote the starting positions of the chaser and target, respectively. The red star denotes the final position of the target. The red line depicts the path of the target along the reference orbit and the blue line is the rendezvous trajectory the chaser takes to intercept the target. The plot on the right presents depicts the relative dynamics in LVLH frame L. The origin of the LVLH frame is defined as the target and will be indicated by the red star. The arrows depict the direction of motion. In each of the reference orbits, the eccentricity of the system is included in the plots to indicate the employed dynamical model with $e = 0$ representing the CR3BP and $e = 0.0549$ representing the ER3BP. Since the analysis of the relative equations of motion indicate that the 3B-LERM are most accurate in regions near apolune, the initial mean anomalies of the target are set to include regions near apolune. Figures 4.2 - 4.7 plot rendezvous scenarios in the CR3BP 9:2 NRHO and Figures 4.8 - 4.13 plot those in the ER3BP 9:2 NRHO. Likewise, rendezvous scenarios are plotted for the CR3BP Small DRO and ER3BP Small DRO in Figures 4.14 - 4.19 and 4.20- 4.25, respectively. Finally rendezvous scenarios are plotted for the CR3BP Large DRO and ER3BP Large DRO in Figures 4.26 - 4.31 and 4.32- 4.33, respectively.
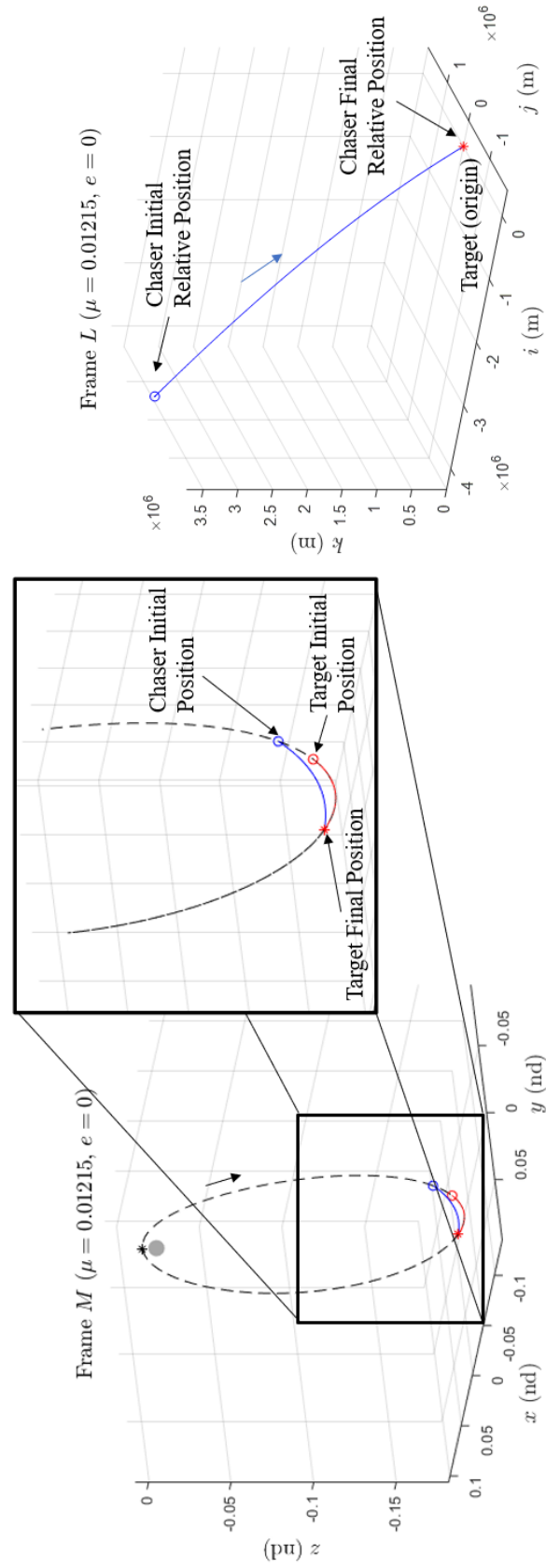
Fig. 4.1. Rendezvous schematic in the 9:2 NRHO

Rendezvous in 9:2 NRHO - CR3BP
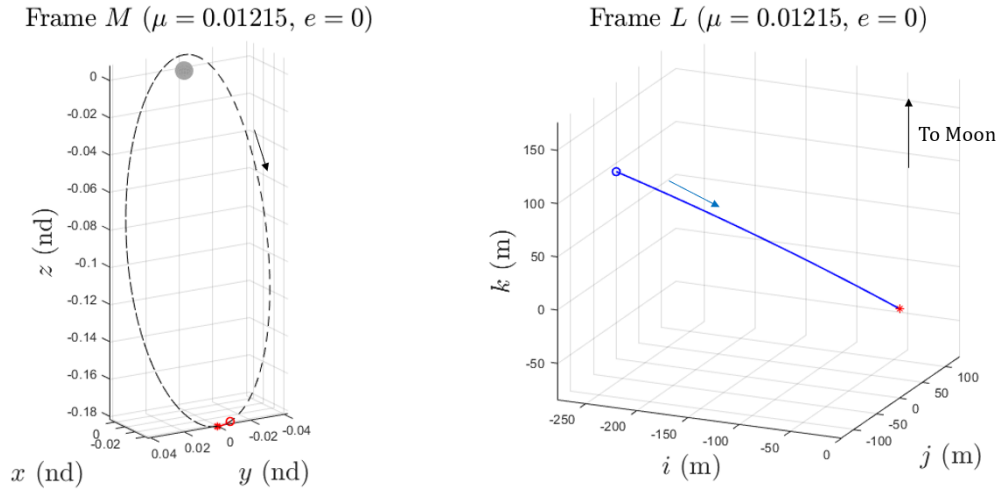
Fig. 4.2. 9:2 NRHO: target $MA = 162°$, 300 m (behind target)
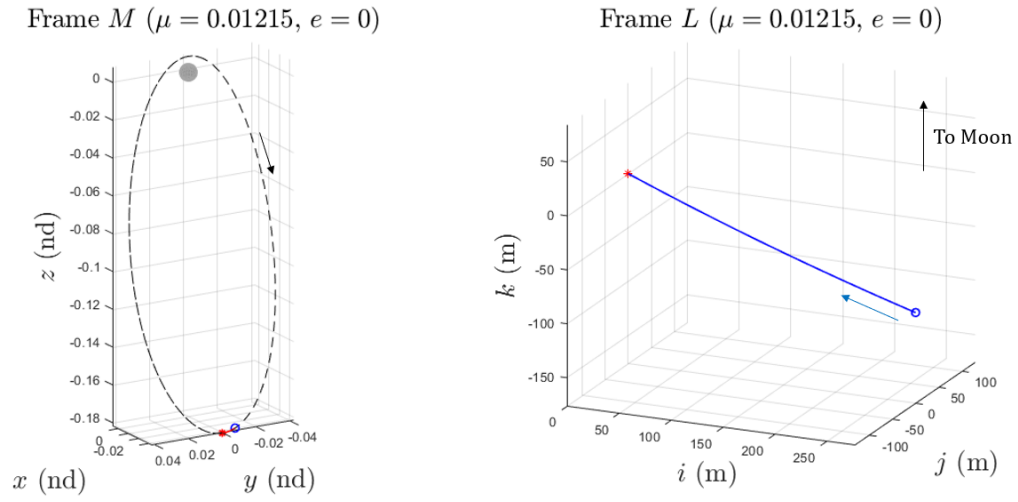
Fig. 4.3. 9:2 NRHO: target $MA = 162°$, 300 m (ahead target)
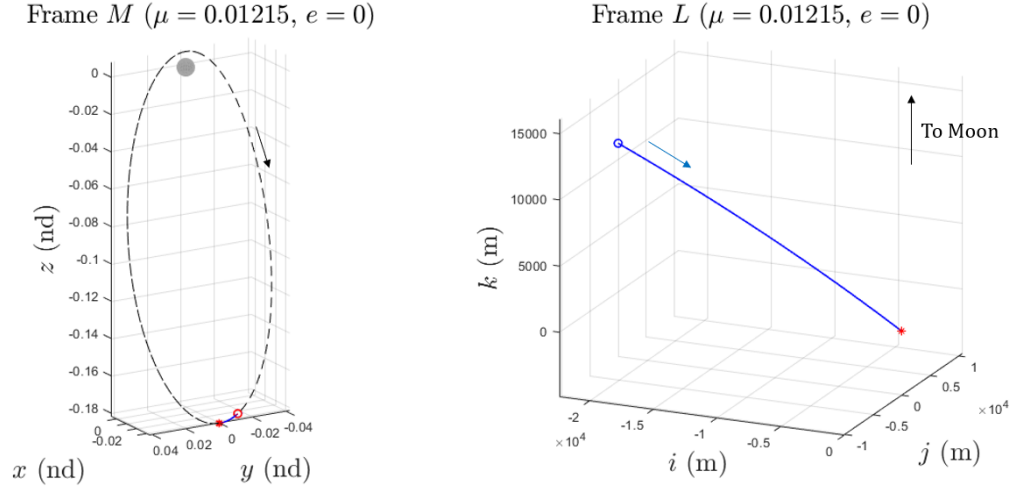
Fig. 4.4. 9:2 NRHO: target $MA = 153°$, 25 km (behind target)
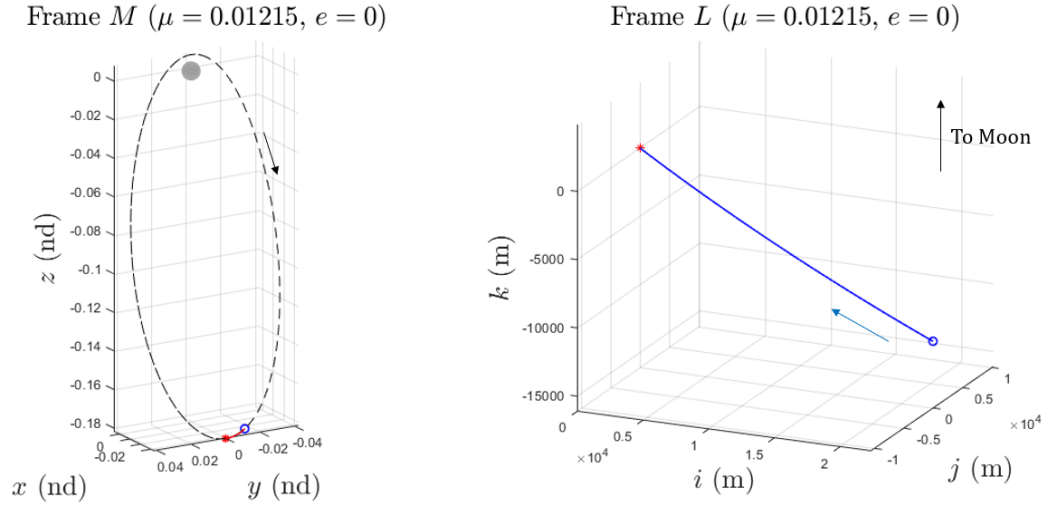
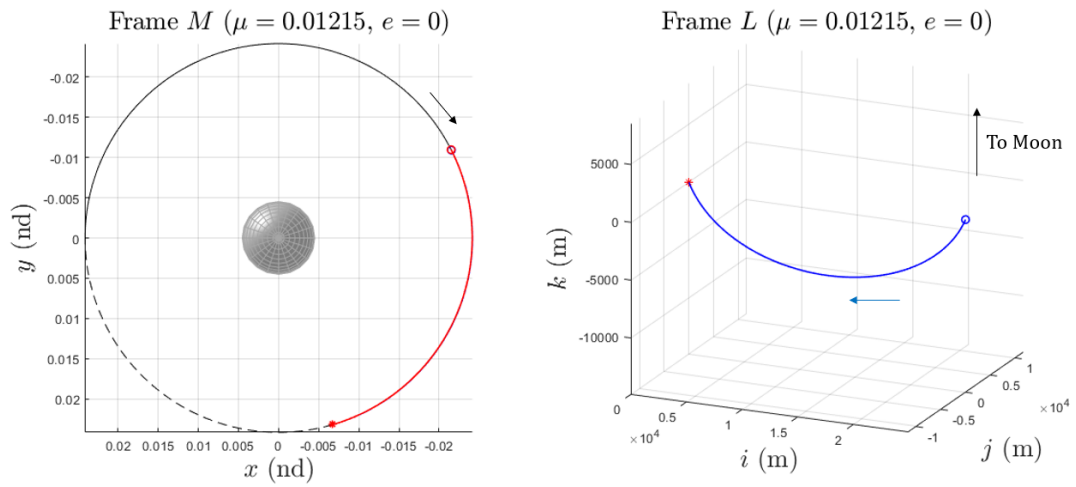Fig. 4.5. 9:2 NRHO: target $MA = 153°$, 25 km (ahead target)
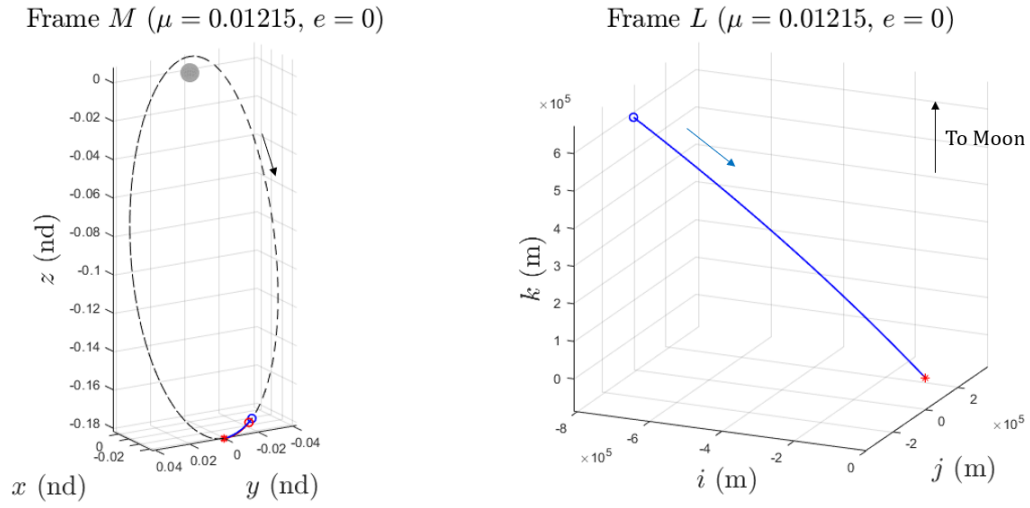
Fig. 4.6. 9:2 NRHO: target $MA = 144°$, 1000 km (behind target)
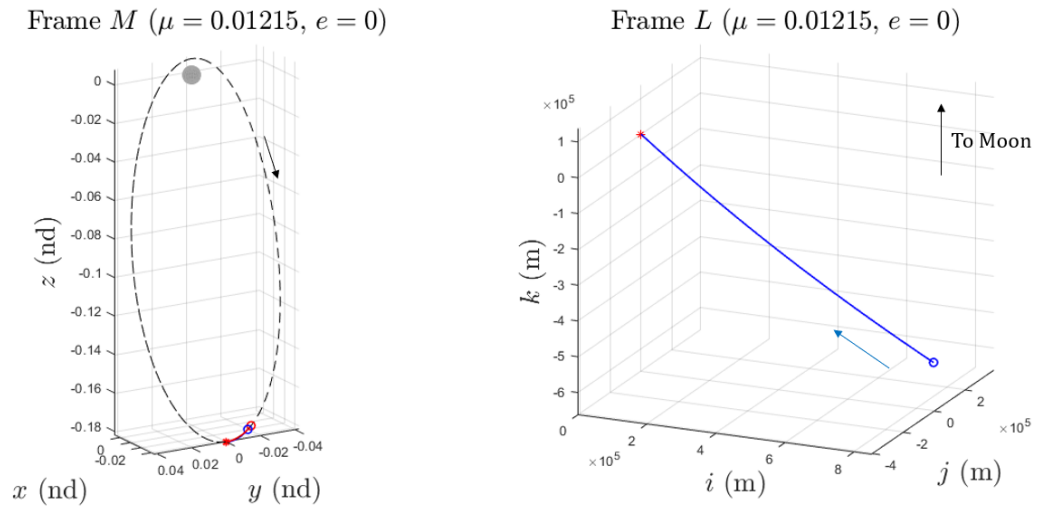
Fig. 4.7. 9:2 NRHO: target $MA = 144°$, 1000 km (ahead target)

Rendezvous in 9:2 NRHO - ER3BP

Fig. 4.8. 9:2 NRHO: target $MA = 162°$, 300 m (behind target)

Fig. 4.9. 9:2 NRHO: target $MA = 162°$, 300 m (ahead target)

Fig. 4.10. 9:2 NRHO: target $MA = 153°$, 25 km (behind target)

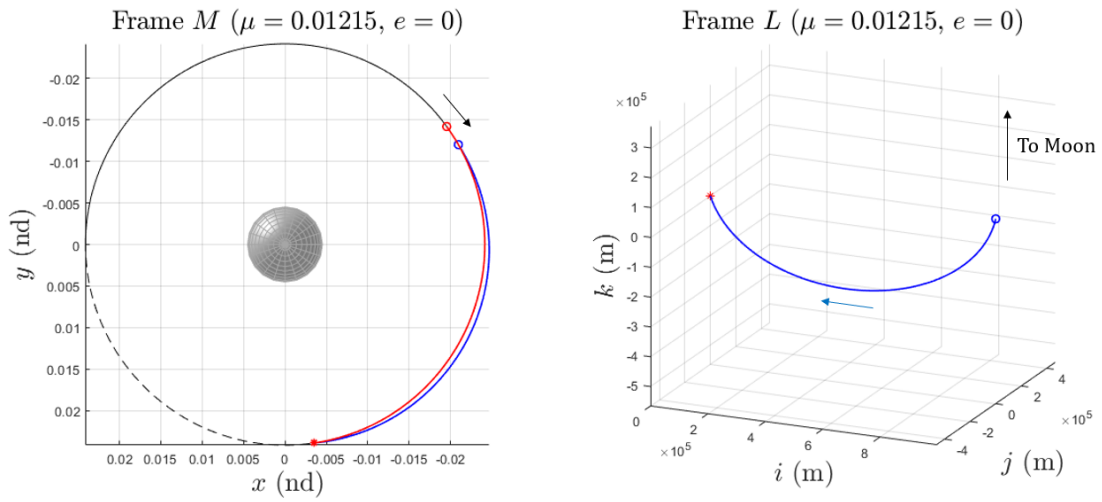Fig. 4.11. 9:2 NRHO: target $MA = 153°$, 25 km (ahead target)

Frame M ($\mu = 0.01215$, $e = 0.0549$)   Frame L ($\mu = 0.01215$, $e = 0.0549$)
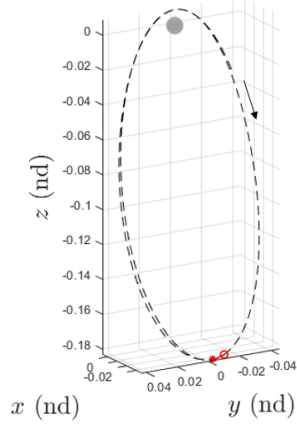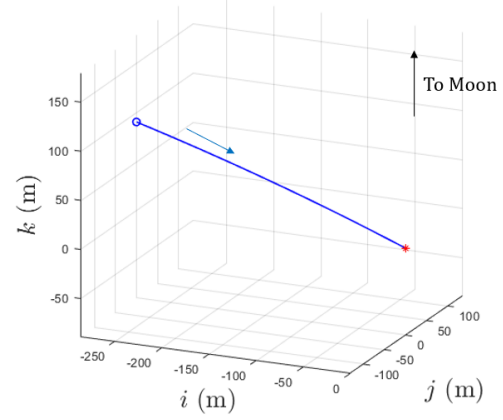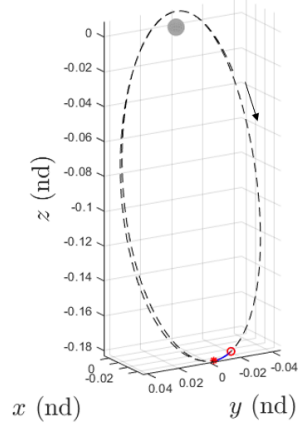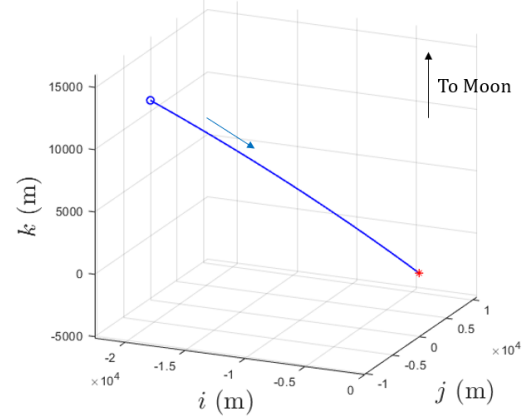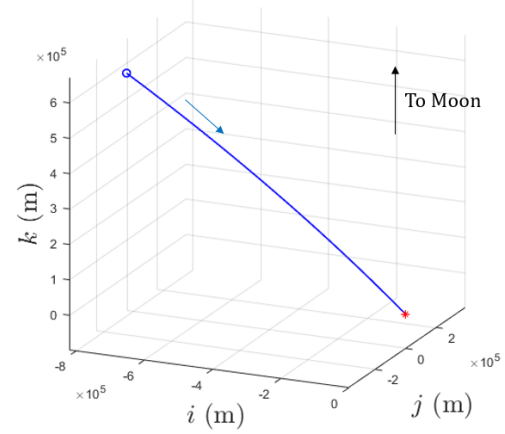
Fig. 4.12. 9:2 NRHO: target $MA = 144°$, 1000 km (behind target)
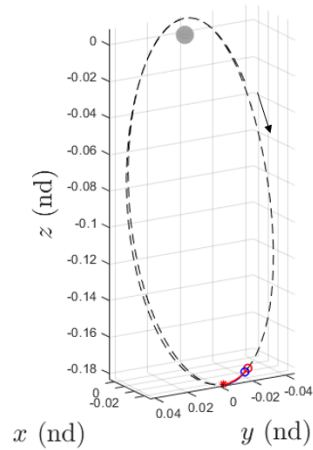
Frame M ($\mu = 0.01215$, $e = 0.0549$)   Frame L ($\mu = 0.01215$, $e = 0.0549$)
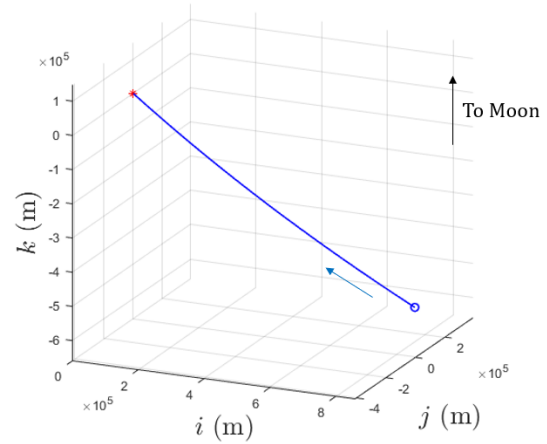
Fig. 4.13. 9:2 NRHO: target $MA = 144°$, 1000 km (ahead target)

Rendezvous in 9:2 NRHO -Results

<div align="center">

Table 4.1.
9:2 NRHO Rendezvous Maneuver Results

</div>

Reference Orbit	Model	Δv_1 [m/s]	Δv_2 [m/s]	Δv_{tot} [m/s]
9:2 NRHO, Figures 4.2 & 4.8	CR3BP	0.01	0.01	0.02
300 m - Behind, TOF: 8 hrs.	ER3BP	0.01	0.01	0.02
9:2 NRHO, Figures 4.3 & 4.9	CR3BP	0.01	0.01	0.02
300 m - Ahead, TOF: 8 hrs.	ER3BP	0.01	0.01	0.02
9:2 NRHO, Figures 4.4 & 4.10	CR3BP	0.517	0.581	1.098
25 km - Behind, TOF: 12 hrs.	ER3BP	0.520	0.581	1.101
9:2 NRHO, Figures 4.5 & 4.11	CR3BP	0.517	0.581	1.098
25 km - Ahead, TOF: 12 hrs.	ER3BP	0.520	0.580	1.101
9:2 NRHO, Figures 4.6 & 4.12	CR3BP	14.062	17.401	31.463
1000 km - Behind, TOF: 16 hrs.	ER3BP	14.216	17.405	31.621
9:2 NRHO, Figures 4.7 & 4.13	CR3BP	14.769	17.429	32.198
1000 km - Ahead, TOF: 16 hrs.	ER3BP	14.885	17.432	32.316

From the results of the rendezvous scenarios in the 9:2 NRHO, it is observed that the differences between the CR3BP and ER3BP models are more evident in scenarios involving a larger initial distance between the target and chaser. This is due partly to the fact that slight differences in the reference geometries between the CR3BP and ER3BP are more apparent on scales involving larger distances, however, the magnitude of the Δv maneuvers only vary on the order of centimeters per second in velocity. Moreover, configurations involving the chaser ahead of the target indicate that there are slight increases in the Δv required to achieve terminal rendezvous. This difference, although slight, arises from the fact that the chaser thrusts in the anti-velocity direction in order to the slow down to intercept the target.

Rendezvous in Small DRO - CR3BP
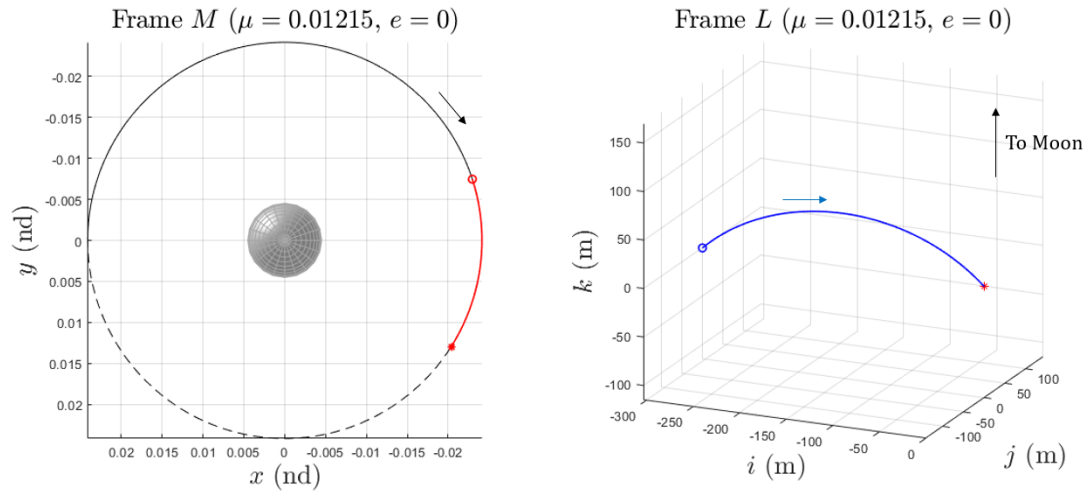
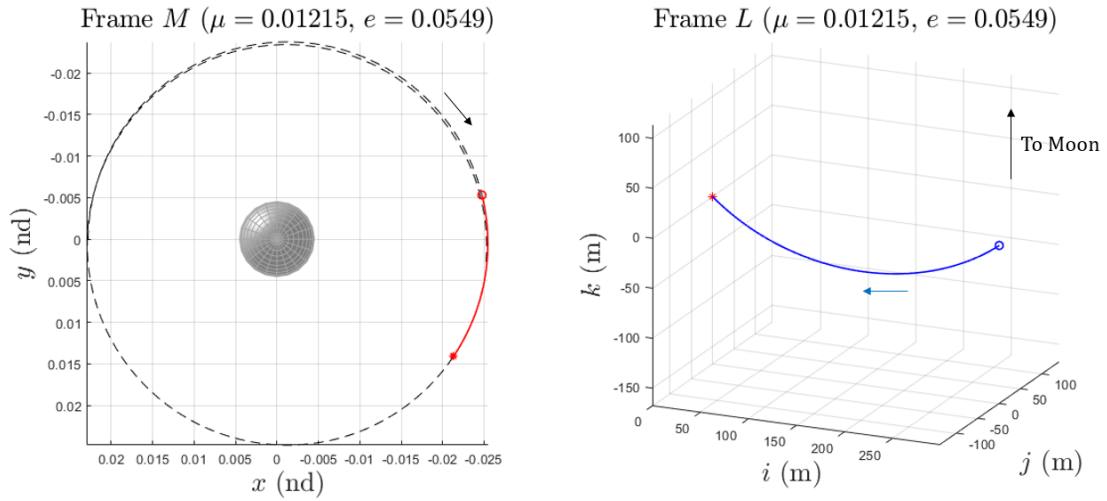Fig. 4.14. Small DRO: target $MA = 162°$, 300 m (behind target)
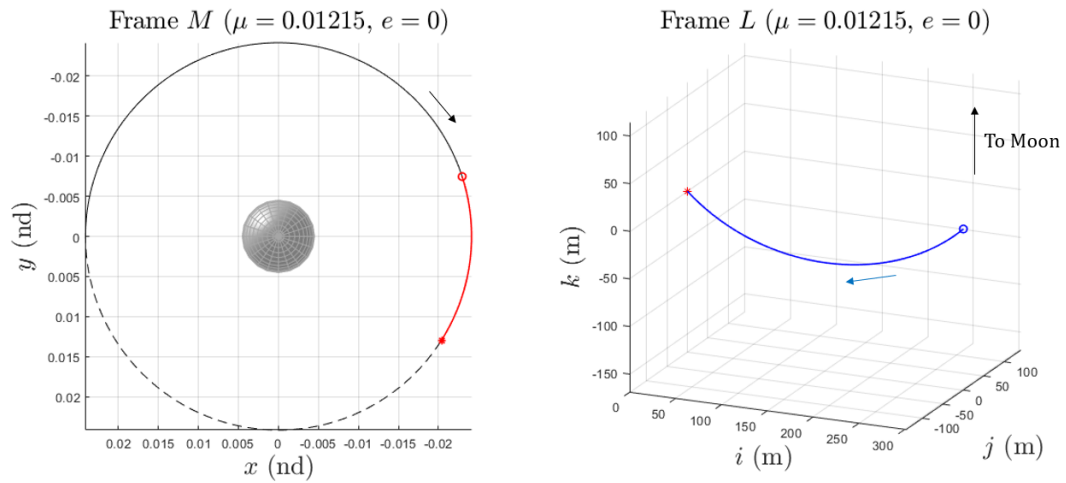
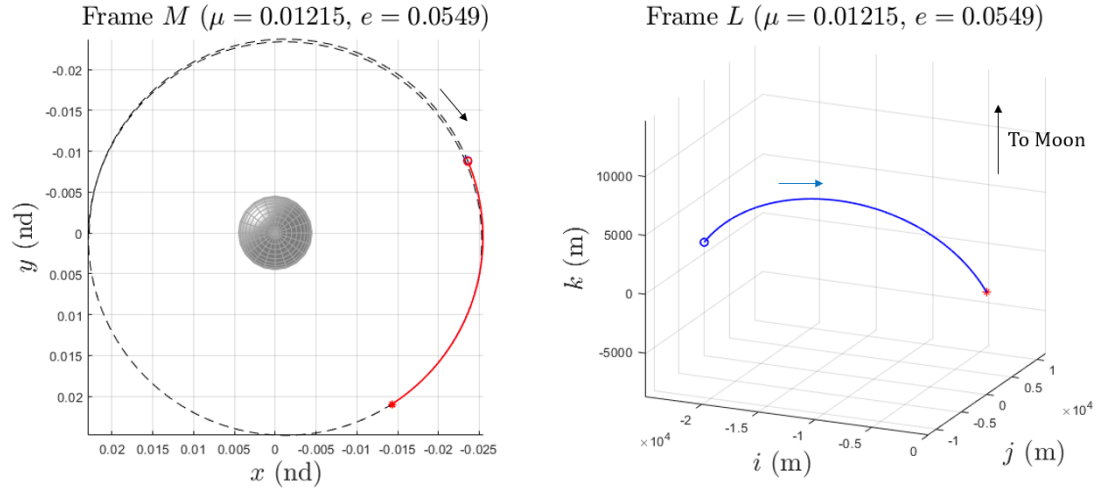Fig. 4.15. Small DRO: target $MA = 162°$, 300 m (ahead target)
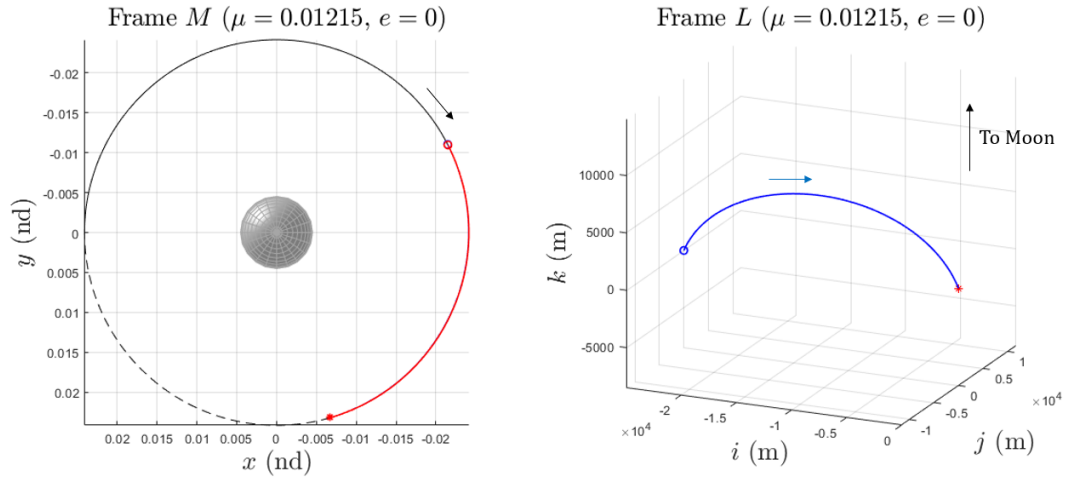
Fig. 4.16. Small DRO: target $MA = 153°$, 25 km (behind target)

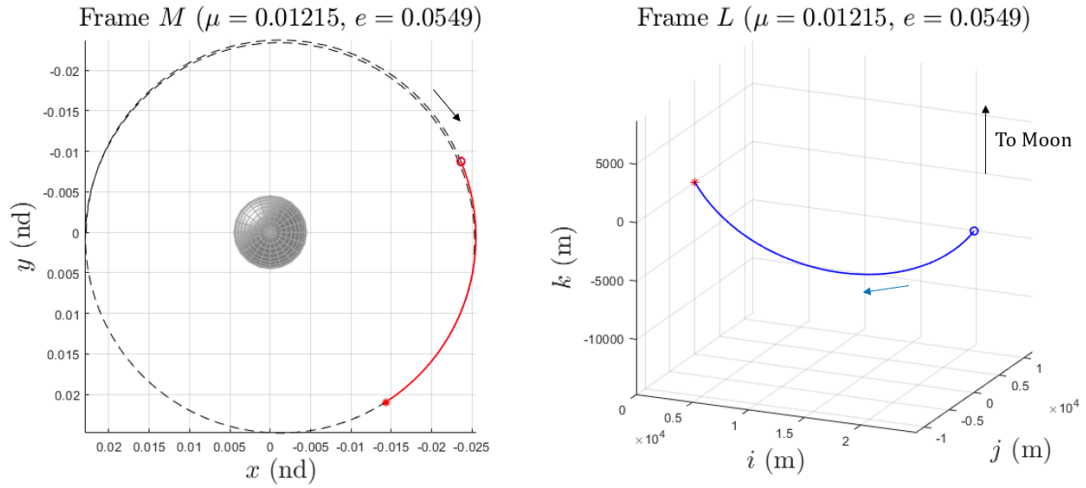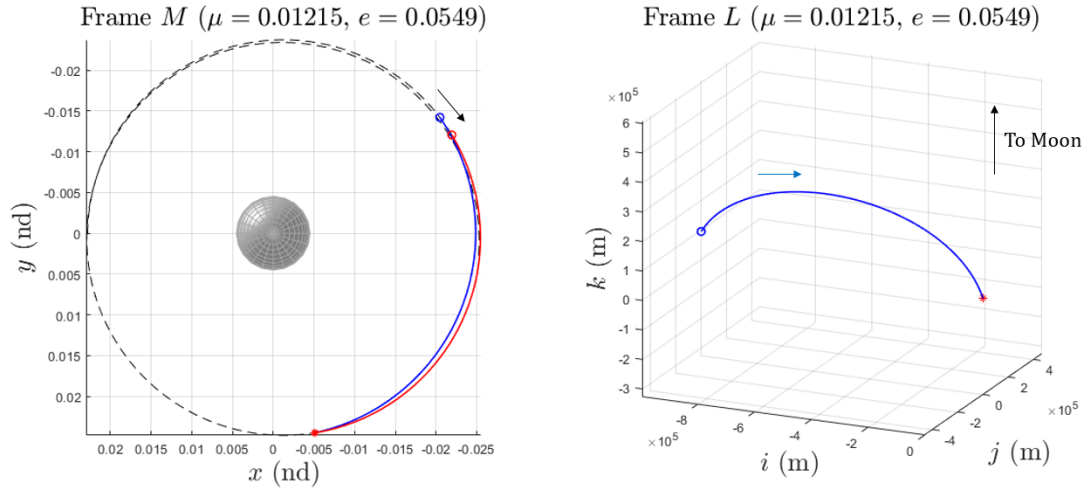Fig. 4.17. Small DRO: target $MA = 153°$, 25 km (ahead target)
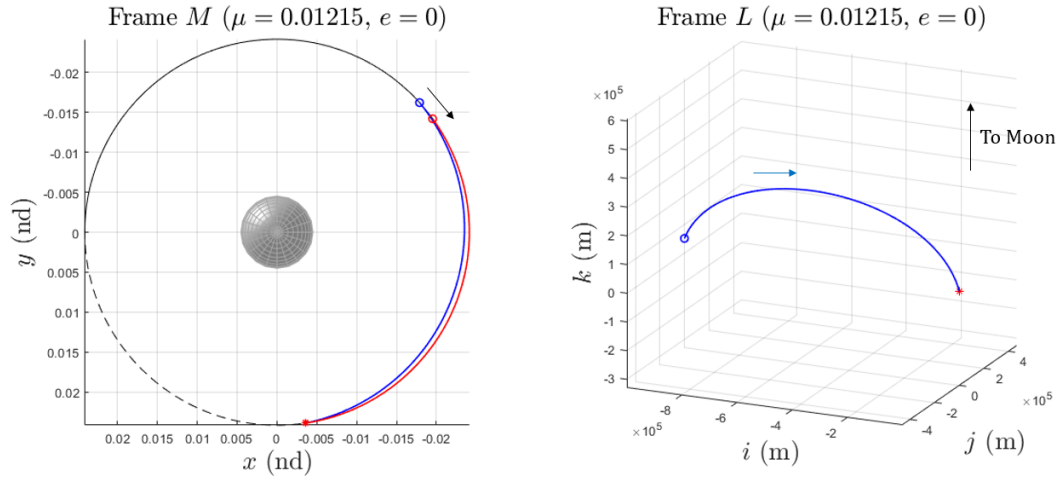
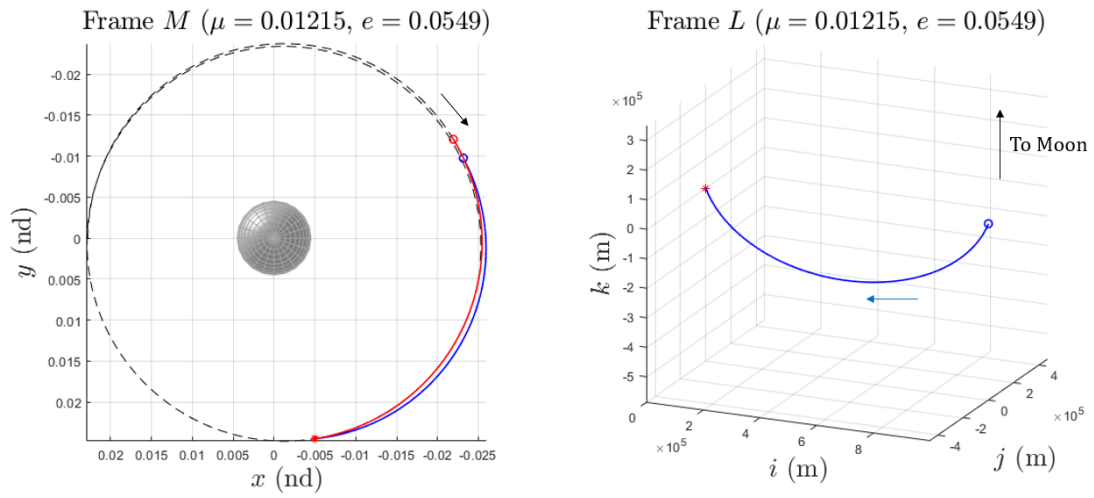Fig. 4.18. Small DRO: target $MA = 144°$, 1000 km (behind target)

Fig. 4.19. Small DRO: target $MA = 144°$, 1000 km (ahead target)

Rendezvous in Small DRO - ER3BP
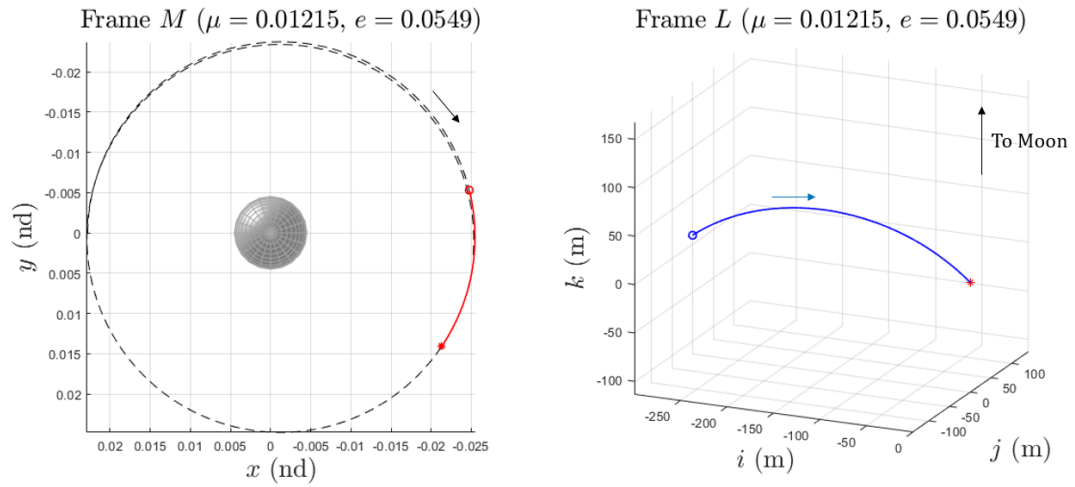
Fig. 4.20. Small DRO: target $MA = 162°$, 300 m (behind target)

Fig. 4.21. Small DRO: target $MA = 162°$, 300 m (ahead target)

Fig. 4.22. Small DRO: target $MA = 153°$, 25 km (behind target)

Fig. 4.23. Small DRO: target $MA = 153°$, 25 km (ahead target)

Fig. 4.24. Small DRO: target $MA = 144°$, 1000 km (behind target)

Fig. 4.25. Small DRO: target $MA = 144°$, 1000 km (ahead target)

Rendezvous in Small DRO -Results

<div align="center">

Table 4.2.
Small DRO Rendezvous Maneuver Results

</div>

Reference Orbit	Model	Δv_1 [m/s]	Δv_2 [m/s]	Δv_{tot} [m/s]
Small DRO, Figures 4.14 & 4.20	CR3BP	0.030	0.030	0.060
300 m - Behind, TOF: 3 hrs.	ER3BP	0.029	0.030	0.059
Small DRO, Figures 4.15 & 4.21	CR3BP	0.030	0.030	0.060
300 m - Ahead, TOF: 3 hrs.	ER3BP	0.029	0.030	0.059
Small DRO, Figures 4.16 & 4.22	CR3BP	1.217	1.22	2.437
25 km - Behind, TOF: 5 hrs.	ER3BP	1.489	1.494	2.982
Small DRO, Figures 4.17 & 4.23	CR3BP	1.218	1.221	2.439
25 km - Ahead, TOF: 5 hrs.	ER3BP	1.489	1.495	2.983
Small DRO, Figures 4.18 & 4.24	CR3BP	39.407	39.539	78.946
1000 km - Behind, TOF: 7 hrs.	ER3BP	39.672	39.857	79.529
Small DRO, Figures 4.19 & 4.25	CR3BP	41.074	41.239	82.313
1000 km - Ahead, TOF: 7 hrs.	ER3BP	41.335	41.523	82.857

From the resulting data of rendezvous scenarios in the small DRO, the same conclusions are reached regarding the slight differences in the Δvs required between the CR3BP and ER3BP reference orbits. Variations in the rendezvous solutions are more apparent with greater initial relative distances between the target and chaser. Differences in the total Δvs required to execute the rendezvous maneuvers vary on the order of tens of centimeters per second. Nevertheless, targeting schemes utilizing relative quantities stemming from the 3B-LERM converge to a chaser rendezvous trajectory that successfully intercepts the target in the LVLH frame L and Moon frame M.

Rendezvous in Large DRO - CR3BP
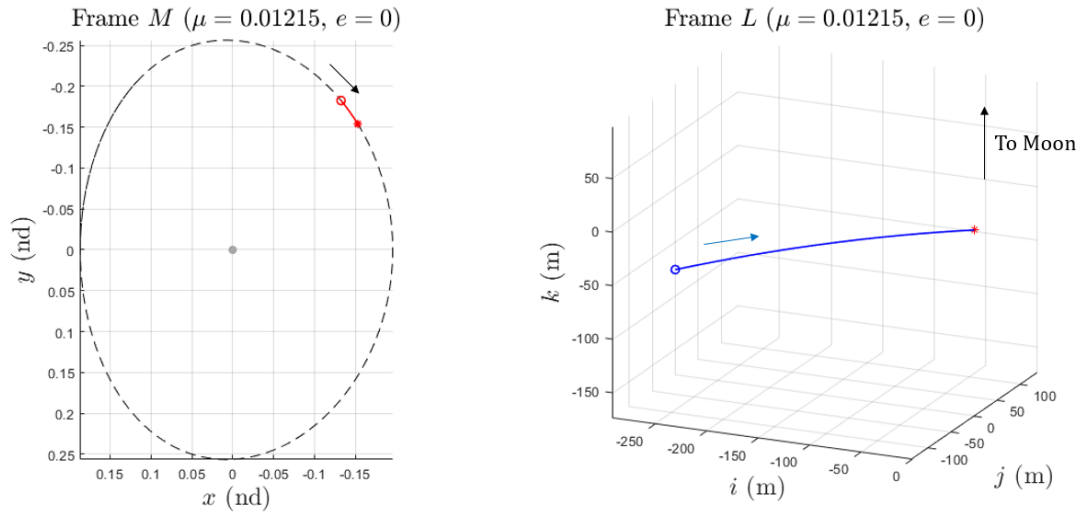
Fig. 4.26. Large DRO: target $MA = 135°$, 300 m (behind target)
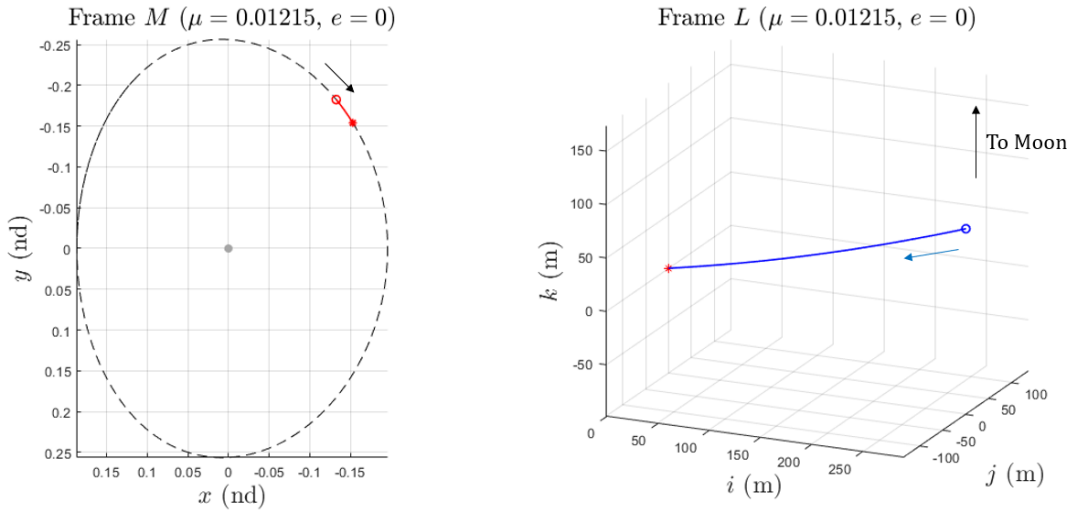
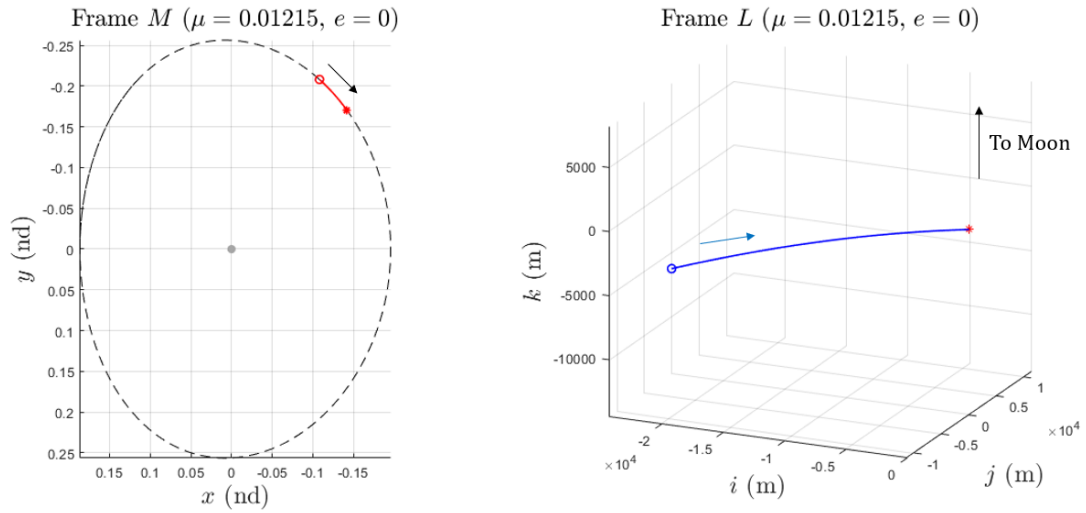
Fig. 4.27. Large DRO: target $MA = 135°$, 300 m (ahead target)

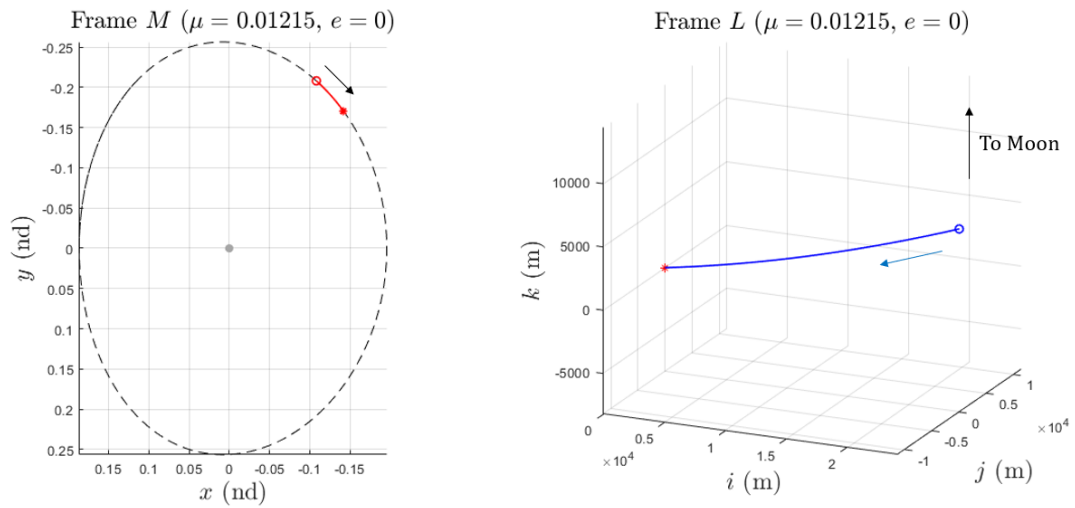Fig. 4.28. Large DRO: target $MA = 126°$, 25 km (behind target)

Fig. 4.29. Large DRO: target $MA = 126°$, 25 km (ahead target)

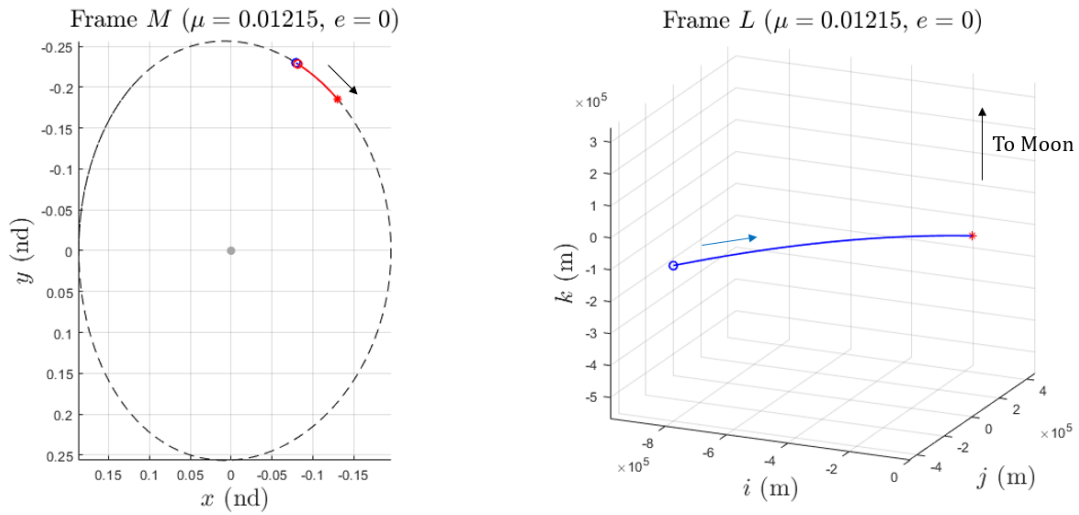Fig. 4.30. Small DRO: target $MA = 117°$, 1000 km (behind target)

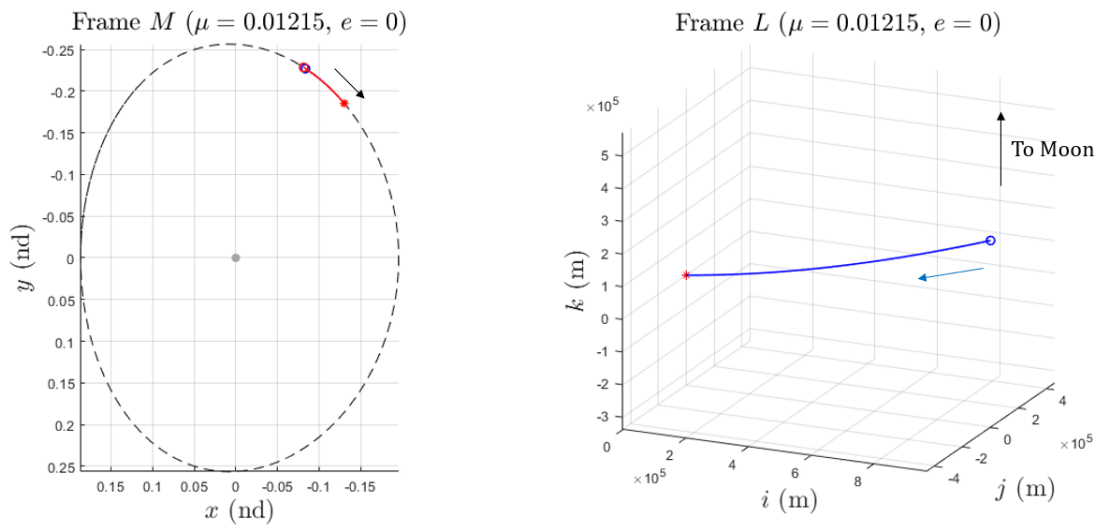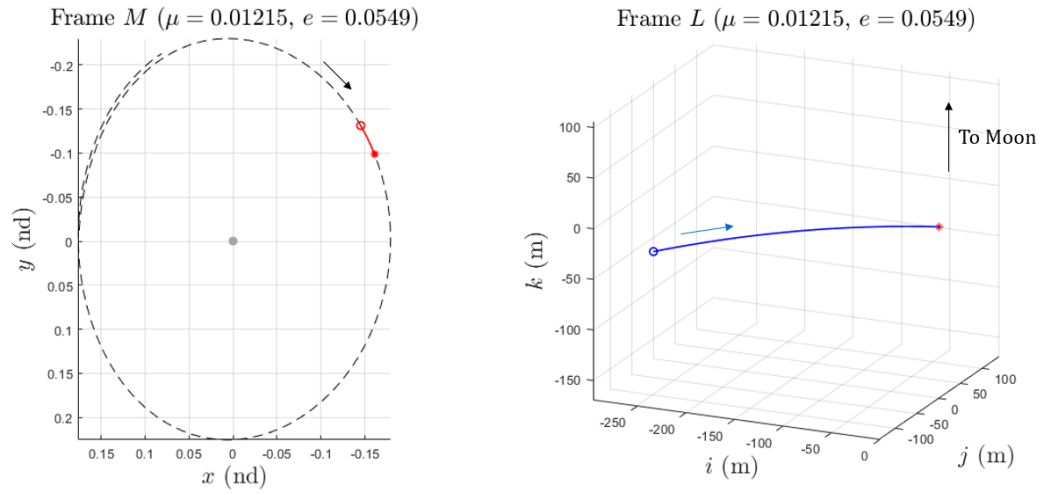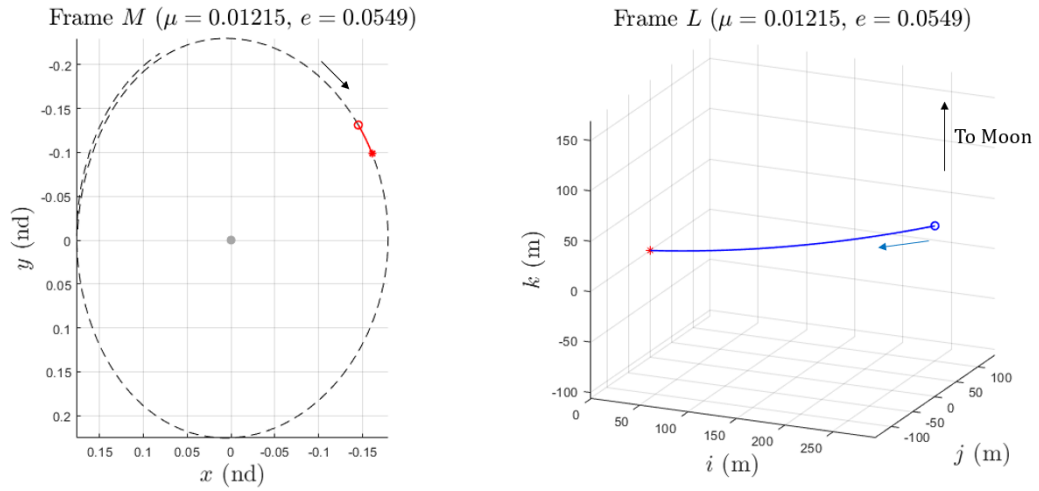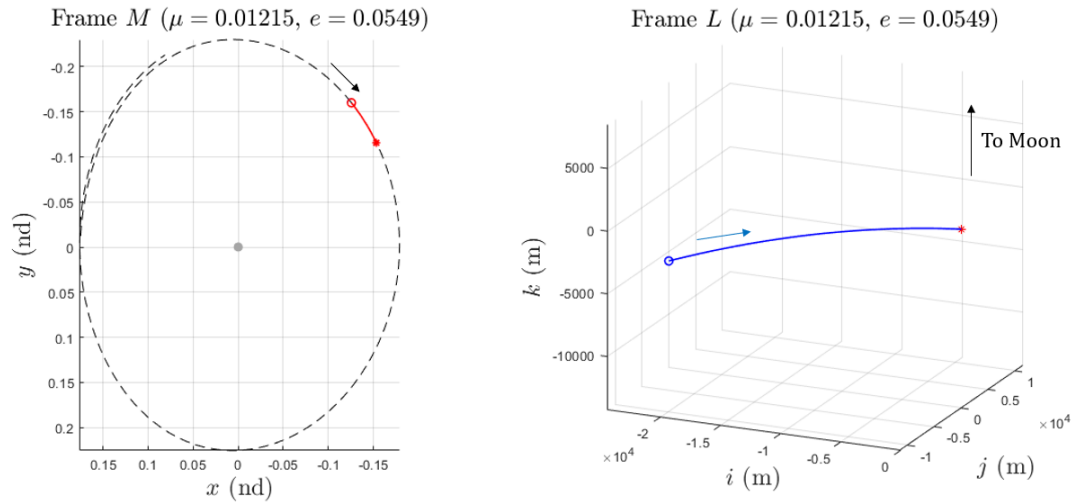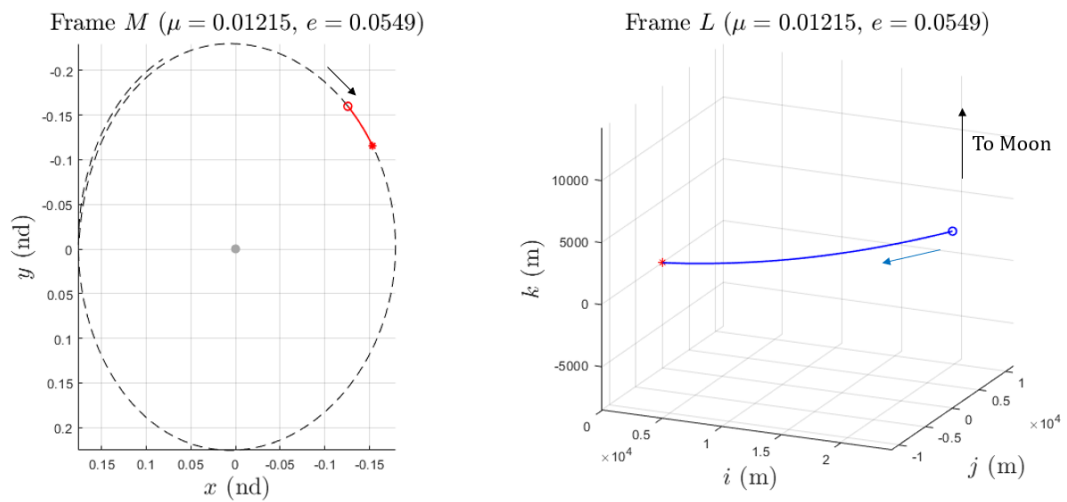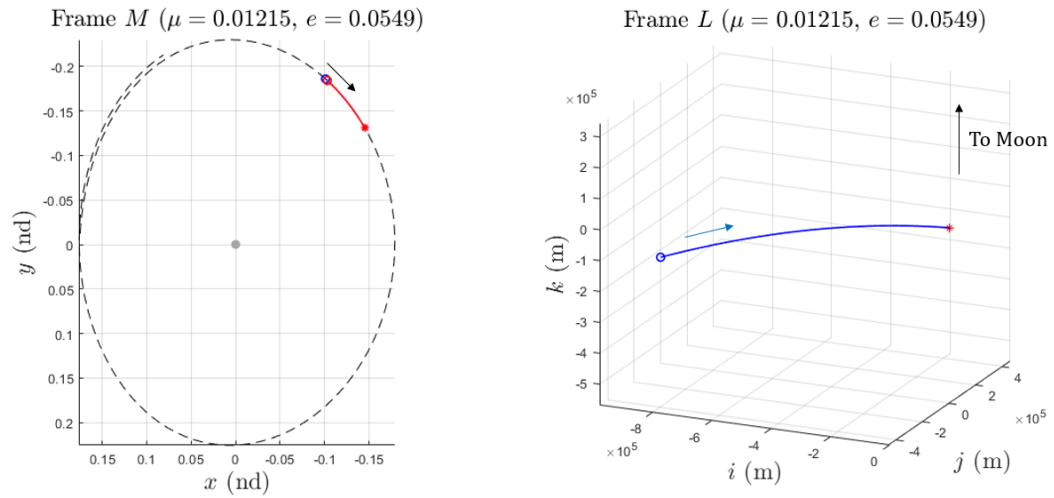Fig. 4.31. Small DRO: target $MA = 117°$, 1000 km (ahead target)

Rendezvous in Large DRO - ER3BP

Fig. 4.32. Large DRO: target $MA = 135°$, 300 m (behind target)

Fig. 4.33. Large DRO: target $MA = 135°$, 300 m (ahead target)

Fig. 4.34. Large DRO: target $MA = 126°$, 25 km (behind target)

Fig. 4.35. Large DRO: target $MA = 126°$, 25 km (ahead target)

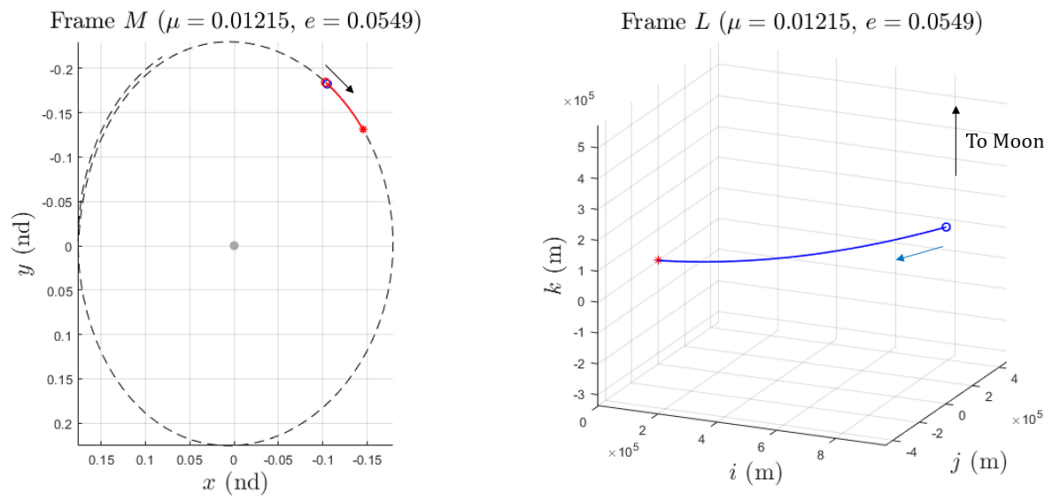Fig. 4.36. Large DRO: target $MA = 117°$, 1000 km (behind target)

Fig. 4.37. Large DRO: target $MA = 117°$, 1000 km (ahead target)

Rendezvous in Large DRO -Results

Table 4.3.
Large DRO Rendezvous Maneuver Results

Reference Orbit	Model	Δv_1 [m/s]	Δv_2 [m/s]	Δv_{tot} [m/s]
Large DRO, Figures 4.26 & 4.32	CR3BP	0.011	0.011	0.021
300 m - Behind, TOF: 8 hrs.	ER3BP	0.011	0.011	0.021
Large DRO, Figures 4.27 & 4.33	CR3BP	0.011	0.011	0.021
300 m - Ahead, TOF: 8 hrs.	ER3BP	0.011	0.011	0.021
Large DRO, Figures 4.28 & 4.34	CR3BP	0.621	0.580	1.201
25 km - Behind, TOF: 12 hrs.	ER3BP	0.614	0.581	1.195
Large DRO, Figures 4.29 & 4.35	CR3BP	0.621	0.580	1.201
25 km - Ahead, TOF: 12 hrs.	ER3BP	0.614	0.581	1.195
Large DRO, Figures 4.30 & 4.36	CR3BP	19.148	17.403	36.551
1000 km - Behind, TOF: 16 hrs.	ER3BP	18.972	17.454	36.426
Large DRO, Figures 4.31 & 4.37	CR3BP	19.146	17.404	36.550
1000 km - Ahead, TOF: 16 hrs.	ER3BP	18.959	17.455	36.415

Finally, rendezvous trajectories long the Large DRO are computed for both the CR3BP and ER3BP reference orbits. The varying geometry between the reference orbits in both dynamical models produce slightly different Δv values, however, the differences between the CR3BP and ER3BP rendezvous results are slight as they increase with a greater initial relative distance between the target and the chaser. Each rendezvous case successfully computes a chaser trajectory that intercepts the target position in the LVLH frame L.

4.2   Spacecraft Loitering

Another application of relative motion examined in this investigation is spacecraft loitering. The aim of loitering is to produce bounded relative motion of the chaser in the LVLH Frame L with respect to the target. One of the ways to accomplish this is by examining natural loitering behaviors where the chaser trajectory is bounded in frame L without the implementation of maneuvers. The principle behind natural loitering stems from the fact that if the target and chaser are placed along the same reference trajectory but at different mean anomalies, their relative motion will also be bounded. Additionally, if a particular trajectory is periodic or near periodic in the synodic frame M, then the relative positions between the spacecraft along that trajectory will repeat in the LVLH frame L with the orbital period. In this investigation, spacecraft loitering is examined in all three reference orbits, namely the 9:2 NRHO, small DRO, and large DRO for the ER3BP. Results for these reference orbits in the CR3BP are nearly identical for the cases involving the ER3BP reference orbits, however the relative motion is repeated. As an example, consider the target and chaser along the same reference trajectory (9:2 NRHO in the CR3BP) but at different initial mean anomalies. Figure 4.38 plots the initial position of the target and chaser along the NRHO denoted with the red and blue circles, respectively. The starred points represent the target and chaser position after one full period of the NRHO, thus they arrive at the initial point at the end of the propagation. Likewise, the right figure plots the corresponding relative motion with the blue circle denoting the initial chaser position. Since the 9:2 NRHO is perfectly periodic, the relative trajectory is repeated with the target orbit period. For other cases examined in the investigation, the chaser and target are placed much closer together and thus their trajectories will differ from the schematic provided in Figure 4.38. Four loitering cases are examined in each reference orbit with varying initial relative distances and configurations of the chaser both behind and ahead of the target at the initial time. Using the same indicators provided in the schematic, Figures 4.39 and 4.40 plot natural loitering trajectories for

a chaser along the 9:2 NRHO in the ER3BP at an initial relative distance of 300 m behind and ahead of the target, respectively. Likewise, Figure 4.41 and 4.42 examine 9:2 NRHO natural loitering trajectories for a greater initial relative distance of 1000 km. Each case is propagated for a full period of the reference orbit where the varying period in the ER3BP is computed as the time between perilunes with each revolution. Figures 4.43 - 4.46 examine natural spacecraft loitering trajectories for the small DRO in the ER3BP at varying relative distances and different chaser configurations with respect to the target. Finally, Figures 4.47- 4.50 plot the natural spacecraft loitering trajectories for the large DRO in the ER3BP with initial relative distances ranging from 300m to 1000 km between the target and chaser.
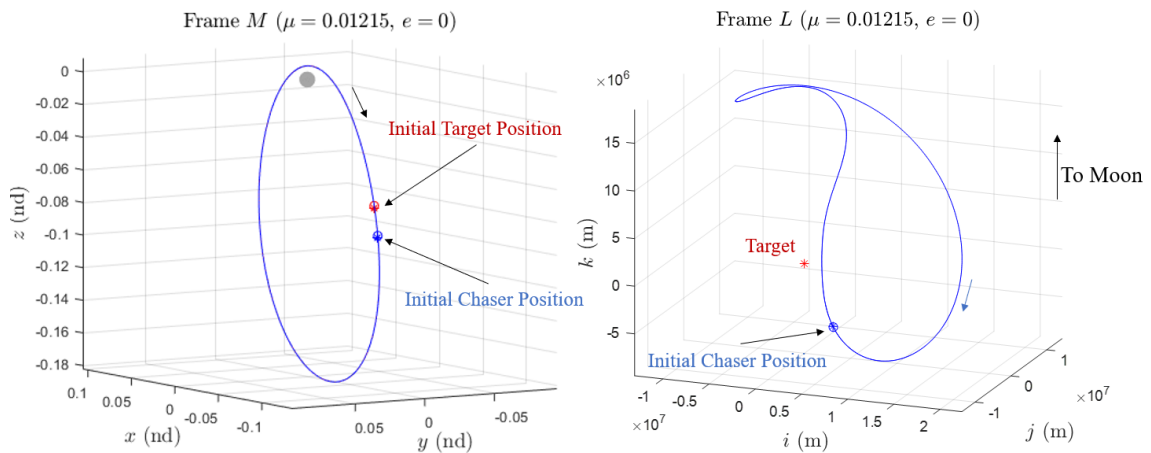
Fig. 4.38. 9:2 NRHO Loitering Description
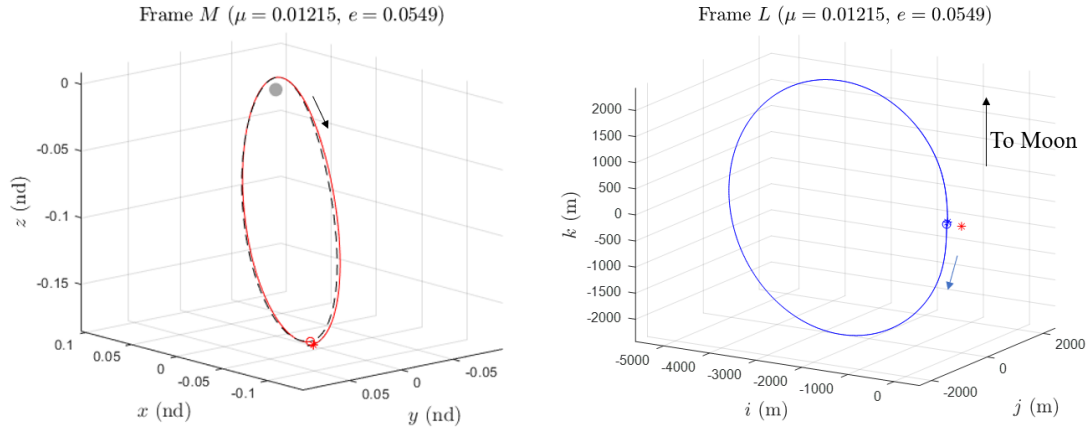
Natural Loitering in 9:2 NRHO - ER3BP

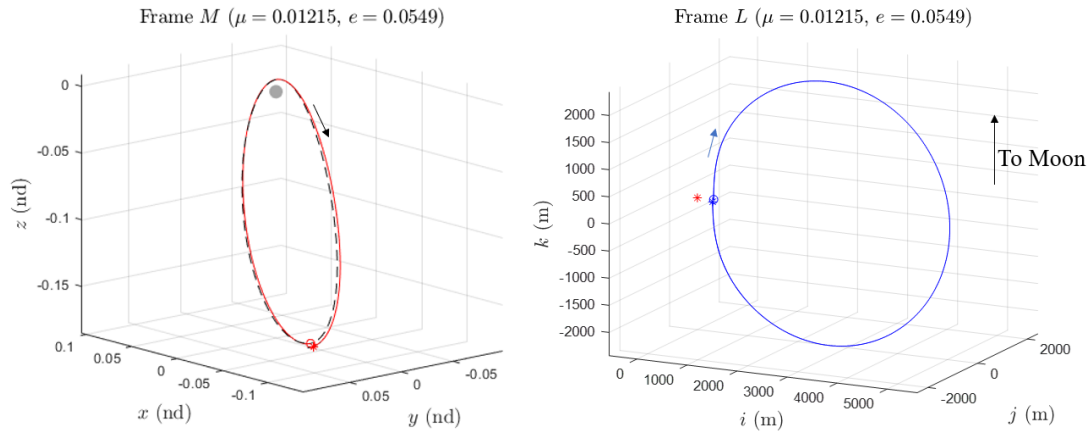Fig. 4.39. 9:2 NRHO: target $MA = 180°$, 300 m (behind target)

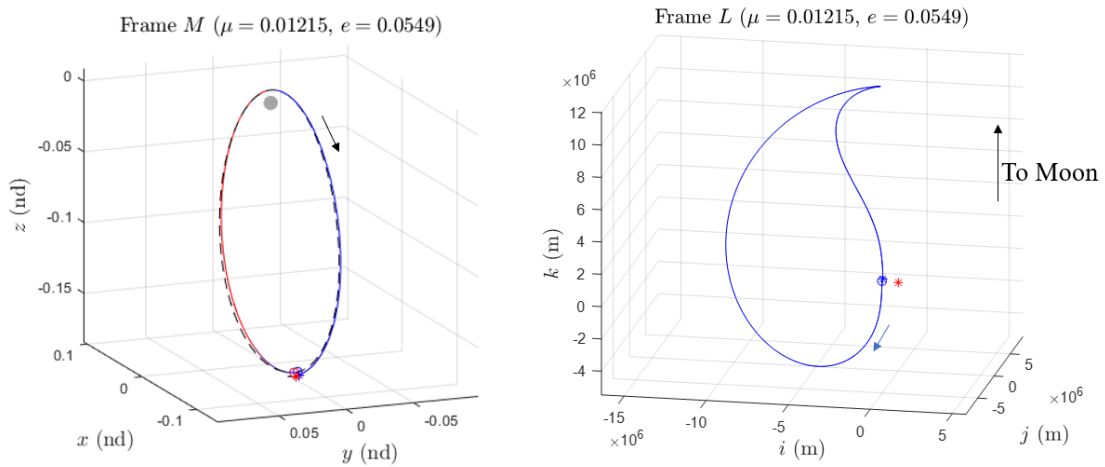Fig. 4.40. 9:2 NRHO: target $MA = 180°$, 300 m (ahead target)

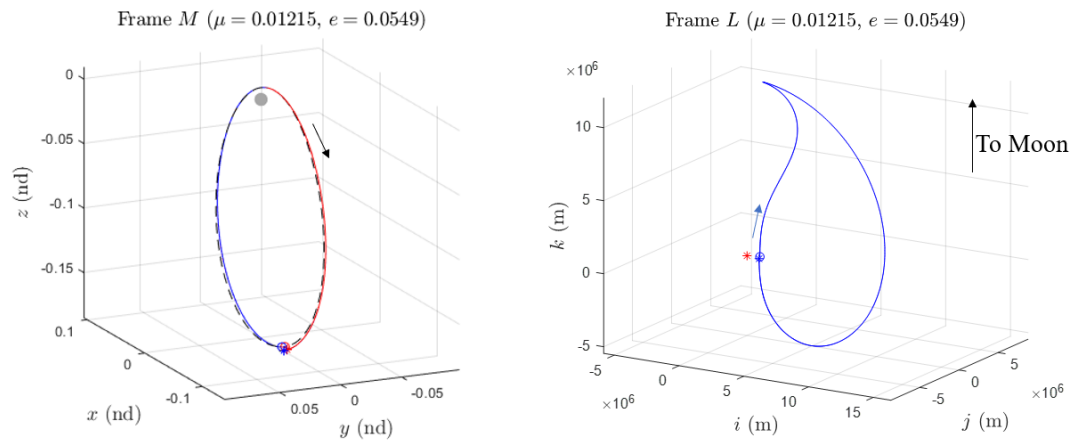Fig. 4.41. 9:2 NRHO: target $MA = 180°$, 1000 km (behind target)

Fig. 4.42. 9:2 NRHO: target $MA = 180°$, 1000 km (ahead target)
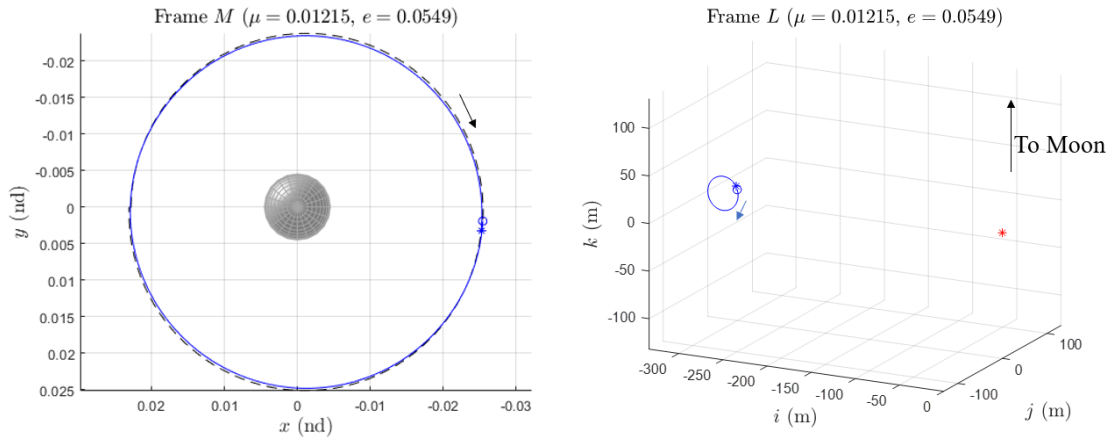
Natural Loitering in the Small DRO - ER3BP

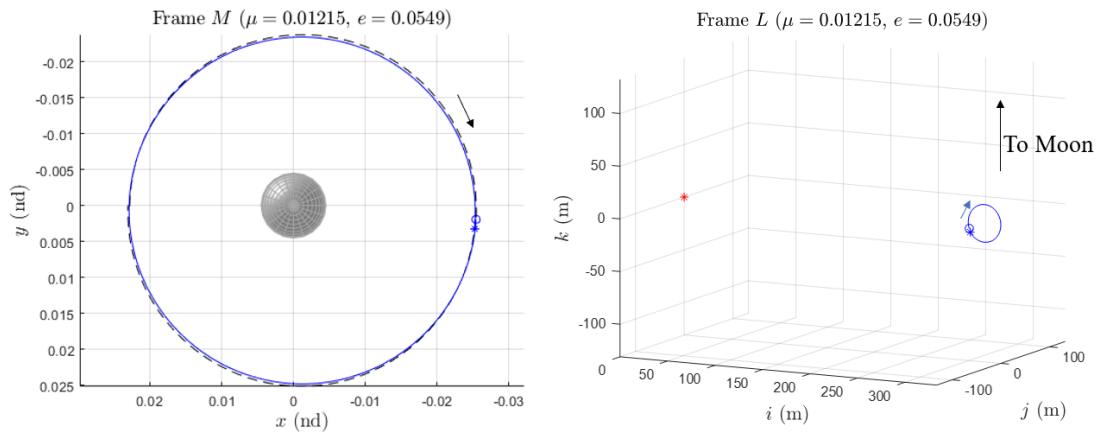Fig. 4.43. Small DRO: target $MA = 180°$, 300 m (behind target)

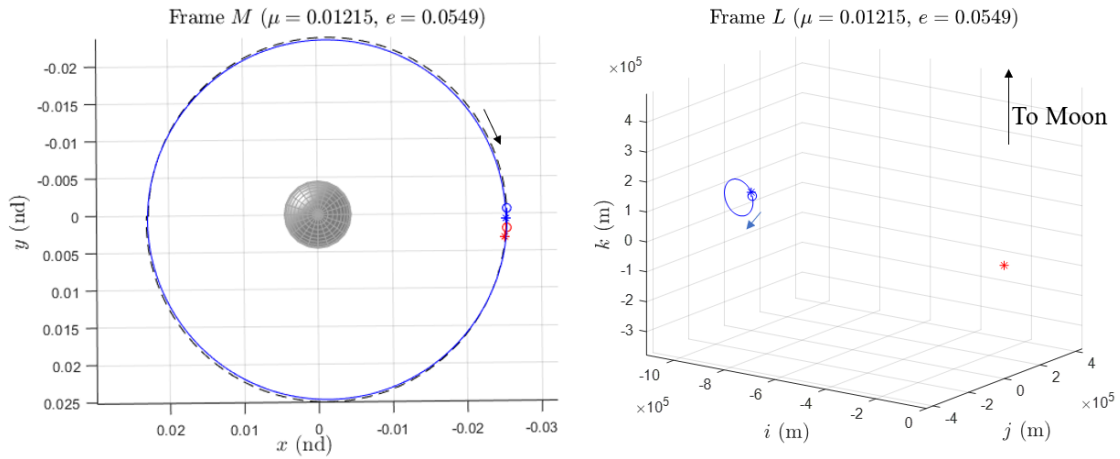Fig. 4.44. Small DRO: target $MA = 180°$, 300 m (ahead target)

Fig. 4.45. Small DRO: target $MA = 180°$, 1000 km (behind target)
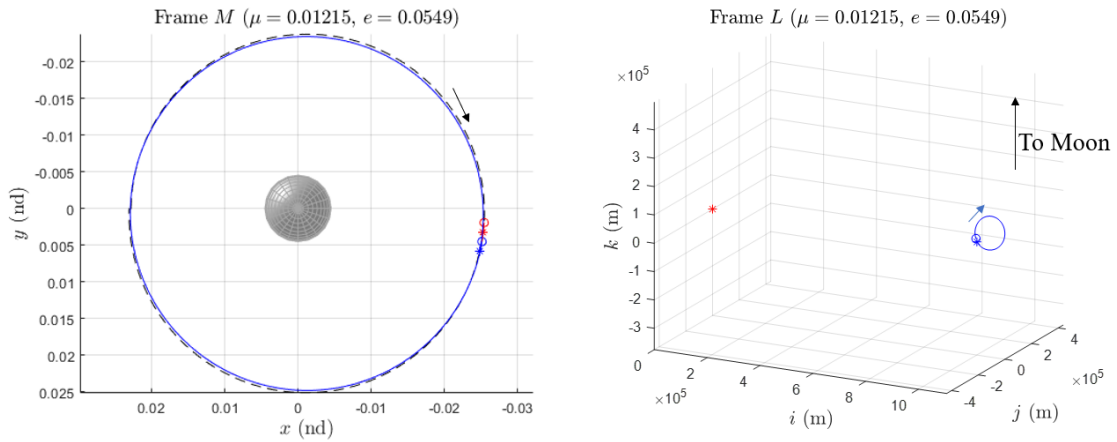

Fig. 4.46. Small DRO: target $MA = 180°$, 1000 km (ahead target)

Natural Loitering in the Large DRO - ER3BP
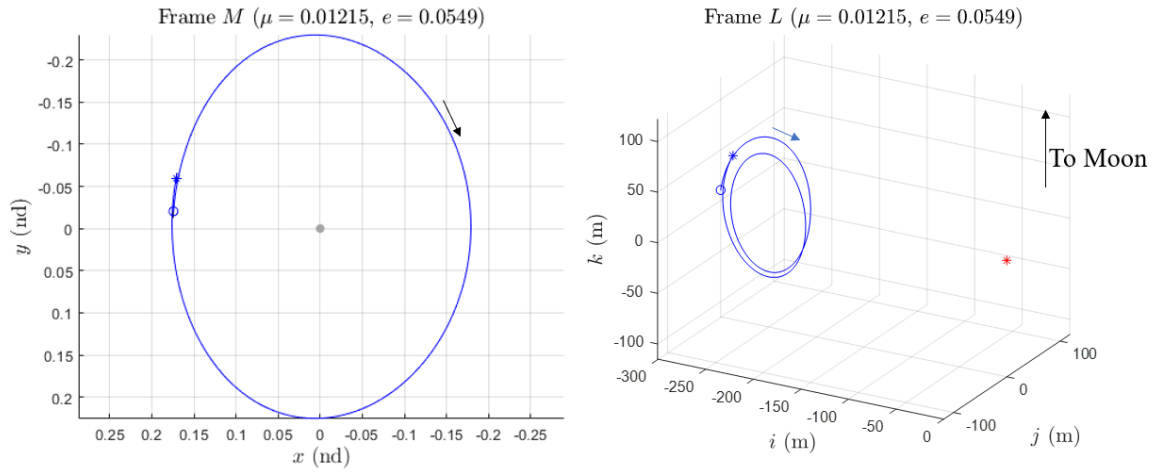

Fig. 4.47. Large DRO: target $MA = 0°$, 300 m (behind target)
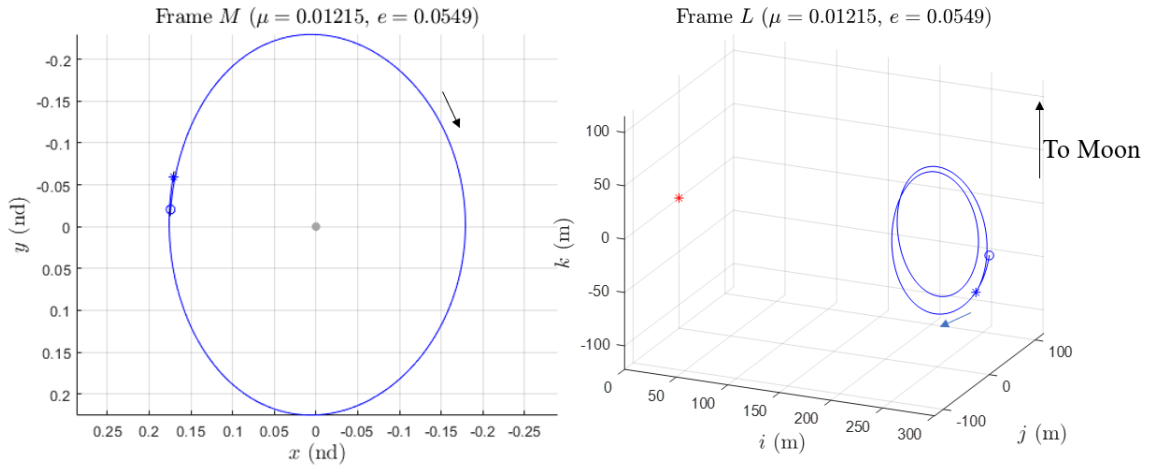

Fig. 4.48. Large DRO: target $MA = 0°$, 300 m (ahead target)
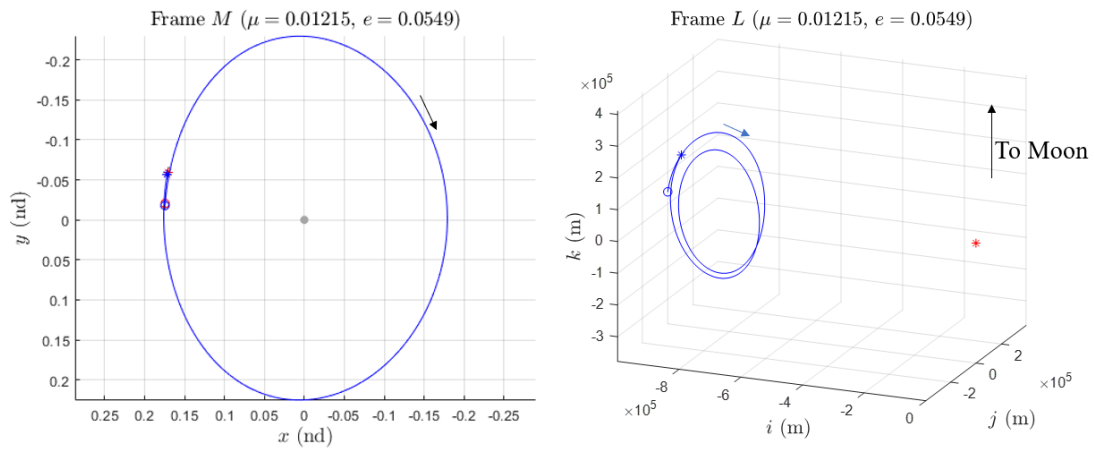
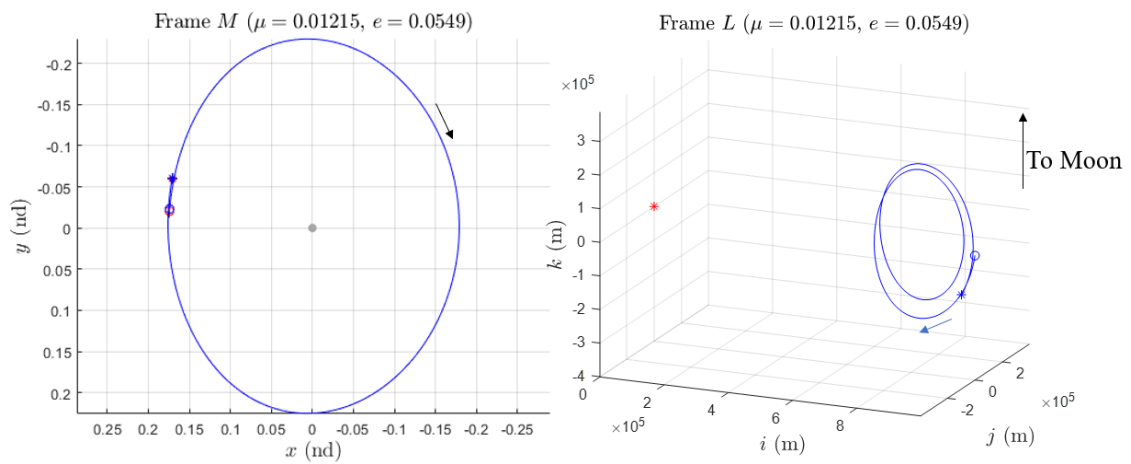Fig. 4.49. Large DRO: target $MA = 0°$, 1000 km (behind target)

Fig. 4.50. Large DRO: target $MA = 0°$, 1000 km (ahead target)

In all the natural spacecraft loitering cases, the relative motion produced in the LVLH frame L is near periodic due to the fact that the reference orbits do not repeat in the synodic frame M. Nevertheless, the relative trajectories are bounded with respect to the target which accomplishes the main objective for the loitering problem. In practice, the chaser may not necessarily loiter for one full period of the reference orbit so segments of the loitering trajectories may be selected depending on the mission application. One of the advantages of natural loitering includes the absence of any maneuvers during the loitering period to maintain a bounded result in the LVLH frame. Nevertheless, the relative trajectories are not controllable along only appear along on one side of the target. For example, for those scenarios involving the chaser behind the target at initial time, the relative motion exists almost entirely in the $-\hat{\mathbf{i}}$ direction. Likewise, the scenarios where the chaser is initially placed ahead of the target, the resulting relative motion is contained along the $+\hat{\mathbf{i}}$ direction. Therefore, spacecraft loitering needs to produce more variable relative geometries for applications requiring more complex chaser movements around the target.

Forced Loitering

Spacecraft loitering involving the execution of multiple maneuvers is another way to produce relative motion in the LVLH frame L. Unlike natural loitering, forced loitering allows for more variation in the relative geometry since the chaser can perform maneuvers in the vicinity of the target. The forced loitering approach is similar to the multiple shooting formulation presented for obtaining solutions in the CR3BP, however the state variables employed are quantities expressed in the local frame. A relative trajectory is discretized into a number of trajectory segments and patchpoints. The patchpoints are selected positions in relative space about the target and can be specified at some relative distance along the LVLH axes. The "relative" multiple shooter is employed to correct for relative position continuity, yet it allows the relative velocity at patchpoints to vary indicating the presence of a maneuver.

Figure 4.51 depicts a schematic outlining the components of a forced loitering approach. The black points along the trajectory denote the relative patchpoints in the LVLH Frame L. Assuming the trajectory is continuous in relative position, the Δvs at each patchpoint denote a velocity discontinuity which is interpreted as a chaser maneuver. In this investigation, forced loitering approaches are examined for the 9:2 NRHO, small DRO, and large DRO in both the CR3BP and the ER3BP. Specifically, certain relative geometries are determined apriori and the converged result provides a continuous relative trajectory continuous in position. Each case provides a plot in Frame M to indicate the starting location of the target and along the corresponding reference orbit. The chaser is placed at an initial relative distance from the target and both spacecraft are propagated for a specified time of flight. Since spacecraft loitering is typically employed when the chaser and target are relatively close to one another, the chaser may not be visible in Frame M due to the axes scaling in the plot. Nevertheless, another plot is presented in Frame L depicting the resulting relative motion over the propagation time interval. In this view, a chaser initial relative state is specified with respect to the target and converged along a trajectory continuous at the predetermined patchpoints. The starred locations along the relative trajectory indicate a maneuver to ensure that the chaser intercepts its next relative patchpoint. As an example, Figure 4.52 plots a forced loitering scenario in the 9:2 NRHO for the CR3BP. Initial positions of the chaser and target are specified along with the locations of each maneuver corresponding to the selected relative patchpoints. In this investigation, certain relative geometries like the "diamond" shape are produced as a proof of concept for the forced loitering approach. In practice, any combination of relative patchpoints can be used, however the "diamond" shape demonstrates the capability of targeting positions both ahead and behind the target. Figures 4.53 and 4.54 plot forced loitering scenarios in the 9:2 NRHO at around 3 km about the target for the CR3BP and ER3BP, respectively. A loitering distance of up to 1000 km along a different relative trajectory is plotted in Figures 4.55 and 4.56. Scenarios are also considered in the small DRO for the CR3BP and ER3BP in Figures 4.57 - 4.60

with varying loitering distances from 300 m to 25 km between the target and chaser. Moreover, forced loitering in the large DRO is examined for both the CR3BP and ER3BP in Figures 4.61 and 4.62, respectively. Finally, a combined forced loiter and rendezvous example is examined in the large DRO in Figures 4.63 and 4.64.
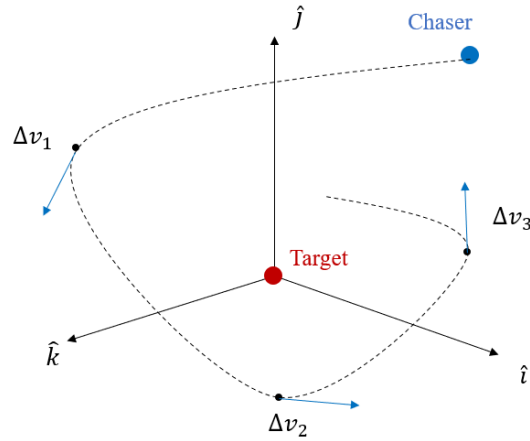

Fig. 4.51. Forced loitering schematic with multiple relative patch-points around the target
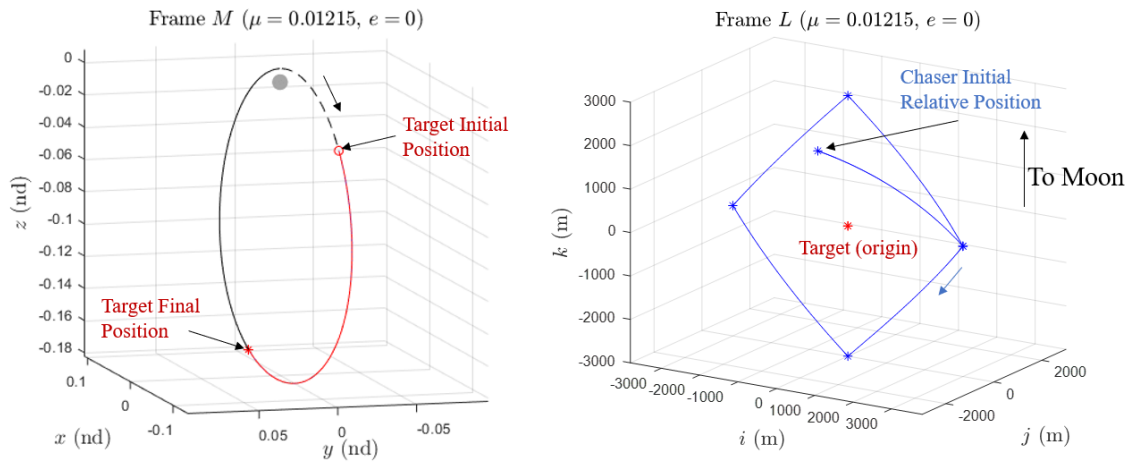

Fig. 4.52. Forced loitering example in the 9:2 NRHO

Forced Loitering in the 9:2 NRHO

Fig. 4.53. 9:2 NRHO Loiter at 300 m in CR3BP

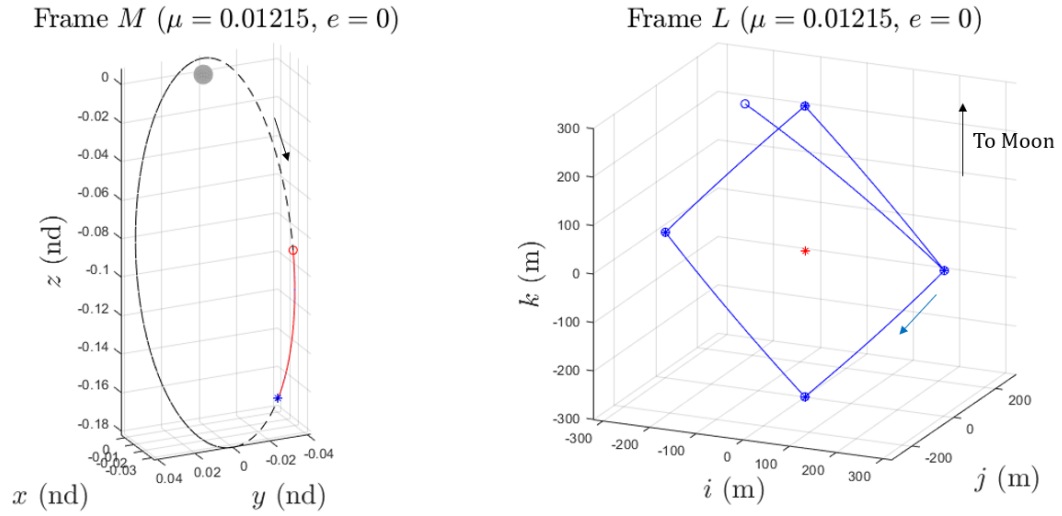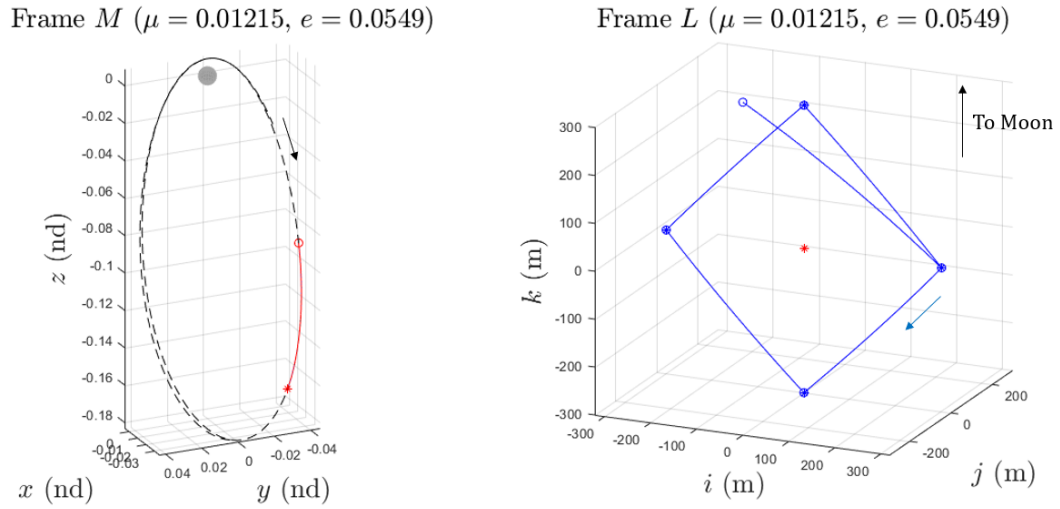Fig. 4.54. 9:2 NRHO Loiter at 300 m in ER3BP
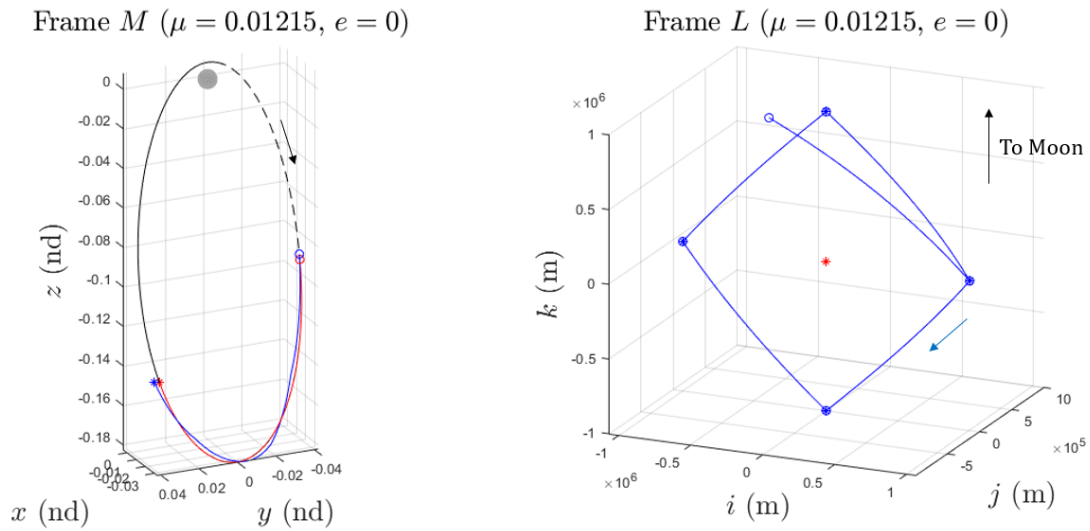
Fig. 4.55. 9:2 NRHO Loiter at 1000 km in CR3BP
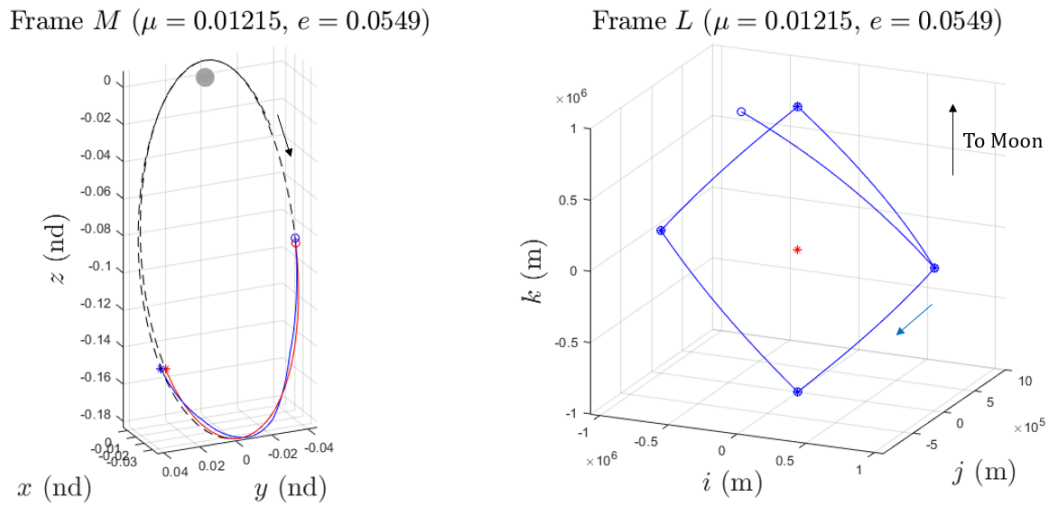
Fig. 4.56. 9:2 NRHO Loiter at 1000 km in ER3BP

Forced Loitering in the Small DRO
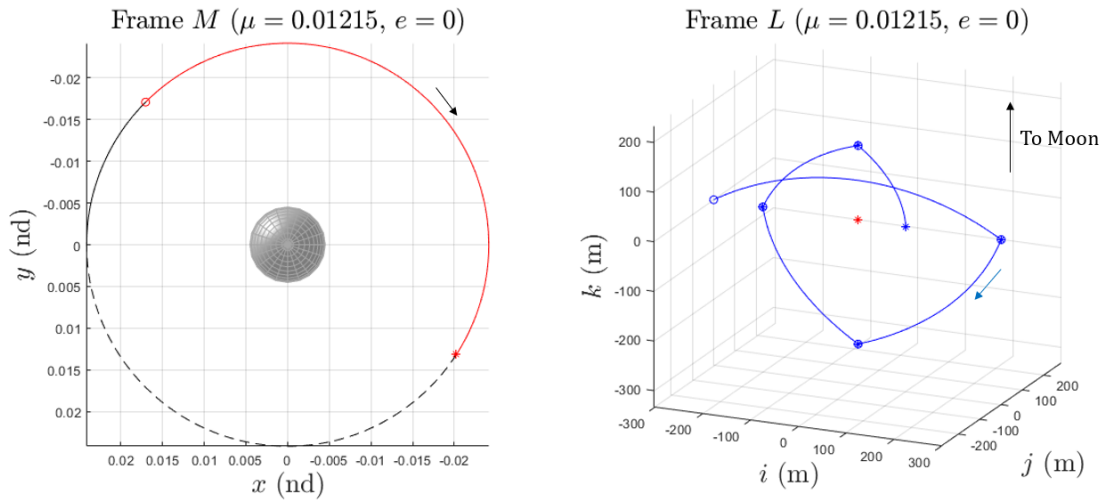
Fig. 4.57. Small DRO Loiter Spiral at 300 m in CR3BP
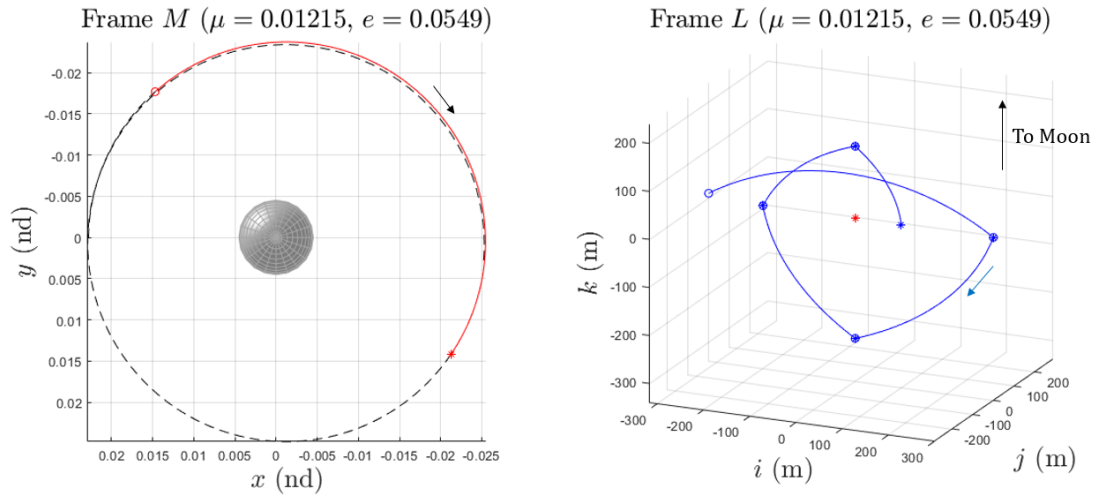
Fig. 4.58. Small DRO Loiter Spiral at 300 m in ER3BP

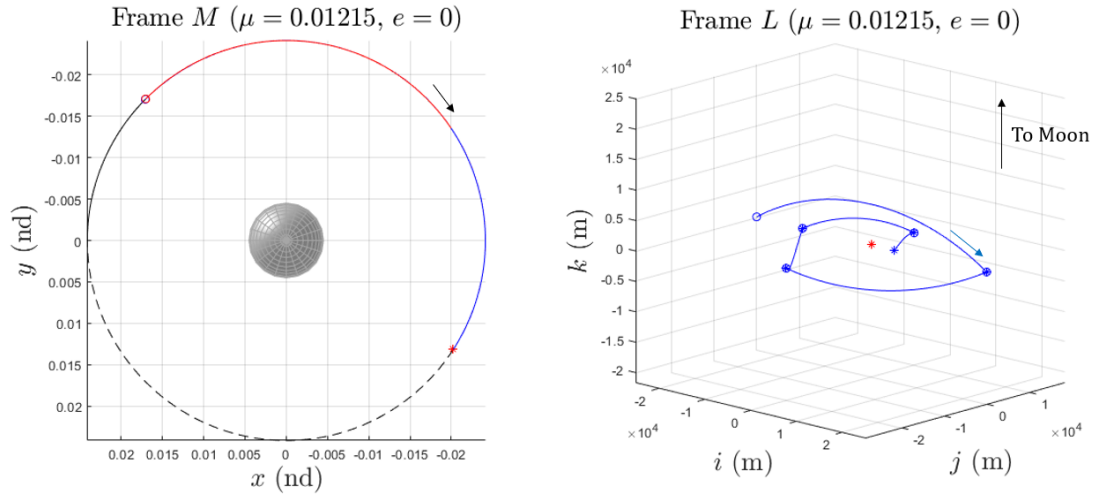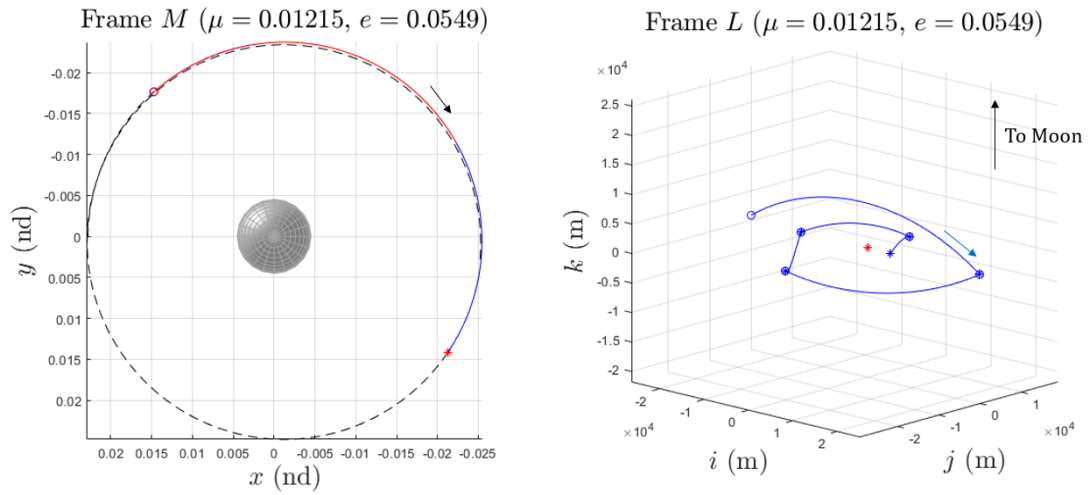Fig. 4.59. Small DRO Loiter Spiral at 25 km in CR3BP

Fig. 4.60. Small DRO Loiter Spiral at 25 km in ER3BP

Forced Loitering in the Large DRO
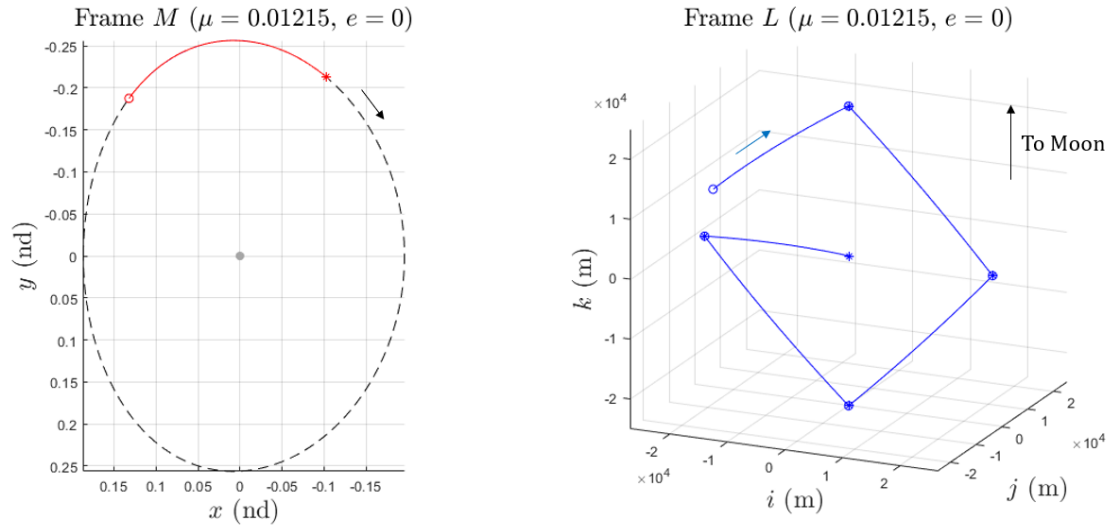
Fig. 4.61. Large DRO Loiter and Rendezvous at 25 km in CR3BP
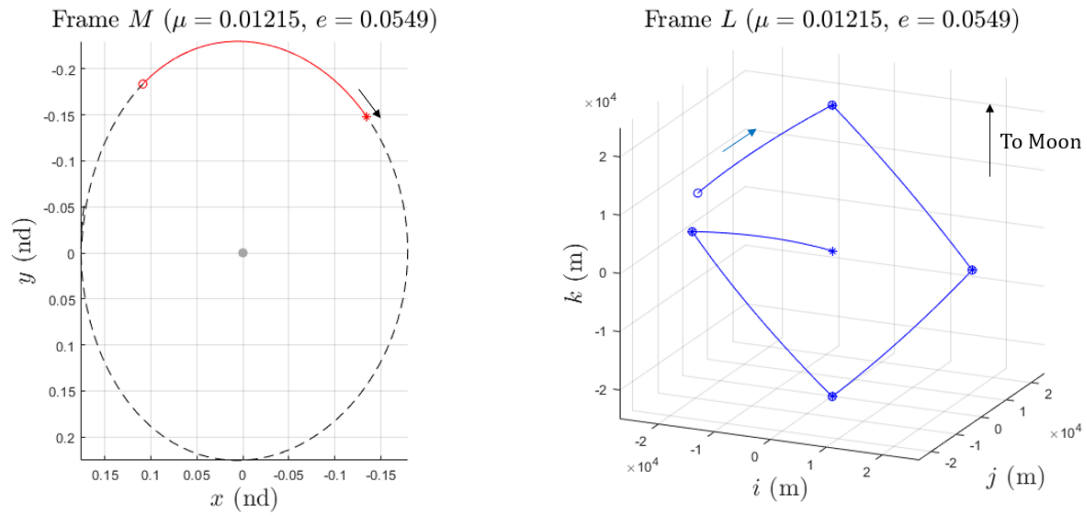
Fig. 4.62. Large DRO Loiter and Rendezvous at 25 km in ER3BP
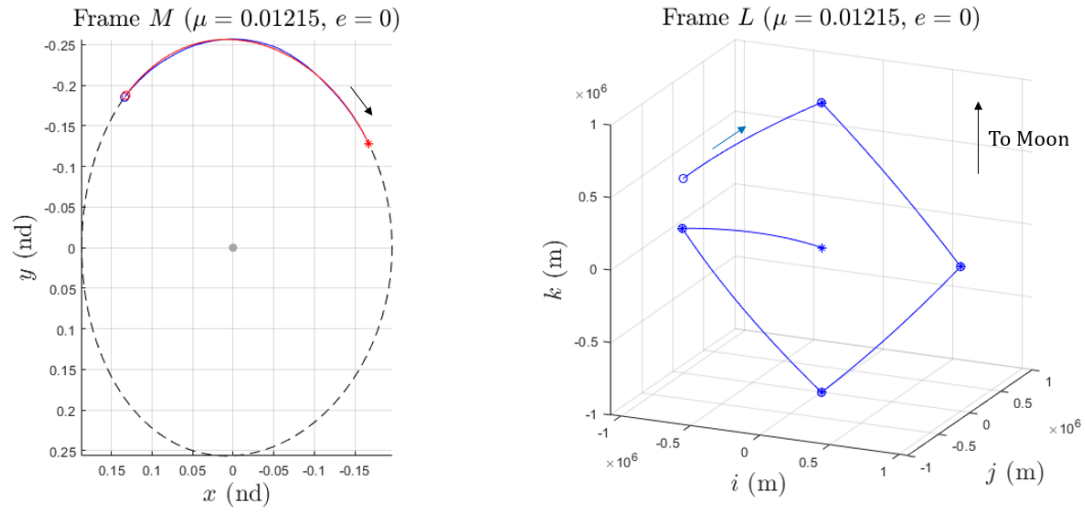
Fig. 4.63. Large DRO Loiter and Rendezvous at 1000 km in CR3BP
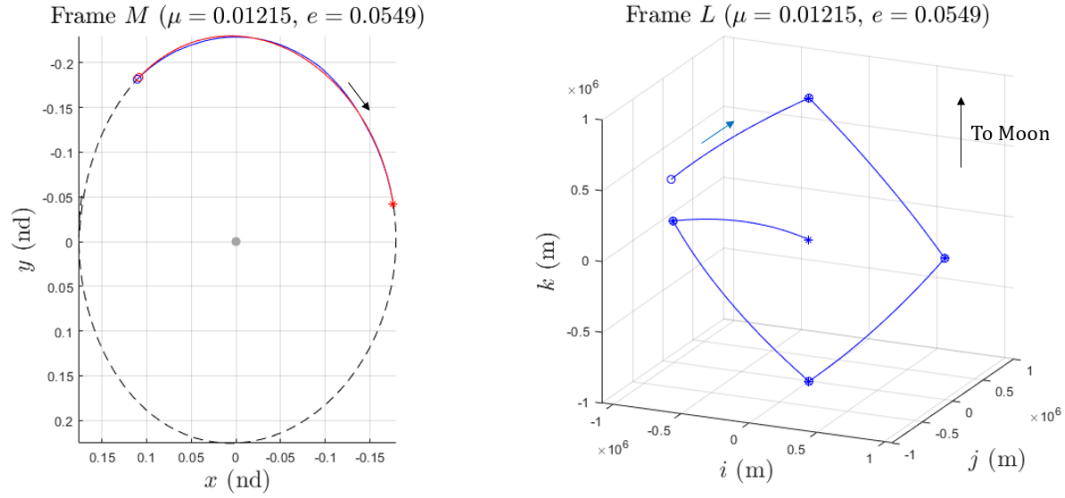
Fig. 4.64. Large DRO Loiter and Rendezvous at 1000 km in ER3BP

Table 4.4.
Forced Loitering Case Descriptions with Δv magnitudes

Reference Orbit	Model	Δv_1 [m/s]	Δv_2 [m/s]	Δv_3 [m/s]	Δv_4 [m/s]	Δv_5 [m/s]	Δv_{tot} [m/s]
9:2 NRHO , 300 m Loiter	CR3BP	0.022	0.032	0.027	0.027	0.027	0.135
Figs 4.53, 4.54 , TOF: 30 hrs.	ER3BP	0.022	0.032	0.027	0.027	0.027	0.135
9:2 NRHO , 1000 km Loiter	CR3BP	20.093	28.715	27.098	24.766	27.136	127.808
Figs 4.55, 4.56 , TOF: 100 hrs.	ER3BP	20.242	28.848	27.019	24.726	27.000	127.836
Small DRO , 300 m Spiral	CR3BP	0.087	0.095	0.048	0.023	0.031	0.284
Figs 4.57, 4.58 , TOF: 10 hrs.	ER3BP	0.089	0.094	0.048	0.025	0.031	0.288
Small DRO , 25 km Spiral	CR3BP	7.223	9.986	5.874	4.027	3.131	30.241
Figs 4.59, 4.60 , TOF: 10 hrs.	ER3BP	7.348	10.031	5.869	4.064	3.123	30.435
Large DRO , 25 km Loiter	CR3BP	0.534	0.718	0.884	0.877	1.012	4.026
Figs 4.61, 4.62 , TOF: 75 hrs.	ER3BP	0.569	0.731	0.863	0.852	0.990	4.004
Large DRO , 1000 km Loiter	CR3BP	16.523	20.694	26.083	25.4156	29.403	118.119
Figs 4.63, 4.64 , TOF: 100 hrs.	ER3BP	17.728	20.951	24.834	24.047	27.933	115.494

The results presented in Table 4.4 provide approximations of the Δvs required to produce the desired relative geometries in each of the reference orbits. There is no significant difference between approximations in the CR3BP and ER3BP and they produce nearly identical loitering geometries. The benefit of forced loitering includes more variation in the loitering trajectory through the implementation of multiple chaser maneuvers about the target. For each of the forced loitering scenarios, a different relative geometry is obtained to represent loitering at a fixed distance, spiral close approaches, and coupled loitering and rendezvous mission profiles. Although it does require a higher cost of propellant use, relative distances between the target and chaser can be maintained for an extended interval of time. In application, forced loitering can be useful to perform before a close approach between the spacecraft so that the chaser may orbit the target for an initial inspection before proceeding to achieve terminal rendezvous. Moreover, a forced loitering approach can be useful to ensure collision avoidance by specifying a loitering geometry at a minimum relative distance between the spacecraft. In either natural or forced loitering, relative geometries are depicted from the perspective of the target which is useful for establishing a baseline intuition regarding the relative behavior of the spacecraft along the different reference orbits examined in this investigation.

5. SUMMARY AND RECOMMENDATIONS

5.1 Summary of the Present Work

NASA's proposed Artemis missions for the mid-2020s outline a series of objectives to establish a permanent crewed platform in the lunar vicinity. The missions are characterized by a long duration in cislunar orbit, the assembly of a lunar orbiting platform called Gateway, and meeting the operating requirements for the Orion spacecraft. Relative motion plays an important role in fulfilling some of the Artemis missions' most immediate requirements by examining the behavior of spacecraft with respect to one another. Rendezvous and spacecraft loitering between Orion and Gateway will be a fundamental step in the integration of mission components to achieve a sustainable human presence around the Moon. In pursuit of this mission objective, this investigation examines the selection of reference orbits of interest for the Artemis program. Different reference solutions including the 9:2 L_2 NRHO, a small DRO, and a large DRO are obtained in different dynamical models describing the Earth-Moon system. The most simplified model employed is the Circular Restricted Three-Body Problem (CR3BP) where a formulation of the equations of motion, the identification of equilibrium points, and tools to compute periodic orbits and their corresponding families are examined. Reference orbits computed in the CR3BP are transitioned into the Elliptical Restricted Three-Body Problem (ER3BP) to incorporate the Moon's nonzero eccentricity about the Earth. Strategies for transitioning solutions and obtaining the CR3BP equivalents in the ER3BP are formulated and applied to generate a set of reference orbits available in the ER3BP. The inclusion of the ER3BP is by no means a required step to transition solutions to a higher-fidelity ephemeris model, yet it provides some indication of how solutions initially computed in the CR3BP evolve under the assumption of a nonzero eccentricity of the second primary.

Another component of this work includes the formulation, derivation, and validation of the equations of relative motion in each of reference orbits. A local-vertical-local-horizontal (LVLH) frame is placed at a target spacecraft along a reference orbit and the motion of a chaser spacecraft is characterized in this rotating frame. Relative motion models employing both two-body and three-body assumptions are investigated and expressions governing the dynamical evolution of the LVLH frame with respect to an inertial frame are obtained. The result establishes the nonlinear equations of relative motion for the restricted three-body problem (3B-NLERM). A number of two-body relative motion models such as the Hill-Clohessy-Wiltshire (2B-HCW) and the linear equations of relative motion (2B-LERM) are compared against the three-body linearized relative equations of motion (3B-LERM) along each of the reference orbits defined in the CR3BP and ER3BP. Moreover, the 3B-LERM are used to develop shooting strategies in the LVLH frame to address a variety of rendezvous and spacecraft loitering problems. A number of rendezvous applications in each of the reference trajectories are examined with varying initial relative distances between the spacecraft and different times of flight. Results obtained in both dynamical regimes, the CR3BP and ER3BP, are compared and discussed to examine the effect of the Moon's eccentricity on solutions. Finally, spacecraft loitering is examined in the LVLH frame to produce bounded relative motion with respect to a target spacecraft along the different reference orbits. The spacecraft loitering problem is examined along two tracks; namely natural loitering and forced loitering. Natural loitering examines the relative behavior produced when a target and chaser fly along the same reference trajectory but are at different initial positions along the orbit. Results are obtained for both dynamical regimes and a variety of ballistic relative geometries are examined. The analysis is continued to incorporate a multiple maneuver scheme to obtain bounded relative behavior using forced loitering. Several configurations involving selected relative patchpoints are considered and different relative geometries are examined along each of the reference orbits at varying loitering distances.

5.2   Recommendations

In this investigation, a number of recommendations are given regarding the analysis of relative motion in the restricted three body problem. These recommendations are examined in the context of the reference orbits planned for NASA's Artemis missions. Based on the results of this work, it can be concluded that:

- The reference orbits of the 9:2 NRHO, small DRO, and large DRO possess slightly different geometries between the ER3BP and CR3BP. This is due to the fact that some of the characteristics of the orbits in the CR3BP (like periodicity and apolune values) are compromised in the transition process to the ER3BP. Nevertheless, the orbit geometry of the reference orbits is preserved and still provide adequate representations of motion obtained in the CR3BP. The inclusion of the ER3BP is by no means a necessary step to transition solutions to a higher-fidelity ephemeris model, yet it does demonstrate the effect of the lunar eccentricity on baseline solutions.

- The equations of relative motion are validated for the restricted three-body problem in a LVLH frame. They outperform more conventional two-body relative motion models in the 9:2 NRHO, small DRO, and large DRO in their depiction of the relative dynamics along these reference orbits. Although the 2B-HCW is certainly more accurate for the small DRO where the orbit's close proximity to the Moon characterize it as more "Keplerian" in shape, it attains unacceptable error in other orbits of interest. On the contrary, the 3B-LERM perform vastly better than their two-body counterparts, yet regions near perilune should be avoided since the rapid separation of the chaser and target exceed the domain of validity for the linearization.

- The 3B-LERM provide a method to obtain numerical tools to target relative states in the LVLH frame. One of these numerical tools termed the relative state transition matrix Φ_R effectively solves a number of rendezvous and spacecraft

loitering problems. By either targeting the target position or positions around the target, shooting schemes in the LVLH frame better characterize the relative motion from the perspective of the target and ensure that relative constraints on position and velocity are met. There are no significant differences between solutions obtained in the CR3BP and ER3BP, yet it is demonstrated that the equations of relative motion can compute solutions in both regimes.

In summary, the equations of relative motion in the restricted three-body problem are a suitable model to characterize relative dynamics between spacecraft along reference orbits available in three-body dynamical regimes. Their accuracy, numerical tools, and effectiveness in obtaining solutions to a number of rendezvous and spacecraft loitering scenarios serve as a good foundation for relative motion analysis for NASA's proposed Artemis missions.

5.3   Future Work

As mission requirements continue to grow in complexity, a number of avenues for future work involving the rendezvous and spacecraft loitering results are proposed. First, a transition of the solutions obtained in the CR3BP and ER3BP into a higher-fidelity ephemeris model should be performed to demonstrate the validity and persistence of the investigated scenarios under the presence of the other gravitational bodies like the Sun. In addition, a number of other reference orbits should be considered to validate and apply the nonlinear equations of relative motion including other halo orbits of interest. Furthermore, an assessment of the numerical sensitivities of the relative state transition matrix Φ_R should be performed for purposes of station-keeping in the LVLH frame. The assessment will aid in the implementation and formulation of relative GNC systems to address future navigation problems for NASA's Artemis missions. Finally, optimizing the results obtained for impulse maneuvers should be examined to provide a better idea of where to execute rendezvous and spacecraft loitering maneuvers. Additional incorporation of constraints specific

to the Orion spacecraft should be considered before any baseline reference trajectory is provided for the real-world missions.

REFERENCES

REFERENCES

[1] G. Franzini and M. Innocenti, "Relative motion equations in the localvertical local-horizon frame for rendezvous in lunar orbits", in Proc. 2017 AAS/AIAA Astrodynamics Specialist Conference, Stevenson,WA, USA, Aug. 2017, Paper AAS 17-641.

[2] W. H. Clohessy and R. S. Wiltshire, "Terminal guidance system for satellite rendezvous," Journal of the Aerospace Sciences, vol. 27, no. 9, pp. 653–658, 1960.

[3] K. Yamanaka and F. Ankersen, "New state transition matrix for relative motion on an arbitrary elliptical orbit," Journal of Guidance, Control, and Dynamics, vol. 25, no. 1, pp. 60–66, 2002.

[4] Franzini, Giovanni. PhD Thesis, Universita di Pisa, May 2018. Relative Motion Dynamics and Control in the Two-Body and in the Restricted Three-Body Problem.

[5] Colagrossi, Andrea, and Michèle Lavagna. "Dynamical Analysis of Rendezvous and Docking with Very Large Space Infrastructures in Non-Keplerian Orbits." CEAS Space Journal 10, no. 1 (March 2018): 87–99. https://doi.org/10.1007/s12567-017-0174-4.

[6] Murakami, Naomi, Satoshi Ueda, Toshinori Ikenaga, Maki Maeda, Toru Yamamoto, and Hitoshi Ikeda. "PRACTICAL RENDEZVOUS SCENARIO FOR TRANSPORTATION MISSIONS TO CIS-LUNAR STATION IN EARTH–MOON L2 HALO ORBIT," n.d., 25.

[7] W. S. Koon, M. W. Lo, J. E. Marsden, and S. D. Ross, Dynamical Systems, the Three-Body Problem and Space Mission Design. Marsden Books, 2011.

[8] E. M. Zimovan, K. C. Howell, and D. C. Davis, "Near rectilinear halo orbits and their application in cis-lunar space," in Proc. 3rd IAA Conference on Dynamics and Control of Space Systems, Moscow, Russia, May 2017, Paper IAA-AAS-DyCoSS3-125.

[9] D. Guzzetti, E. M. Zimovan, K. C. Howell, and D. C. Davis, "Stationkeeping analysis for spacecraft in lunar near rectilinear halo orbits," in Advances in the Astronautical Sciences, vol. 160, 2017, pp. 3199–3218, Paper AAS 17-395.

[10] A. Colagrossi, M. Lavagna, and S. F. R. Carna, "Dynamical analysis of rendezvous and docking with very large space infrastructures in non-Keplerian orbits," in Proc. 6th International Conference on Astrodynamics Tools and Techniques, Darmstadt, Germany, Mar. 2016.

[11] K. T. Alfriend, S. R. Vadali, P. Gurfil, J. P. How, and L. S. Breger, Spacecraft Formation Flying. Elsevier, 2010.

[12] J. Sullivan, S. Grimberg, and S. D'Amico, "Comprehensive survey and assessment of spacecraft relative motion dynamics models," Journal of Guidance, Control, and Dynamics, vol. 40, no. 8, pp. 1837–1859, 2017.

[13] W. Fehse, Automated Rendezvous and Docking of Spacecraft. New York: Cambridge University Press, 2003.

[14] Zimovan, Emily M. MSAAE, Purdue University, August 2017. Characteristics and Design Strategies for Near Rectilinear Halo Orbits Within the Earth-Moon System.

[15] McCarthy, Brian P. MSAAE, Purdue University, December 2018. Characterization of Quasi-Periodic Orbits for Applications in the Sun-Earth and Earth-Moon Systems.

[16] William H. Gerstenmaier. Progress in Defining the Deep Space Gateway and Transport Plan. https://www.nasa.gov/sites/default/files/atoms/files/nss_chart_v23.pdf, March 28, 2017.

[17] Isaac Newton. The Principia: Mathematical Principles of Natural Philosophy. University of California Press, 1999. Translated by I. Bernard Cohen and Anne Whitman.

[18] Victor Szebehely. Theory of Orbits: The Restricted Problem of Three Bodies. Academic Press, Inc., New York, 1967.

[19] Thomas A. Pavlak. Trajectory Design and Orbit Maintenance Strategies in Multi- Body Dynamical Regimes. Ph.D. Dissertation, School of Aeronautics and Astronautics, Purdue University, West Lafayette, Indiana, May 2013.

[20] Daniel J. Grebow. Generating Periodic Orbits in the Circular Restricted Three-Body Problem with Applications to Lunar South Pole Coverage. M.S. Thesis, School of Aeronautics and Astronautics, Purdue University, West Lafayette, Indiana, May 2006.

[21] Wayne R. Schlei. Interactive Spacecraft Trajectory Design Strategies Featuring Poincare Map Topology. Ph.D. Dissertation, School of Aeronautics and Astronautics, Purdue University, West Lafayette, Indiana, May 2017.

[22] Davide Guzzetti. GRANT: NNX13AK60 Final Report. Technical Report, Purdue University, NASA, 2016.

[23] D. J. Grebow, M. T. Ozimek, K. C. Howell, and D. C. Folta. Multi-Body Orbit Architectures for Lunar South Pole Coverage. In Paper No. AAS 06-179, AAS/AIAA Spaceflight Mechanics Meeting, Tampa, Florida, January 2006.

[24] M. Henon. Numerical Exploration of the Restricted Problem. VI: Hill's case: Non-Periodic Orbits. Astronomy and Astrophysics, 9:24-36, 1970.

[25] A. E. Roy and M. W. Ovenden. On the occurence of commensurable mean motions in the solar system. the mirror theorem. Monthly Notices of the Royal Astronomical Society, 115:296, December 1954.

[26] Zimovan-Spreen, E. M. , Howell, K. C., and Davis, D. C., "Near Rectilinear Halo Orbits and Nearby Higher-Period Dynamical Structures: Orbital Stability and Resonance Properties," Celestial Mechanics and Dynamical Astronomy, Vol. 132, No. 28, June 2020

[27] N. Bosanac, "Leveraging Natural Dynamical Structures to Explore Multi-Body Systems," Ph.D., August 2016.

[28] National Space Council. "Presidential Memorandum on Reinvigorating America's Human Space Exploration Program". December 2017.

[29] Boudad, K. K; Davis, D. C. & Howell, K. C. Dynamics of Synodic Resonant Near Rectilinear Halo Orbits in the Bicircular Four-Body Problem. Manuscript submitted for publication, 2020

[30] Whitley, Ryan J, Diane C Davis, Laura M Burke, Brian P McCarthy, J Power, Melissa L McGuire, and Kathleen C Howell. "Earth-Moon Near Rectilinear Halo and Butterfly Orbits for Lunar Surface Exploration,". AAS/AIAA Astrodynamics Specialist Conference, Snowbird, UT. 2018.

[31] J. A. Kechichian, "Motion in general elliptic orbit with respect to a dragging and presessing coordinate frame," The Journal of the Astronautical Sciences, vol. 46, no. 1, pp. 25–45, 1998.

[32] G. Xu, J. Luo, Z. Li, and X. Chen, "Equations of satellite relative motion in low Earth orbit under lunar perturbation," in Proc. 2014 IEEE Chinese Guidance, Navigation and Control Conference, Yantai, China, Aug. 2014, pp. 113–120.

[33] S. Casotto, "The equations of relative motion in the orbital reference frame," Celestial Mechanics and Dynamical Astronomy, vol. 124, no. 3, pp. 215–234, 2016.

[34] H. Schaub and J. L. Junkins, Analytical Mechanics of Space Systems, 2nd ed. Reston, VA: American Institute of Aeronautics and Astronautics, 2009.